Plasmonics and Electron Optics in Graphene

Thesis by

Min Seok Jang

In Partial Fulfillment of the Requirements

for the Degree of

Doctor of Philosophy

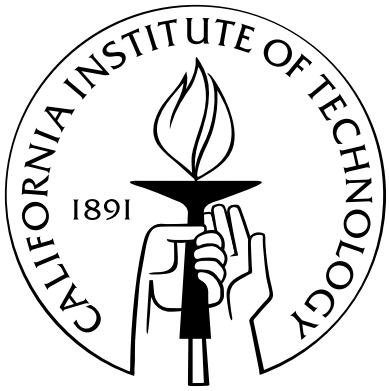

California Institute of Technology

Pasadena, California

2013

(Defended Nov 21, 2012)

Acknowledgements

First, I would like to thank my advisor, Professor Harry Atwater. He always amazes me with his endless energy, enthusiasm, and knowledge. With his guidance, I have been able to experience diverse aspects of research throughout my graduate program. I especially thank him for giving me an opportunity to learn experiments at the end of my graduate studies.

Victor Brar has been a wonderful teacher for an experiment novice. He, Seyoon Kim, Josue Lopez and I have been working as a team on the graphene plasmonics project. I also thank Stanley Burgos for helping me to get accustomed to the Atwater group. He has been not only a good friend, but also a great mentor. It was my fortune to have worked alongside the inspiring young scientists in Atwater group.

Hyungjun Kim and I have been working on graphene electron optics more than three years. I still remember the days we discussed and wrote simulation codes in the Maui Wowi cafe. From my first year at Caltech, he has been my best friend and an amazing collaborator. I would also like to thank Professor William Goddard and Professor Young Woo Son for helpful discussions and comments.

I also thank my Korean friends who have kept my life enjoyable outside the lab—Chan Youn Park, Chang Soon Park, Jaewon Song, Hee Joong Chung, Junho Suh, Jeongwan Haah, Seokmin Jeon, Seung Ah Lee, Kun Woo Kim, Isaac Kim, Jeesoon Choi, Kiyoul Yang, Jeen Joo Kang, Hyoung Jun Ahn, Sonjong Hwang, and others.

I am grateful to Samsung Scholarship for financial assistance during my graduate study. I also thank Professor Frank Porter for offering numerous opportunities to serve as a teaching assistant for physics courses.

Lastly, but most importantly, I would like to express my deepest gratitude to my

Mom and Dad for their endless supports. My little but bigger brother, Mooseok, you made my days at Caltech truly joyful. Thank you!

Min Seok Jang

November 2012

Pasadena, CA

Abstract

The field of plasmonics has been attracting wide interest because it has provided routes to guide and localize light at nanoscales by utilizing metals as its major building block. Meanwhile, graphene, a two-dimensional lattice of carbon atoms, has been regarded as an ideal material for electronic applications owing to its remarkably high carrier mobility and superior thermal properties. Both research fields have been growing rapidly, but quite independently. However, a closer look reveals that there are actually numerous similarities between them, and it is possible to extract useful applications from these analogies. Even more interestingly, these research fields are recently overlapping to create a new field of research, namely graphene plasmonics.

In this thesis, we present a few examples of these intertwined topics. First, we investigate "rainbow trapping" structures, broadband plasmonic slow light systems composed of single or double negative materials. We clarify the mode-conversion mechanism and the light-trapping performance by analyzing the dispersion relation. We then show that electrons in graphene exhibit photonlike dynamics including Goos-Hänchen effect and the rainbow trapping effect, but quantitatively differently. To study the dynamics of graphene electrons numerically, we develop a finite-difference time domain simulator. We also present a way to enhance electron backscattering in graphene by engineering the dispersion of electron eigenmodes in a Kronig-Penney potential. Finally, we discuss physics of graphene plasmon cavities. We report the resonant mid-infrared transmission across a plasmonic waveguide gap that is governed by the Fano interference between transmission through plasmon modes in graphene and nonresonant background transmission. An ultracompact graphene plasmon cavity, which resonates at near-infrared telecommunication frequencies, is also proposed.

Contents

List of Figures

Chapter 1

Introduction

The field of plasmonics and graphene electronics have been growing rapidly, but quite independently. However, a closer look reveals that there are actually numerous similarities between them, and it is one of the main purpose of this thesis to shed light on and extract useful applications from these analogies. Even more interestingly, these research fields are recently overlapping to create a new field of research, namely graphene plasmonics, which is the last topic of this thesis. In this chapter, we introduce basic concepts of plasmonics, and electronic and optical properties of graphene as bases for detailed discussions in the following chapters.

1.1 Plasmonics

In the past decade, the field of plasmonics has been attracting wide interest because it has provided routes to guide [52, 64, 83] and localize [23, 80, 98] light at scales substantially smaller than the free space wavelength. Unlike the conventional optics, plasmonics actively utilizes metals as its major building block. The interaction between electromagnetic radiation and conduction electrons in metal induces distinctive, often counter intuitive, phenomenon such as negative refraction [12, 55, 88].

In this section, we provide a brief review on the fundamental ingredients of plasmonics, including surface plasmon polaritons (SPP) at metal-dielectric interfaces and eigenmodes in plasmonic slab waveguides. Assuming the Drude model for metals, we derive the field profile and the dispersion relations, and discuss how they differ from

conventional optics.[1]

1.1.1 Drude Model of Metal

In the Drude model, conduction electrons in a metal form a free electron gas and move against fixed background ion cores [25]. When there is an oscillating external electric field $\mathbf{E} = \mathbf{E}_0 e^{-i\omega t}$, the classical equation of motion for an electron becomes

$$\frac{d\mathbf{p}}{dt} = -\frac{\mathbf{p}}{\tau} - e\mathbf{E}, \tag{1.1}$$

where $\mathbf{p}$ is the momentum of the electron. The relaxation time, τ, phenomenologically takes into account the electron scattering inside the metal. The Fourier transform of Eq. (1.1) yields

$$-i\omega\mathbf{p}(\omega) = -\frac{\mathbf{p}(\omega)}{\tau} - e\mathbf{E}(\omega), \tag{1.2}$$

$$\mathbf{p}(\omega) = -\frac{ie\mathbf{E}(\omega)}{\omega + i/\tau} = -\frac{ie\mathbf{E}(\omega)}{\omega + i\Gamma}. \tag{1.3}$$

In the last step, the scattering rate $\Gamma = 1/\tau$ is introduced. The optical conductivity $\sigma(\omega)$, which is the ratio of the current density $\mathbf{j} = -ne\mathbf{p}/m$ to the electric field $\mathbf{E}$, is given by

$$\sigma(\omega) = \frac{\mathbf{j}(\omega)}{\mathbf{E}(\omega)} = -\frac{ne\mathbf{p}(\omega)}{m\mathbf{E}(\omega)} = \frac{ine^2}{m(\omega + i\Gamma)}, \tag{1.4}$$

where n, e, and m are the carrier density, the elementary charge, and the mass of the electron respectively. The relative permittivity of the metal $\epsilon(\omega)$ is directly deduced from Eq. (1.4),

$$\epsilon(\omega) = 1 + i\frac{\sigma(\omega)}{\epsilon_0\omega} = 1 - \frac{ne^2}{m\epsilon_0(\omega^2 + i\Gamma\omega)} = 1 - \frac{\omega_p^2}{\omega^2 + i\Gamma\omega}, \tag{1.5}$$

[1]For more details on electronic and optical properties of metals, see Ref. [2]. Reference [65] provides a general overview of the field of plasmonics. Guided modes in plasmonic slab waveguides are thoroughly investigated in Refs. [23, 24].

where $\omega_p = ne^2/m\epsilon_0$ is the plasma frequency of the free electron gas. Note that, ϵ flips its sign at $\omega = \omega_p$ for small damping $\Gamma \ll \omega$.

It should be noted that the Drude description is valid even up to the ultraviolet for alkali metals, but for noble metals the model becomes inaccurate for high frequencies at which interband transitions occur. A more detailed review on the Drude model and the optical response of metals is given in Ref. [2].

1.1.2 Surface Plasmon Polaritons at a Metal-Dielectric Interface

A flat metal-dielectric interface supports SPPs at frequencies below the plasma frequency ω_p (i.e., the metal has negative permittivity, $\mathrm{Re}\{\epsilon_m\} < 0$). The field profile and the dispersion relation of SPP can be obtained by solving the Maxwell's equations [65]. Let us assign a coordinate system such that the x axis is perpendicular to the metal-dielectric interface ($x = 0$). We seek for transverse magnetic (TM) polarized guided mode propagating along the $+z$ direction with a propagation constant β (the system does not support transverse electric (TE) polarized mode). We adopt the following ansatz for the magnetic field $H_y(x, z)$,

$$H_y(x,z) = \begin{cases} A_2 e^{i\beta z} e^{\gamma_2 x} & \text{where } x < 0, \\ A_1 e^{i\beta z} e^{-\gamma_1 x} & \text{where } x > 0, \end{cases} \tag{1.6}$$

where $\gamma_i = \sqrt{\beta^2 - k_0^2 \epsilon_i}$ and $k_0 = \omega/c$ is the free space wavevector. The expression for the electric field can be obtained from the sorce-less Maxwell's equation $\mathbf{E} = (i/\omega\epsilon_0\epsilon)\nabla \times \mathbf{H}$ [84]. From the continuity of the magnetic field H_y and the in-plane component of electric field E_z, we get

$$A_1 = A_2, \quad \text{and} \tag{1.7}$$

$$\beta = \frac{\omega}{c}\sqrt{\frac{\epsilon_d \epsilon_m}{\epsilon_d + \epsilon_m}}. \tag{1.8}$$

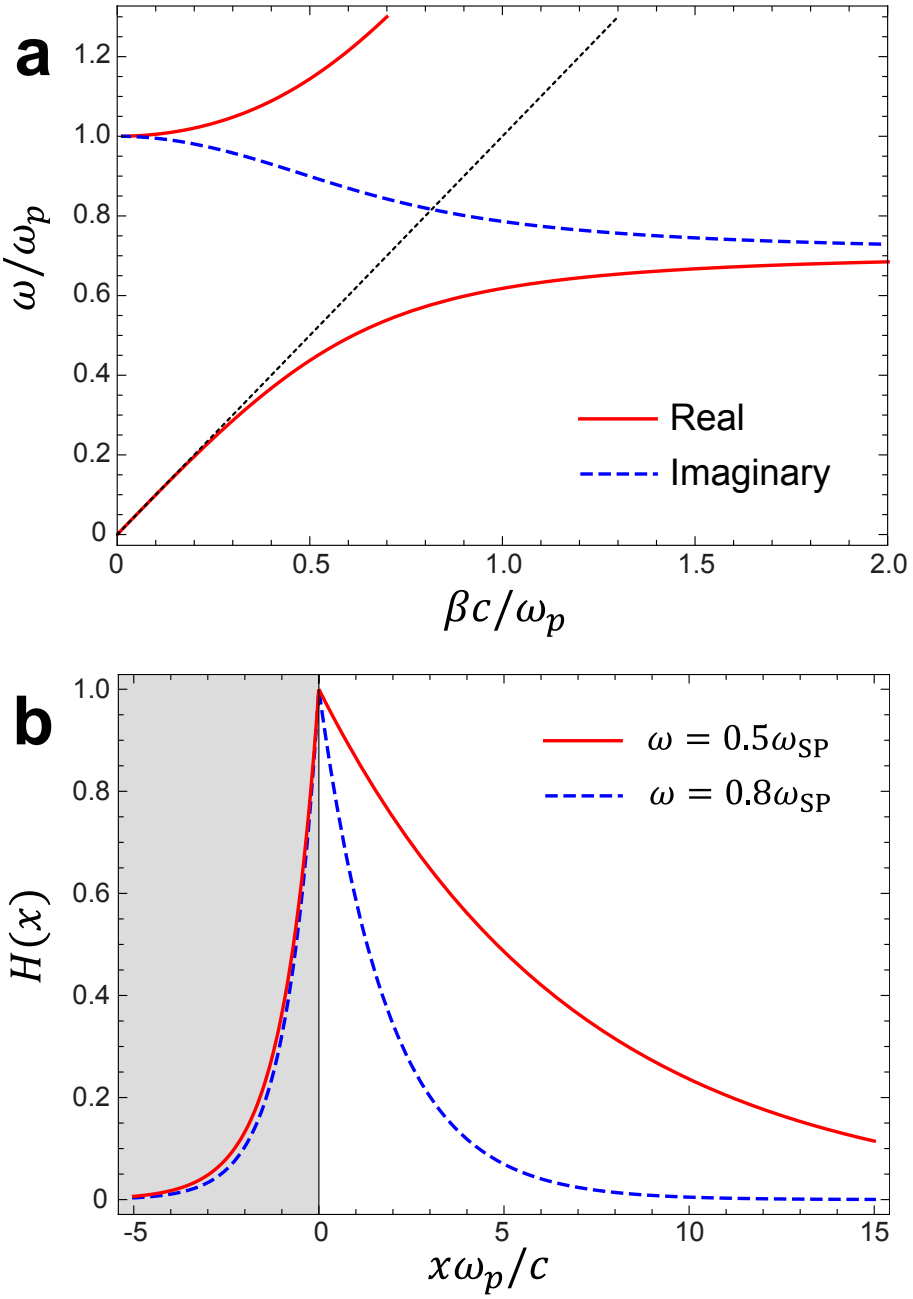

Figure 1.1: (a) Dispersion relation of SPPs at a metal-air interface. The scattering rate Γ is assumed to be negligible. The real part (red solid) and the imaginary part (blue dashed) of the normalized propagation constant $\beta c/\omega_p$ are both presented. The black dotted line indicates the free space dispersion. As ω approaches to $\omega_{\mathrm{SP}} = \omega_p/\sqrt{2}$, the group velocity $v_g = \partial\omega/\partial\beta$ of the SPP decreases. (b) Magnetic field profile of SPPs at $\omega = 0.5\omega_{\mathrm{SP}} = 0.35\omega_p$ (red solid) and $0.8\omega_{\mathrm{SP}} = 0.57\omega_p$ (blue dashed). As $\omega \to \omega_{\mathrm{SP}}$, the SPP becomes more tightly confined near the interface.

Figure 1.1 (a) presents the dispersion relation of SPPs at an interface between the free space ($\epsilon_d = 1$) and a Drude a metal with negligible damping ($\Gamma = 1$). For $\omega > \omega_p$, the metal layer is transparent (i.e., $\epsilon_m > 0$) and thus allows the propagation of unbound radiation. Note that the transverse decay constant γ becomes imaginary in this frequency regime. On the other hand, for $\omega < \omega_{\rm SP} = \omega_p/\sqrt{1+\epsilon_d} = \omega_p/\sqrt{2}$, the interface supports a bound mode. The electromagnetic field in free space becomes more tightly confined near the interface as ω approaches to $\omega_{\rm SP}$ (Fig. 1.1 (b)). The group velocity $v_g = \partial\omega/\partial\beta$ vanishes and the surface plasmon resonance occurs at $\omega = \omega_{\rm SP}$. The condition for the surface plasmon resonance is more generally written as

$$\epsilon_d + \epsilon_m = 0, \tag{1.9}$$

which makes the denominator of Eq. (1.8) vanish. Between $\omega_{\rm SP}$ and ω_p, β is purely imaginary, indicating there is no propagating mode.

1.1.3 Plasmonic Slab Waveguides

By putting two metal-insulator interfaces close together, we form symmetric and antisymmetric hybrid SPP modes. These modes are also referred to as $\rm TM_0$ and $\rm TM_1$ modes respectively, according to the number of zeros in their transverse field profile. For simplicity and clarity, we focus our discussion on two representative trilayer geometries: a metal/insulator/metal (MIM) and an insulator/metal/insulator (IMI) slab waveguides. We further assume that the structures possess a mirror symmetry with respect to $x = 0$ plane. Let the thickness of the core layer be d.

The magnetic field profile for the symmetric (H_y^s) and the antisymmetric (H_y^a)

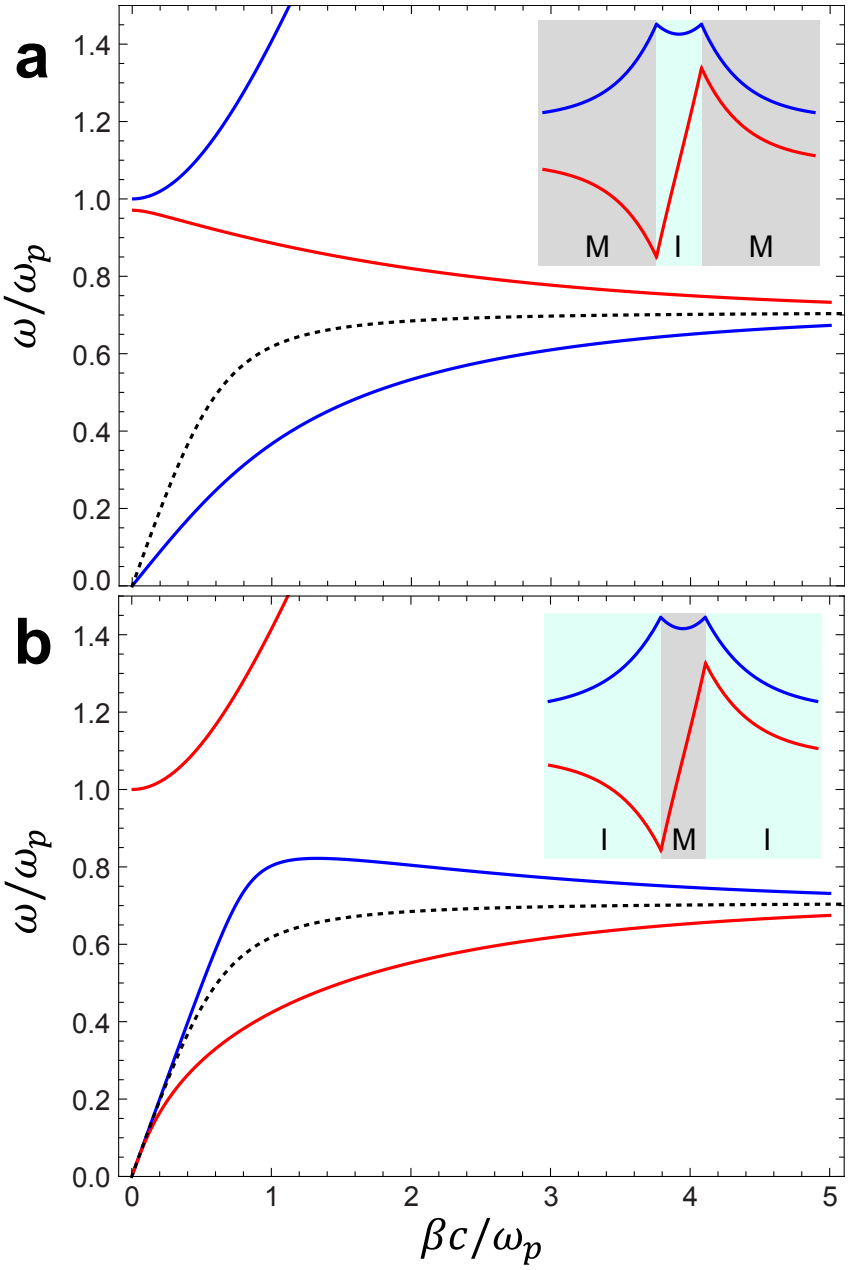

Figure 1.2: Dispersion relations of TM_0 (symmetric, blue solid) and TM_1 (antisymmetric, red solid) modes in (a) MIM and (b) IMI waveguides. Lossless ($\Gamma \approx 0$) Drude dispersion is assumed for the metal layers. The thickness of the core is chosen as $d = 0.5c/\omega_p$. The black dotted lines indicate the dispersion relation of the decoupled SPPs. The magnetic field profiles $H_y(x)$ for the eigenmodes are plotted in the insets

modes are

$$H_y^s(x,z) = \begin{cases} Ae^{i\beta z}\dfrac{\cosh(\gamma_1 x)}{\cosh\left(\gamma_1 d/2\right)} & \text{where } |x| < \dfrac{d}{2}, \\ \\ Ae^{i\beta z}\exp\left(-\gamma_2\left(|x| - \dfrac{d}{2}\right)\right) & \text{where } |x| > \dfrac{d}{2}, \end{cases} \tag{1.10}$$

$$H_y^a(x,z) = \begin{cases} Ae^{i\beta z}\dfrac{\sinh(\gamma_1 x)}{\sinh\left(\gamma_1 d/2\right)} & \text{where } |x| < \dfrac{d}{2}, \\ \\ \mathrm{sgn}(x)Ae^{i\beta z}\exp\left(-\gamma_2\left(|x| - \dfrac{d}{2}\right)\right) & \text{where } |x| > \dfrac{d}{2}, \end{cases} \tag{1.11}$$

where $\gamma_i = \sqrt{\beta^2 - k_0^2\epsilon_i}$ and β is the propagation constant. The boundary conditions at $x = \pm d/2$, H_y and E_z are continuous, yield the following dispersion relations.

$$\tanh\left(\gamma_1\frac{d}{2}\right) = -\frac{\gamma_2\epsilon_1}{\gamma_1\epsilon_2} \quad \text{TM}_0 \text{ (Symmetric)}, \tag{1.12}$$

$$\tanh\left(\gamma_1\frac{d}{2}\right) = -\frac{\gamma_1\epsilon_2}{\gamma_2\epsilon_1} \quad \text{TM}_1 \text{ (Antisymmetric)}, \tag{1.13}$$

$\epsilon_1 = \epsilon_d$ and $\epsilon_2 = \epsilon_m(\omega)$ for the MIM waveguide, whereas $\epsilon_1 = \epsilon_m(\omega)$ and $\epsilon_2 = \epsilon_d$ for the IMI waveguide.

For infinite core thickness $d \to \infty$, Eqs. (1.12) and (1.13) reduces to the SPP dispersion relation at a single interface Eq. (1.8), implying the SPPs at the two interfaces are decoupled. As the core layer becomes thinner, the dispersion relations of TM_0 (symmetric) and TM_1 (antisymmetric) modes deviate further away from the uncoupled SPP dispersion. Note that TM_0 mode has higher energy than TM_1 modes in MIM waveguides, whereas TM_1 modes are energetically favorable for IMI structures. Because the higher fraction of the energy resides in the metal, TM_1 (TM_0) modes tend to be more lossy than TM_0 (TM_1) modes in MIM (IMI) heterostructures. Unlike IMI structures, MIM structures do not support TM_1 modes at low frequencies. As a consequence, the dispersion relation of MIM TM_1 modes is qualitatively different

from the other plasmonic modes (Fig. 1.2).

By bringing the interfaces into close proximity to each other, MIM TM_1 modes and IMI TM_0 modes exhibit negative group velocity, $v_g = \partial\omega/\partial\beta < 0$, which is not observed for decoupled SPPs (Fig. 1.2). The negative group velocity arises from the fact that the direction of power flow in metal is opposite to that in dielectric materials, and the larger amount of power is conveyed in the metal layers. One can also interpret this phenomenon as a consequence of the negative Goos-Hänchen shifts at metal-dielectric interfaces [37].

In Chapter 2 we discuss on a more exotic example of dispersion engineering on plasmonic waveguides. A MIM waveguide is also a major building block of the graphene-based plasmonic waveguide modulator, which is presented in Chapter 5.

1.2 Relativistic Electrons in Graphene

Graphene is a two-dimensional honeycomb lattice of carbon atoms. This two dimensional allotrope of carbon is mechanically very strong, showing a breaking strength that is 200 times greater than steel with a Youngs modulus of 0.5 TPa from atomic force microscope experiments [33]. Graphene also exhibits an extremely high thermal conductivity of $\sim 5 \times 10^3$ W/mK [5]. Most importantly, graphene is a ballistic conductor exhibiting a remarkably high electron mobility exceeding 200,000 $\mathrm{cm^2V^{-1}s^{-1}}$ [10]. Therefore, it has been regarded as an ideal material for electronic applications.

In this section, we discuss on the electronic properties of graphene. We describe the tight binding model of graphene and explain how the charge carriers in graphene have relativistic nature. We then briefly introduce the field of electron optics, and remark that graphene is an excellent system for electron optics.[2]

1.2.1 Linear Dispersion Relation

Atomistic structure of the graphene has a hexagonal lattice with two carbon atoms per cell interconnected through covalent bonds. Among four valence electrons of

[2]Reference [13] provides a more detailed and through review on electronic properties of graphene.

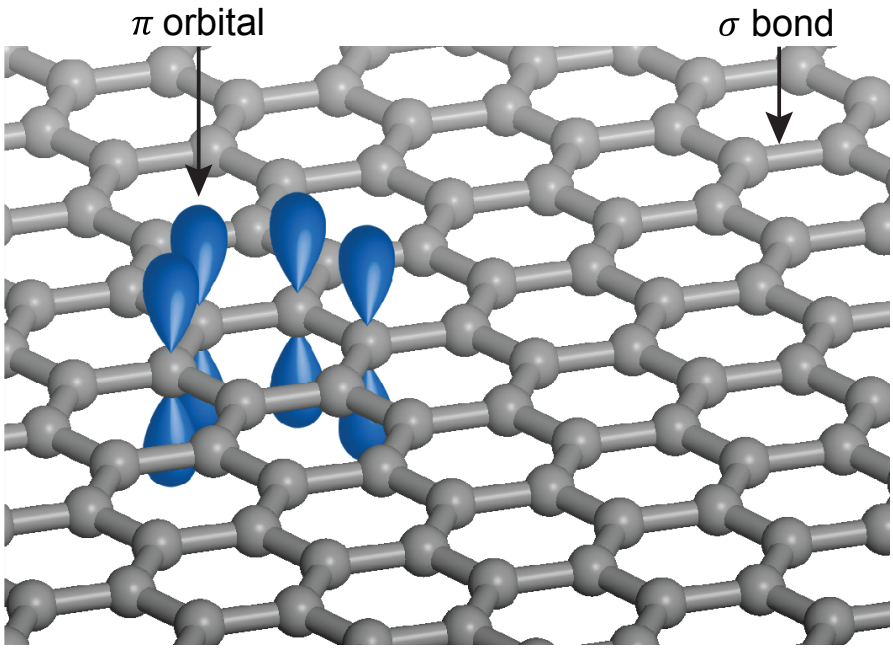

Figure 1.3: Graphene is a two-dimensional carbon allotrope forming a honeycomb lattice. Among four valence electrons of the carbon atom, three are used to make σ bonds with neighboring carbon atoms and the other is occupied in π orbital, which is orthogonal to the graphene sheet plane (i.e., sp^2 hybridization). These π electrons yielding an ideal 2DEG originates many intriguing electronic behaviors of the graphene.

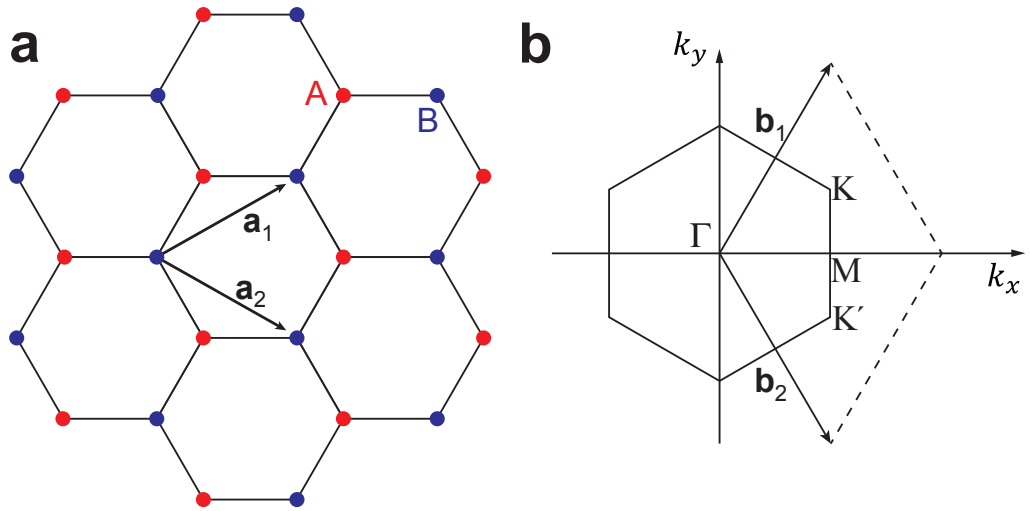

Figure 1.4: (a) Graphene honeycomb lattice. Within a unit cell, there are two basis atoms called as sublattice A (red dots) and sublattice B (blue dots). $\mathbf{a_1}$ and $\mathbf{a_2}$ are lattice unit vectors. (b) Brillouin zone with reciprocal lattice vectors of $\mathbf{b_1}$ and $\mathbf{b_2}$. Three high-symmetry points in the reciprocal space (Γ, M, and K) are shown.

each carbon, only three are involved in the covalent bonds (σ orbital) forming a honeycomb lattice while the other one is occupied in the orbital perpendicular to the graphene sheet (π orbital) as shown in Fig. 1.3 [13]. Many intriguing physical properties of the graphene are determined by the electrons near the Fermi energy of which wavefunction is composed of the linear combination of π orbitals. The lattice parameter of the graphene is given as

$$\mathbf{a_1} = \left(\frac{3a}{2}, \frac{\sqrt{3}a}{2}\right), \ \mathbf{a_2} = \left(\frac{3a}{2}, -\frac{\sqrt{3}a}{2}\right), \tag{1.14}$$

where a is the carbon-carbon distance of 1.42 Å(see Fig. 1.4(a)). This results a hexagonal shape of Brillouin zone (BZ) as shown in Fig. 1.4(b). Among the high symmetry points in BZ, two points located at the corners, $\mathbf{K}$ and $\mathbf{K}'$ are of importance, which are named as Dirac points. The momentum space positions of Dirac points are

$$\mathbf{K} = \left(\frac{2\pi}{3a}, \frac{2\pi}{3\sqrt{3}a}\right), \ \mathbf{K}' = \left(\frac{2\pi}{3a}, -\frac{2\pi}{3\sqrt{3}a}\right). \tag{1.15}$$

We assume that the electrons are tightly bound near the lattice points and can hop to nearest-neighbor sites, which is a realistic assumption because the overlap function between two π orbitals decays fast (compare Fig. 1.5(a) from nearest-neighbor hopping tight binding Hamiltonian and Fig. 1.5(b) from the density functional theory calculation). This leads a tight-binding Hamiltonian [13] of

$$H = -t \sum_{\langle i,j \rangle, \sigma} \left(a^{\dagger}_{\sigma,i} b_{\sigma,j} + \text{h.c.} \right), \tag{1.16}$$

where $a_{\sigma,i}(a^{\dagger}_{\sigma,i})$ is an annihilation (creation) operator of electron with spin σ on site i of the sublattice A, and $b_{\sigma,j}(b^{\dagger}_{\sigma,j}$ stands for the same operation on site j of sublattice B ($\hbar$ is set as unity for brevity). t is a nearest neighbor hopping energy which is around 2.8 eV. The bandstructure of the Hamiltonian (1.16)

$$E_{\pm}(\mathbf{k}) = \pm t \sqrt{3 + 2\cos\left(\sqrt{3} k_y a\right) + 4\cos\left(\frac{\sqrt{3}}{2} k_y a\right) \cos\left(\frac{3}{2} k_x a\right)}. \tag{1.17}$$

Electronic band of Eq. (1.17) is shown in Fig. 1.5(a). The energy value spectrum is symmetric around zero energy (meaning the electron-hole symmetry) and crosses at Dirac points. Eq. (1.17) can be expanded near Dirac points ($\mathbf{K}$ and $\mathbf{K}'$) with respect to the relative momentum vector $\mathbf{q} = \mathbf{k} - \mathbf{K}$:

$$E_{\pm}(\mathbf{q}) \approx v_F |\mathbf{q}|, \tag{1.18}$$

with the Fermi velocity of $v_F = 3ta/2 \approx 10^6$m/s and $|q| \ll |K|$. The linear dispersion relation of Eq. (1.18) is quite different from the usual quadratic dispersion relation of free electrons. This modification in dispersion relation results a significantly different electronic dynamics—it gives rise to massless and relativistic quasi-particle dynamics of charge carriers in graphene.

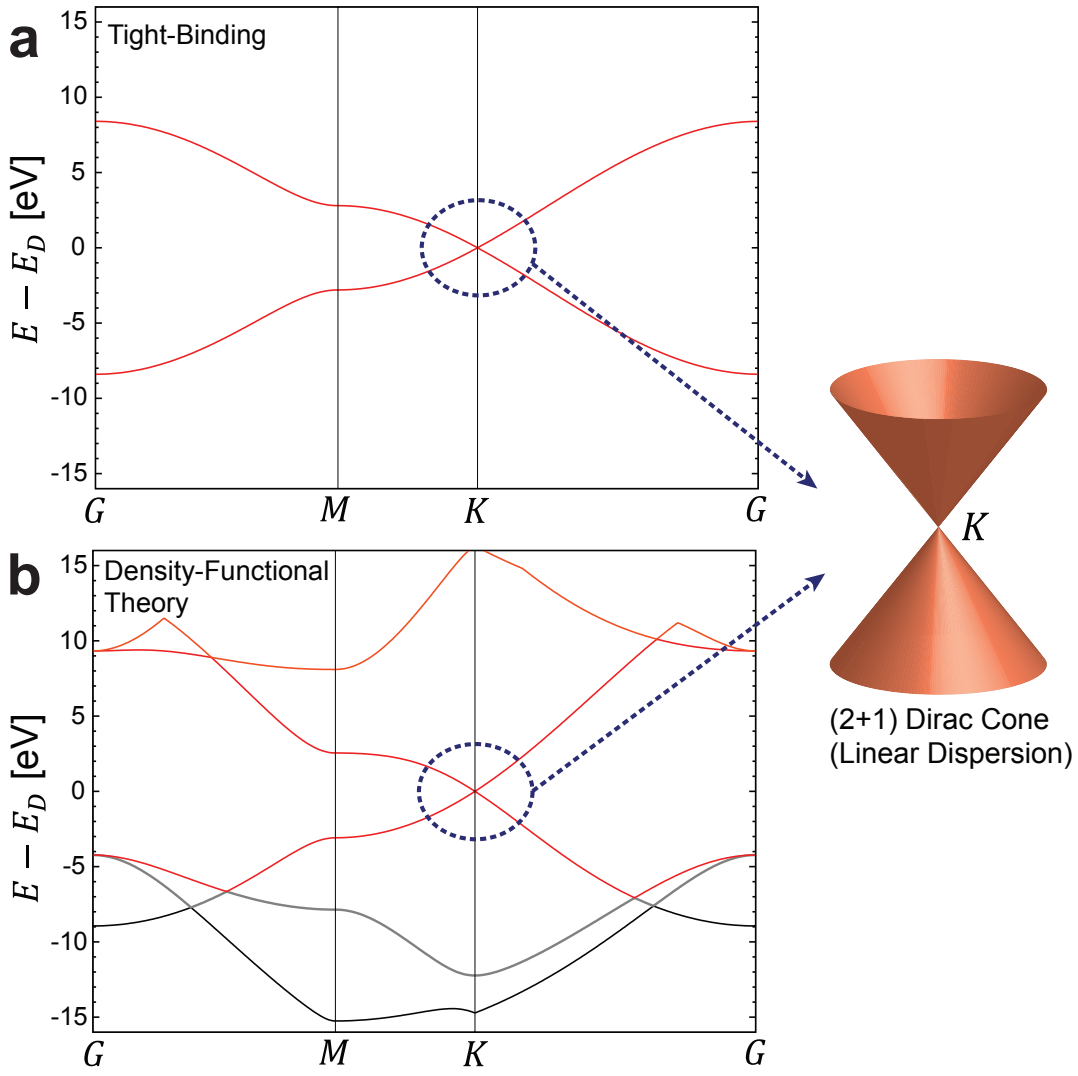

Figure 1.5: Electronic band structure of graphene calculated using (a) nearest-hopping tight-binding (TB) Hamiltonian (Eq. (1.17)) when $t = 2.8$eV, and (b) density-functional theory (DFT) calculation. TB results a good agreements with the more sophisticated result from DFT near the Dirac points while forming a (2+1) conical structure. For DFT calculations, we here used hybrid functional of B3LYP.

1.2.2 Massless Dirac Fermions

To describe the linear dispersion relation, one requires a Dirac equation describing relativistic dynamics of spin 1/2 particle instead of a Schrödinger equation. The cone shaped energy band (Fig. 1.5) makes the effective mass to be zero. Thus the carrier electron dynamics becomes effectively identical to the (2+1)-dimensional quantum electrodynamics (QED). The expansion of the tight-binding Hamiltonian of Eq. (1.16) up to a linear order in nearest-neighbor vectors yields an effective Hamiltonian of

$$H \approx -iv_F \int dxdy \left[\hat{\Psi}_1^\dagger(\mathbf{r})\boldsymbol{\sigma}\cdot\nabla\hat{\Psi}_1(\mathbf{r}) + \hat{\Psi}_2^\dagger(\mathbf{r})\boldsymbol{\sigma}^*\cdot\nabla\hat{\Psi}_2(\mathbf{r})\right], \tag{1.19}$$

where Pauli matrices $\boldsymbol{\sigma} = (\sigma_x, \sigma_y)$ and $\boldsymbol{\sigma}^* = (\sigma_x, -\sigma_y)$, and $\hat{\Psi}_i = (a_i, b_i)$. Here, the subscript 1 and 2 denote the $\mathbf{K}$ and $\mathbf{K}'$ points as shown in Fig. 1.4(b)) [13]. Thus, by introducing a electron wavefunction $\Psi = (\psi_1, \psi_2)$ with two-(pseudo)spin components around the $\mathbf{K}$ point, the graphene electron wavefunction can be described by using a two-dimensional Dirac-like equation:

$$-iv_F\boldsymbol{\sigma}\cdot\nabla\Psi(\mathbf{r}) = E\Psi(\mathbf{r}), \tag{1.20}$$

In momentum space, free graphene electron wavefunction $\Psi(\mathbf{k})$ near Dirac points of $\mathbf{K}$ or $\mathbf{K}'$ has the form of

$$\Psi_{\pm,\mathbf{K}}(\mathbf{k}) = \frac{1}{\sqrt{2}}\begin{pmatrix} e^{-i\theta_\mathbf{k}} \\ \pm e^{i\theta_\mathbf{k}} \end{pmatrix},\ \Psi_{\pm,\mathbf{K}'}(\mathbf{k}) = \frac{1}{\sqrt{2}}\begin{pmatrix} e^{i\theta_\mathbf{k}} \\ \pm e^{-i\theta_\mathbf{k}} \end{pmatrix}. \tag{1.21}$$

Similar to the usual QED systems, chirality of the graphene electronic eigenfunctions can be discussed. Here the chirality (or helicity) is defined as an inner product of the Pauli matrix ($\boldsymbol{\sigma}$) describing the pseudospin direction and the wavevector ($\mathbf{k}$) describing the momentum direction, and its eigenvalue can be either $+1/2$ or $-1/2$ for electrons (above the Fermi energy) or holes (below the Fermi energy), respectively.

The existence of the helicity quantum number dramatically changes the impurity scattering of graphene carriers. To preserve the chirality, the scattering event that

flips the momentum of the charge carrier from $+\mathbf{k}$ to $-\mathbf{k}$ should flip the direction of the pseudospin simultaneously, which is not possible if the Hamiltonian (1.19) is valid. This suppresses the backscattering of graphene carriers substantially, often referred to as Klein tunnelling [51], leading an extremely high carrier mobility.

1.2.3 Electron Optics in Graphene

Electronic analogues of optical behaviors such as focusing [90, 96, 102], collimation [72], and interference [108] have been achieved in two-dimensional electron gas (2DEG) systems. Bridging two fundamental physics, optics and electronics, has been made possible thanks to the ballistic transport properties of 2DEG. This has been cultivating new concepts for the manipulation of electrons in ways similar to that of photons in optical systems, which is referred as an "electron optics."

Graphene, the ideal 2DEG, is the most suitable system for electron optics. It has a substantially large carrier mean free path as large as a few microns [10], yielding a robust ballistic transport regime. Additionally, the two basis atoms with 3-fold symmetry in the graphene unit cell result in a semimetallic electronic band effectively described by a (2+1) dimensional Dirac cone. Therefore, the quasiparticles in graphene share several relativistic properties with photons, described by a (3+1) dimensional Dirac cone, although those two are intrinsically different from each other (e.g., graphene electrons are charged fermions but photons are uncharged bosons).

In Chapter 3 and 4, we explore the similarities and differences in behaviors of relativistic electrons in graphene and electromagnetic waves in optical systems.

1.3 Graphene as a Tunable Plasmonic Material

Recently, researchers have noticed that a single layer of graphene can support plasmons at infrared frequencies with an extremely high confinement factor ($\sim$ 100) without too much propagation loss [41]. Subsequent experimental endeavors have demonstrated the evidences of the existence of graphene plasmons by measuring the

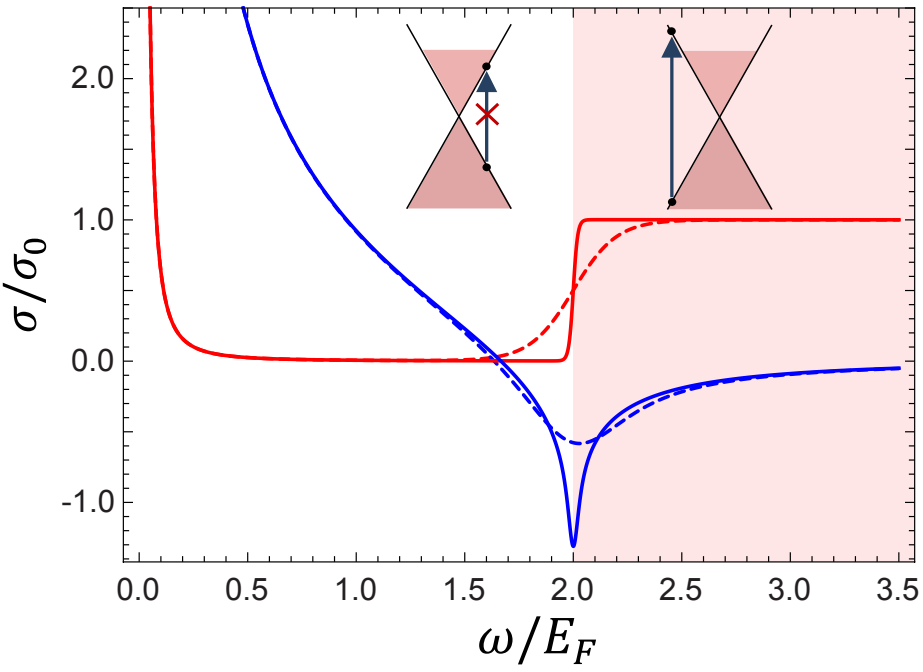

Figure 1.6: Optical conductivity of graphene, in units $\sigma_0 = e^2/4\hbar$, as a function of frequency ω. The real part ($\mathrm{Re}\{\sigma\}$, red) and the imaginary part ($\mathrm{Im}\{\sigma\}$, blue) are plotted for $T/E_F = 0.005$ (solid) and 0.05 (dashed). The red shaded area denote the regime of interband excitations.

plasmon resonance of graphene nanoribbon arrays [46], and by acquiring their near field images [17, 32].

In this section, we focus on graphene as a plasmonic material. We discuss on the optical conductivity of graphene and then derive the properties of plasmons in graphene.[3]

1.3.1 Optical Conductivity of Graphene

The optical conductivity $\sigma(\omega)$ of graphene consists of the intraband σ_{intra} and the interband σ_{inter} contributions. Neglecting the spatial dispersion, σ_{intra} and σ_{inter} can be analytically written as follows within the random phase approximation (RPA) [30, 31].

$$\sigma_{\mathrm{intra}}(\omega) = \frac{e^2\omega}{i\pi\hbar}\int_{-\infty}^{\infty} d\epsilon \frac{|\epsilon|}{\omega^2}\frac{df(\epsilon)}{d\epsilon} = \frac{2ie^2T}{\pi\hbar(\omega+i\Gamma)}\ln\left[2\cosh(E_F/2T)\right], \tag{1.22}$$

[3]References [30, 92] derives the AC electrical conductivity of graphene. A more detailed discussion on the properties of graphene plasmons is provided in Ref. [41].

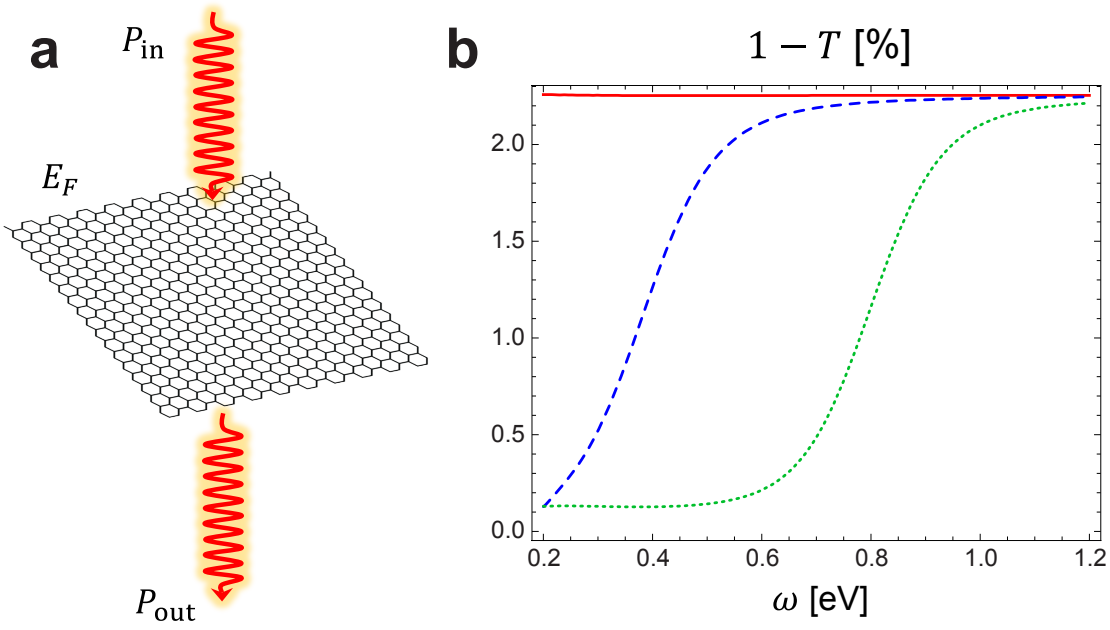

Figure 1.7: (a) Schematic of a transmission measurement through a single layer graphene. (b) Numerically simulated spectra $1-T$ for $E_F = 0.01$eV (red solid), 0.2eV (blue dashed), and 0.4eV (green dotted), assuming room temperature. Note that the absorption abruptly increases at $\omega = 2E_F$ and becomes constant($\sim \pi e^2/\hbar c$) for higher photon energies, as a result of interband transitions.

$$\sigma_{\text{inter}}(\omega) = \frac{ie^2\omega}{\pi\hbar}\int_0^\infty d\epsilon \frac{f(-\epsilon)-f(\epsilon)}{(\omega+i\delta)^2-4\epsilon^2}, \tag{1.23}$$

where $f(\epsilon) = 1/(\exp[(\epsilon - E_F)/T]+1)$ is the Fermi distribution function, and Γ is the scattering rate of carriers. More general expression for the conductivity tensor with non-negligible spatial dispersion is given in Ref. [30]. In low temperature limit, $T \ll E_F$, σ_{intra} recovers the Drude from,

$$\sigma_{\text{intra}}(\omega) = \frac{ie^2|E_F|}{\pi\hbar(\omega+i\Gamma)}. \tag{1.24}$$

σ_{inter} is also further reduced, yielding

$$\sigma_{\text{inter}}(\omega) = \frac{e^2}{4\hbar}\left[\theta(\omega-2E_F) - \frac{i}{\pi}\ln\left|\frac{\omega+2E_F}{\omega-2E_F}\right|\right], \tag{1.25}$$

where θ is the Heaviside step function.

The real part of the conductivity shows a step at $\omega = 2E_F$, which corresponds to the onset of the interband transition (Fig. 1.6). In other words, when $\omega > 2E_F$, the optical loss in graphene is dominated by the interband transition. As an interesting consequence, the optical transmittance of a free-standing graphene also has a step at $\omega \approx 2E_F$ and becomes flat for higher frequencies (Fig. 1.7). The optical transmittance at $\omega > 2E_F$ can be analytically expressed as [54]

$$T_{\text{opt}} = \left(1 + \frac{\pi e^2}{2\hbar c}\right)^{-2} \approx 1 - \frac{\pi e^2}{\hbar c} \approx 0.977. \tag{1.26}$$

For $\omega < 2E_F$, the optical loss in graphene is determined by various electron scattering processes. Electron-impurity scattering dominates at low frequencies, and the scattering rate Γ_{imp} can be estimated from DC mobility μ, such as $\Gamma_{\text{imp}} = e\hbar v_F^2/\mu E_F$. Electron-optical phonon scattering becomes significant above the phonon energy $\omega_{ph} \sim 0.2$eV [41].

1.3.2 Plasmons in Graphene

A layer of graphene supports plasmons. Similar to Section 1.1.2, we obtain the field profile and the dispersion relation of graphene plasmons by solving the Maxwell's equations. Here we consider TM modes in graphene, which lies on $x = 0$ plane, sandwiched by dielectric media of permittivity ϵ_1 and ϵ_2.[4] We again use Eq. (1.6) as the ansatz for the magnetic field $H_y(x, z)$. The boundary condition, however, is quite different, because there is a sheet current σE_z flowing along the graphene layer, which induces a discontinuity in the magnetic field.

$$E_z\left(x \to 0^+\right) = E_z\left(x \to 0^-\right), \tag{1.27}$$

$$H_y\left(x \to 0^+\right) - H_y\left(x \to 0^-\right) = \sigma E_z(x = 0). \tag{1.28}$$

[4]Graphene also supports TE modes at $1.667 < \omega/E_F < 2$. See Ref. [68] for details.

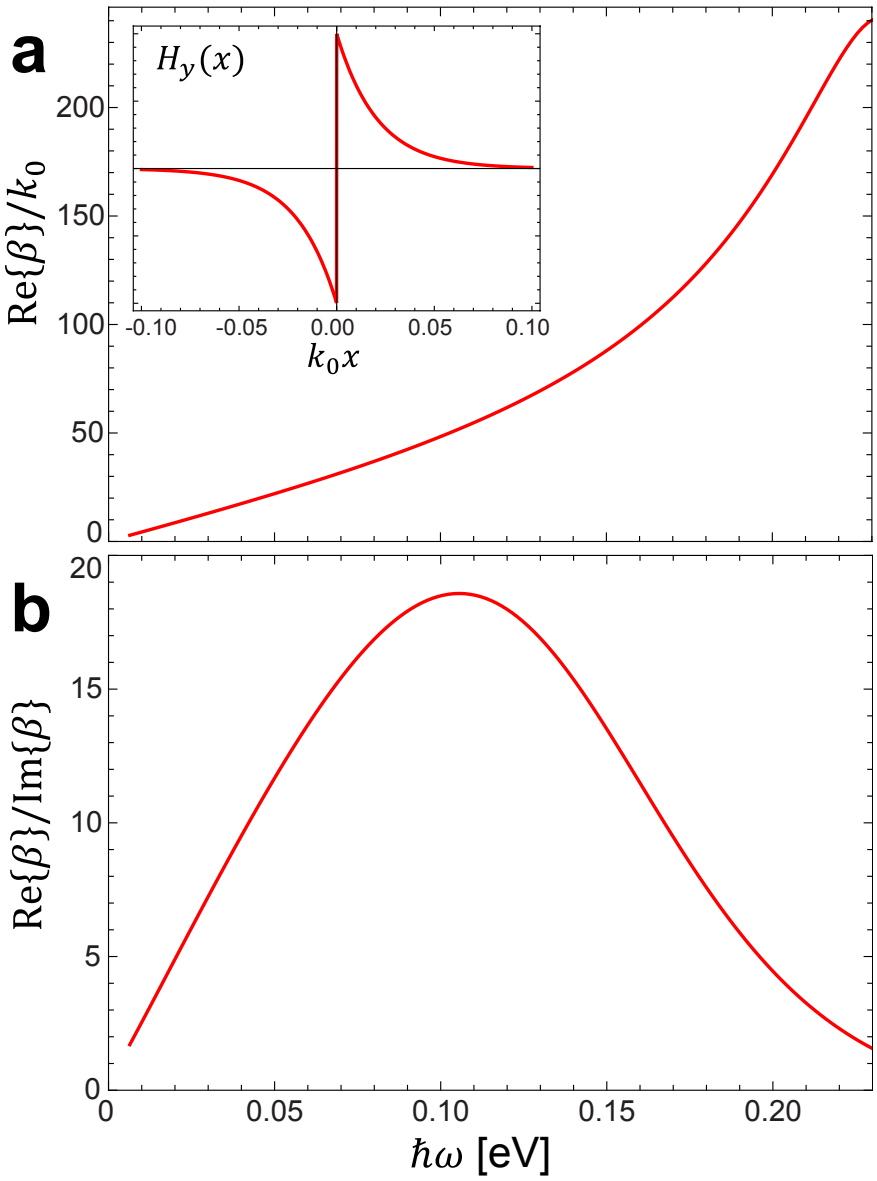

Figure 1.8: (a) Field localization $\mathrm{Re}\{\beta\}/k_0$ and (b) normalized propagation loss $\mathrm{Re}\{\beta\}/\mathrm{Im}\{\beta\}$ of plasmons in a suspended graphene ($\epsilon_1 = \epsilon_2 = 1$) for $E_F = 0.16$eV, $T = 300$K, and $\Gamma = 4.1$meV, which corresponds to the mobility μ of $10^4\mathrm{cm}^2\mathrm{V}^{-1}\mathrm{s}^{-1}$. The magnetic field profile at $\omega = 0.1\mathrm{eV} \approx 13\mu\mathrm{m}$ is plotted in the inset of (a).

The dispersion relation for graphene plasmons is then analytically written as

$$\frac{\epsilon_1}{\sqrt{\beta^2 - \epsilon_1 k_0^2}} + \frac{\epsilon_2}{\sqrt{\beta^2 - \epsilon_2 k_0^2}} = -i\frac{\sigma}{\omega\epsilon_0}. \tag{1.29}$$

In non-retarded regime ($\beta \gg \omega/c$), the above equation is further simplified, yielding

$$\beta \approx i\frac{(\epsilon_1 + \epsilon_2)\epsilon_0\omega}{\sigma}. \tag{1.30}$$

At frequencies much lower than the interband threshold yet much higher than the scattering rate ($\Gamma \ll \omega \ll 2E_F$), σ is inversely proportional to ω (see Eq. (1.24)). The dispersion relation for low energy plasmons is thus $\beta \propto \omega/\sigma \propto \omega^2$, or $\omega \propto \sqrt{\beta}$. Note that the low energy dispersion of SPPs on metals is $\omega \propto \beta$ (Fig. 1.1). This qualitative difference is originated from the differences in electronic dispersions—linear for graphene and quadratic for bulk metals.

Figure 1.8 plots the field localization and the normalized propagation loss of plasmons in a suspended graphene ($\epsilon_1 = \epsilon_2 = 1$) as a function of frequency, assuming $E_F = 0.16$eV, $T = 300$K, and $\Gamma = 4.1$meV, which corresponds to the mobility of $10^4\text{cm}^2\text{V}^{-1}\text{s}^{-1}$ [74]. The field confinement factor is calculated to be around 30–100 with reasonable losses $\text{Re}\{\beta\}/\text{Im}\{\beta\} > 10$. From Eq. (1.30), we know that the field localization can be readily enhanced by factor of $(1 + \epsilon_d)/2$ by placing graphene on a dielectric substrate of permittivity of ϵ_d. The effect of interband transition become significant for high frequencies, resulting in substantial propagation losses. By increasing E_F, it is possible to achieve much longer propagation lengths, $\text{Re}\{\beta\}/\text{Im}\{\beta\}$ 100 [41]. The mobility of $10^4\text{cm}^2\text{V}^{-1}\text{s}^{-1}$ can be improved by employing hexagonal boron nitride substrates, even up to $10^6\text{cm}^2\text{V}^{-1}\text{s}^{-1}$ [21, 66]. This may further reduces the plasmon losses.

In Chapter 5 and 6, we discuss physics of graphene plasmon cavities, and demonstrate how to utilize them in photonic device applications.

1.4 Scope of This Thesis

This thesis discusses five interrelated topics on plasmonic dispersion engineering, graphene electron optics, and graphene plasmonics. The chapters are organized as follows:

Braodband Slow Light in Tapered Plasmonic Waveguide

As an example of plasmonic dispersion engineering, Chatper 2 describes "rainbow trapping" structures, which has been proposed as a scheme for localized storage of broadband electromagnetic radiation in metamaterials and plasmonic heterostructures. We articulate the dispersion and power flow characteristics of rainbow trapping structures, and show that tapered waveguide structures composed of dielectric core and metal cladding are best suited for light trapping. A metal/insulator/metal taper acts as a cascade of optical cavities with different resonant frequencies, exhibiting a large quality factor and small effective volume comparable to conventional plasmonic resonators.

Electron Optics in Graphene

Chapter 3 presents a few examples of electron optics in graphene. We investigate the temporal behavior of a single localized electron wavepacket, showing that it exhibits optics-like dynamics including the Goos-Hänchen effect at a heterojunction and the Rainbow trapping effect in a tapered electron waveguide, but the behavior is quantitatively different than for electromagnetic waves. To study the dynamics of graphene electrons numerically, we develop a finite difference time domain (FDTD) method for simulating the dynamics of graphene electrons, denoted GraFDTD.

Graphene Field Effect Transistor without Energy Gap

Inspired by plasmonic dispersion engineering, exemplified in Chapter 2, Chapter 4 describes a way to enhance electron backscattering in graphene by engineering the

dispersion of electron eigenmodes in a Kronig-Penney potential. A major complication in realizing graphene based field effect transistors for logic applications is that the electrons in pristine graphene exhibit unimpeded Klein tunnelling through gate potential barriers. Introducing a band gap in graphene suppresses Klein tunnelling, but inevitably degrades the carrier mobility. To solve this dilemma, we propose a gating mechanism employing a sawtooth-shaped gate potential geometry (in place of the conventional bar-shaped geometry) that leads to a hundredfold enhancement in on/off transmission ratio for normally incident electrons without any band gap engineering.

Graphene Subwavelength Waveguide Modulator

Chapter 5 presents a scheme for modulating mid-infrared transmission of plasmonic waveguides by employing the Fano interference between transmission through plasmon resonance in graphene and nonresonant background transmission. We demonstrate that the overall transmission can be almost completely suppressed by total destructive interference, which is ideal for switching applications. Because of the high field confinement of graphene plasmons, the effective volume of the structure is much smaller than the free space wavelength.

Graphene Nano Cavities at Near-Infrared Frequencies

Chapter 6 experimentally examines the properties of plasmon resonance in graphene nanocavity arrays on SiO_2 using the FTIR spectroscopy. The system exhibits multiple resonance peaks originated from the coupling with surface phonons in SiO_2 substrate. By changing the size and the Fermi energy of the ribbon arrays, the resonance frequency ω_{res} was tuned from 0.16 to 0.26eV. The width of the resonance becomes broader due to the electron-optical phonon coupling as ω_{res} passing over ω_{Oph}. We also predict that ω_{res} can be further increased and even reach to the telecommunication bands with a reasonable quality factor by decreasing the size of the cavity and raising E_F sufficiently.

Chapter 2

Plasmonic Dispersion Engineering: Trapped Rainbow in Tapered Plasmonic Waveguide

"Rainbow trapping" has been proposed as a scheme for localized storage of broadband electromagnetic radiation in metamaterials and plasmonic heterostructures. Here, we articulate the dispersion and power flow characteristics of rainbow trapping structures, and show that tapered waveguide structures composed of dielectric core and metal cladding are best suited for light trapping. A metal/insulator/metal taper acts as a cascade of optical cavities with different resonant frequencies, exhibiting a large quality factor and small effective volume comparable to conventional plasmonic resonators.[1]

2.1 Introduction

Slow electromagnetic waves, first studied in systems with atomic coherence at low temperature [59], have been investigated in recent years at room temperature via light dispersion in solid state media such as photonic crystals [34, 104]. However most of these systems operate only at specific resonant frequencies, and so broadband light trapping remains a great challenge. Tsakmakidis et al. first proposed "rainbow trapping" in which a wide wavelength range of electromagnetic fields can be trapped in

[1]This chapter is a slightly modified version of Ref. [43].

tapered waveguide structures composed of negative index core and dielectric cladding (insulator-negative index-insulator, or INI) that exhibits a negative Goos-Hänchen effect [98]. Recently, researchers have determined that such trapping mechanism is also applicable for transverse magnetic (TM) waves in insulator-metal-insulator (IMI) and metal-insulator-metal (MIM) waveguide tapers under certain material property conditions [63, 79]. However, to date the question of how much light a rainbow trapping structure can actually store and how the light escapes from it has not been addressed.

In this work, we study fundamental mode conversion and loss mechanisms of linearly-tapered INI, IMI, and MIM rainbow trapping structures and show that MIM rainbow trapping structures are superior to the others in terms of trapping performance. Assuming a Drude dispersion relation for the cladding metal, we specify the frequency range and the structural dimensions needed to achieve rainbow trapping and calculate the quality factor Q and the effective mode area A_{eff} as quantitative measures of light trapping and localization. We perform a transfer matrix analysis [110] to examine the behavior of the guided modes in the structure, and confirm the results with full-wave finite difference time domain (FDTD) and finite element method (FEM) simulations. This chapter is organized as follows: Fig. 2.2 illustrates the mode conversion properties of IMI, INI and MIM tapers. We then compare the energy density distributions and modal amplitudes achievable for IMI TM_0 modes and MIM TM_2 modes, as indicated in Fig. 2.3. For MIM tapers, we then investigate the critical taper thickness for mode conversion and the quality factor achievable for the quasi-bound mode as a function of frequency. Finally we explore the properties of rainbow tapers as a function of taper angle, as illustrated by Fig. 2.5.

2.2 Transfer Matrix Analysis

We discretize the taper of length L as a series of N parallel waveguide segments of equal length $\Delta z = L/N$ whose eigenmodes are analytically given (see Fig. 2.1). In each segment, each eigenmode simply propagates without coupling. At the interfaces,

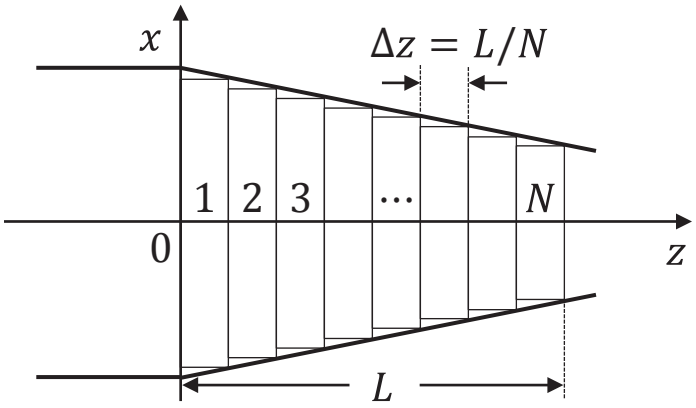

Figure 2.1: Waveguide discretization for transfer matrix calculation.

the modes are partially transmitted and partially reflected. We can analytically obtain the coupling coefficients from the field continuity conditions and the orthogonality relations. This can be conveniently expressed in matrix form, $\mathbf{a}^{j+1} = \mathbf{S}^j \mathbf{T}^j \mathbf{a}^j$. Here, $\mathbf{a}^j = \left\{a^j_{f+}, a^j_{f-}, a^j_{b+}, a^j_{b-}\right\}$ the vector whose elements are the mode amplitudes in j-th waveguide segment, and $\mathbf{T}^j$ and $\mathbf{S}^j$ are 4×4 transfer matrices,respectively describing the propagation of the modes in the segment and the intermode coupling at the interface between j-th and $(j+1)$-th segments.

$$\mathbf{T}^j_{lm} = \delta_{lm} \exp\left(ik_0 n_l \Delta z\right), \tag{2.1}$$

$$\mathbf{S}^j_{lm} = \frac{\int \left(\mathbf{e}^{j+1}_l \times \mathbf{h}^j_m\right)_z + \int \left(\mathbf{e}^j_m \times \mathbf{h}^{j+1}_l\right)_z}{2 \int \left(\mathbf{e}^j_m \times \mathbf{h}^j_m\right)_z}, \tag{2.2}$$

where $\mathbf{e}$ and $\mathbf{h}$ are the vector waveguide modes such that $\mathbf{E} = a\mathbf{e}$ and $\mathbf{H} = a\mathbf{h}$. Expanding this argument to the entire series of waveguide segments, the mode amplitudes of the taper ends are related by

$$\mathbf{a}^N = \prod_{j=1}^{N} \mathbf{S}^j \mathbf{T}^j \mathbf{a}^1. \tag{2.3}$$

The mode amplitudes are normalized such that $|\mathbf{a}|^2 = |\int dx (\mathbf{E} \times \mathbf{H})_z / 2|$, where $\mathbf{E}$ and $\mathbf{H}$ are electric and magnetic fields of the corresponding mode. Note that, for

modes having real propagation constants, $|\mathbf{a}|^2$ is simply the time-averaged power flow.

2.3 Mode Conversion Mechanism

2.3.1 Dispersion Relation of Guided Modes

The dispersion relations of eigenmodes in rainbow trapping systems are exotic. Figures 2.2(d)–(f), respectively, show the effective indices n_{eff} of IMI TM_0 modes and modes in INI and MIM tapers as a function of core thickness α. For all three cases, the modes consist of two branches; the energy velocity,

$$v_E = \frac{\int S_z dx}{\int u dx}, \tag{2.4}$$

where u and $\mathbf{S}$ are the time averaged energy density [85] and Poynting vector, and the phase velocity are parallel for one branch ($|f\rangle$) and antiparallel for the other ($|b\rangle$), as seen in Figs. 2.2(g)–(i). Since each mode can propagate along either the $+z$ or $-z$ direction, there exist a total of four orthogonal eigenmodes $|f+\rangle$, $|f-\rangle$, $|b+\rangle$ and $|b-\rangle$. The letters f and b identify the branch and the signs $+$ and $-$ indicate the direction of energy propagation. If the system is adiabatic enough to neglect the coupling between these modes and higher order modes, it is possible to describe the system as a linear superposition of these four basis modes. The $|f\rangle$ and $|b\rangle$ are degenerate at a certain core thickness, α_d, and the dispersion relations splits as α deviates from α_d. It is worth noting that the direction of power flow through the cladding is opposite to the flow through the core and their magnitudes become equal at $\alpha = \alpha_d$ which results in zero energy velocity. The conditions for having degeneracy points are specified in Table 2.1 [63, 79].

2.3.2 Mode Conversion in Rainbow Trapping Structures

Many simulation results have shown that it is impossible to trap light to a complete standstill even under the assumption of lossless materials [40, 44, 63]. This results

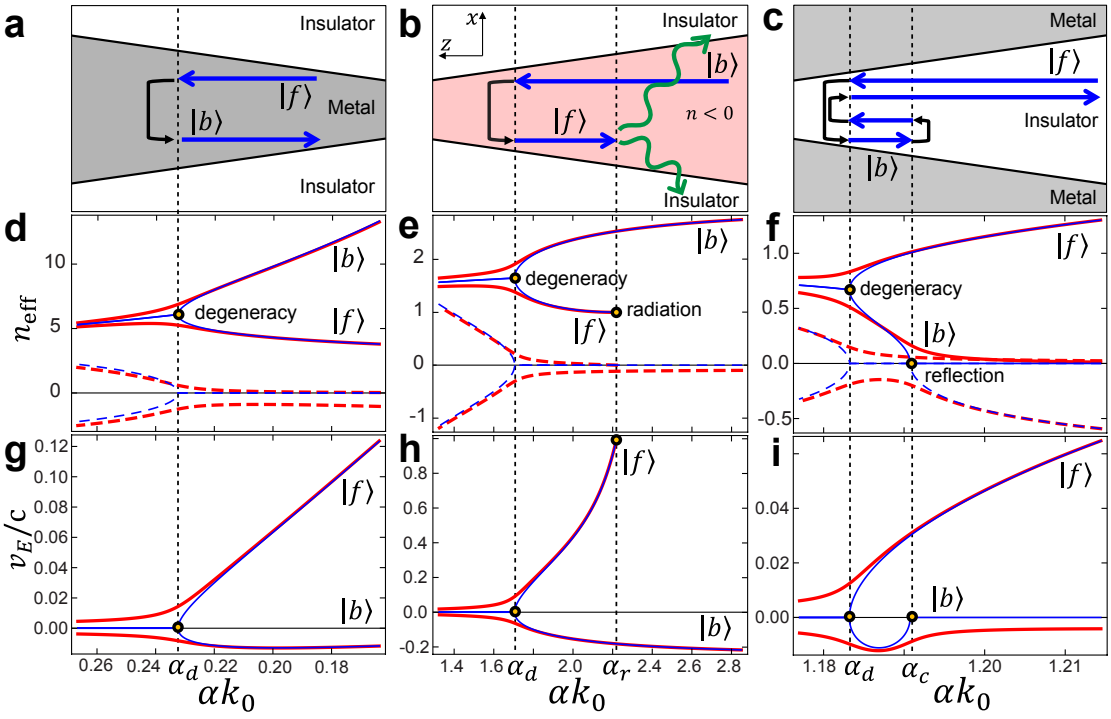

Figure 2.2: Schematic descriptions of (a)–(c) mode conversion mechanism, (d)–(f) n_{eff}, and (g)–(i) v_E of IMI($\epsilon_{\text{I}} = -8.5$, $\epsilon_{\text{II}} = 10$) TM_0, INI($\epsilon_{\text{I}} = \mu_{\text{I}} = -3$, $\epsilon_{\text{II}} = \mu_{\text{II}} = 1$) TM_2, and MIM($\epsilon_{\text{I}} = 10$, $\epsilon_{\text{II}} = -1$) TM_2 modes versus αk_0. In (d)–(f), real part and imaginary part of n_{eff} are represented as solid and dashed curves respectively. Lossless and lossy($\text{Im}\{\epsilon\}/\text{Re}\{\epsilon\} = 0.03$ for metal and $\text{Im}\{\epsilon\}/\text{Re}\{\epsilon\} = \text{Im}\{\mu\}/\text{Re}\{\mu\} = 0.03$ for negative index metamaterial) cases are plotted as thin blue and thick red curves, respectively in (d)–(i). Dotted vertical lines indicate degeneracy point α_d, radiation point α_r, and the mode cutoff α_c.

INI, NIN	MIM	IMI
TM_0: $\sigma_\epsilon > \max\{1, \sigma_\mu^{-1}\}$	TM_1: $1 < \sigma_\epsilon < 1.13510$	TM_0: $\sigma_\epsilon > 1$
TM_1: $1 < \sigma_\epsilon < \sigma_\mu^{-1}$	$\mathrm{TM}_{m\geq 2}$: $\sigma_\epsilon^{-1/2} + \mathrm{atan}(\sigma_\epsilon^{-1/2}) > m\pi/2$	
$\mathrm{TM}_{m\geq 2}$: $\sigma_\epsilon\sigma_\mu < 1$		

Table 2.1: The conditions for rainbow trapping. $\sigma_\epsilon = |\epsilon_{\mathrm{II}}/\epsilon_{\mathrm{I}}|$ and $\sigma_\mu = |\mu_{\mathrm{II}}/\mu_{\mathrm{I}}|$ where the subscripts I and II denote the core and the cladding respectively. For INI TE modes, replace $\sigma_\epsilon \leftrightarrow \sigma_\mu$.

from the coupling between the eigenmodes due to the fundamental nonadiabaticity near $\alpha = \alpha_d$. More specifically, the slow core thickness variation condition [93], $d\alpha/dz \ll \alpha k_0 \Delta n/\pi$, where k_0 is the wavenumber in the free space and Δn is the effective index difference between eigenmodes, can never be fulfilled throughout the entire structure because $\Delta n = 0$ at the degeneracy point. In fact, the degeneracy point connects $|f\pm\rangle$ to $|b\mp\rangle$. Mechanisms for power flow into and out of rainbow trapping structures are schematically described in Figs. 2.2(a)–(c). An incident IMI TM_0 $|f+\rangle$ is converted to the other branch $|b-\rangle$ at $\alpha = \alpha_d$ and escapes the structure. In an INI structure, an incident photonic $|b+\rangle$ is converted to $|f-\rangle$ at $\alpha = \alpha_d$ and couples into a backward propagating radiative mode at $\alpha = \alpha_r$, where n_{eff} coincides with the index of the cladding. An incident MIM photonic $|f+\rangle$ undergoes similar mode conversion at the degeneracy point but the converted $|b-\rangle$ is reflected to $|b+\rangle$ at the mode cutoff $\alpha = \alpha_c$, and converted back to $|f-\rangle$, which finally escapes the structure. The reflection at $\alpha = \alpha_c$, where the energy velocity also vanishes, makes electromagnetic waves reside longer in the taper segment between the degeneracy point and the mode cutoff.

One can intuitively sketch out the mode conversion mechanism in an analogous ray optic picture. A light ray incident upon a core/cladding interface at an angle of incidence Θ_0 undergoes total internal reflection with negative Goos-Hänchen shift, propagates in the core, and strikes the other interface with angle $\Theta_0 - \theta$, where θ is the taper angle. Since the successive angle of incidence $\Theta_N = \Theta_0 - N\theta$ decreases as the number of bounces N increases, the lateral propagation of the ray between two

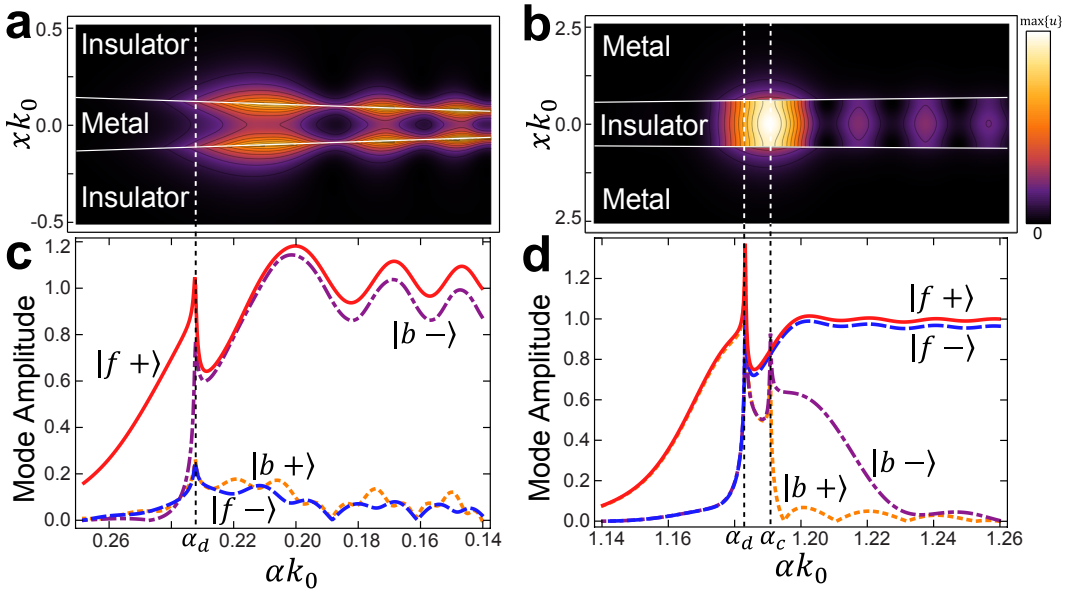

Figure 2.3: Energy density distribution $u(x, z)$ of (a) IMI ($\epsilon_{\mathrm{I}} = -8.5$, $\epsilon_{\mathrm{II}} = 10 + 0.01i$) TM_0 and (b) MIM ($\epsilon_{\mathrm{I}} = 10$, $\epsilon_{\mathrm{II}} = -1 + 0.001i$) TM_2 modes. Boundaries between core and claddings are indicated by white solid lines. (c),(d) Mode amplitudes of $|f+\rangle$ (red solid), $|f-\rangle$ (blue dashed), $|b+\rangle$ (orange dotted), and $|b-\rangle$ (purple dash-dotted) modes as functions of core thickness in the (c) IMI and (d) MIM structures. Dotted vertical lines indicate α_d and α_c.

consecutive Goos-Hänchen shifted internal reflections also decreases, crosses zero, and becomes negative which corresponds to our mode conversion description at $\alpha = \alpha_d$. For INI structures, the light ray escapes the structure in the form of radiation once Θ_N reaches the angle of escape Θ_r determined by Snell's law (Fig. 2.2(b)). Therefore a ray can bounce M times, where M is the largest integer satisfying $\Theta_M > \Theta_r$ (i.e., $M \sim (\Theta_0 - \Theta_r)/\theta$). On the other hand, in MIM structures, the light ray is always totally reflected at the interface. Therefore Θ_N can be further reduced and cross zero at the mode cutoff ($\alpha = \alpha_c$) (Fig. 2.2(c)). From there, the ray travels back in the $+z$ direction again and then repeats the same process that we described previously but in the reverse manner. The number of internal reflections is thus $M \sim 2\Theta_0/\theta$, which is greater than that of the INI case.

We perform a transfer matrix analysis to quantitatively understand the behavior of the modes in the IMI and MIM rainbow trapping structure by computing the amplitude of the eigenmodes. Figure 2.3(c) shows the mode amplitudes of IMI TM_0

modes in the steady state. Corresponding to our previous description, a_{f+} and a_{b-} are of similar magnitude whereas a_{f-} and a_{b+} are very small, which indicates mode conversion from $|f+\rangle$ to $|b-\rangle$, with other modes suppressed. On the other hand, for MIM TM_2 mode trapping, $|a_{f+}| \sim |a_{f-}|$ where $\alpha > \alpha_c$ and $|b+\rangle$ and $|b-\rangle$ are excited only in the taper section $\alpha \in (\alpha_d, \alpha_c)$ and decay as they become evanescent (Fig. 2.3(d)). Due to the simultaneous excitation of $|f+\rangle$, $|f-\rangle$, $|b+\rangle$ and $|b-\rangle$, an MIM structure can store large amounts of energy which makes them the best candidates for trapping light. Although an IMI structure can perform as a compact mode converter, its light trapping capability is inferior to the MIM trapping structure because it does not exhibit mode cutoff (Figs. 2.3(a) and (b)). Due to the inevitable radiation loss, in addition to the difficulties in fabrication, INI rainbow trapping seems less attractive compared to the other approaches. Therefore, we focus our attention on MIM rainbow trapping in the rest of the discussion.

2.4 Performance of MIM Rainbow Tapers

2.4.1 MIM TM_2 Mode Trapping

Although rainbow trapping structures are open systems, they can be considered as a series of optical cavities having different resonant frequencies since they can localize broadband light in tapered sections of different width depending on frequency. Assuming a dispersionless dielectric core and a Drude metal cladding of

$$\epsilon_{\mathrm{II}} = 1 - \frac{\omega_p^2}{\omega^2 + i\Gamma\omega}, \tag{2.5}$$

where ω_p and Γ are the plasma frequency and the damping constant respectively, TM_2 modes at frequency

$$\frac{\omega}{\omega_p} \in \left((0.2430\epsilon_{\mathrm{I}} + 1)^{-1/2}, 1\right) \tag{2.6}$$

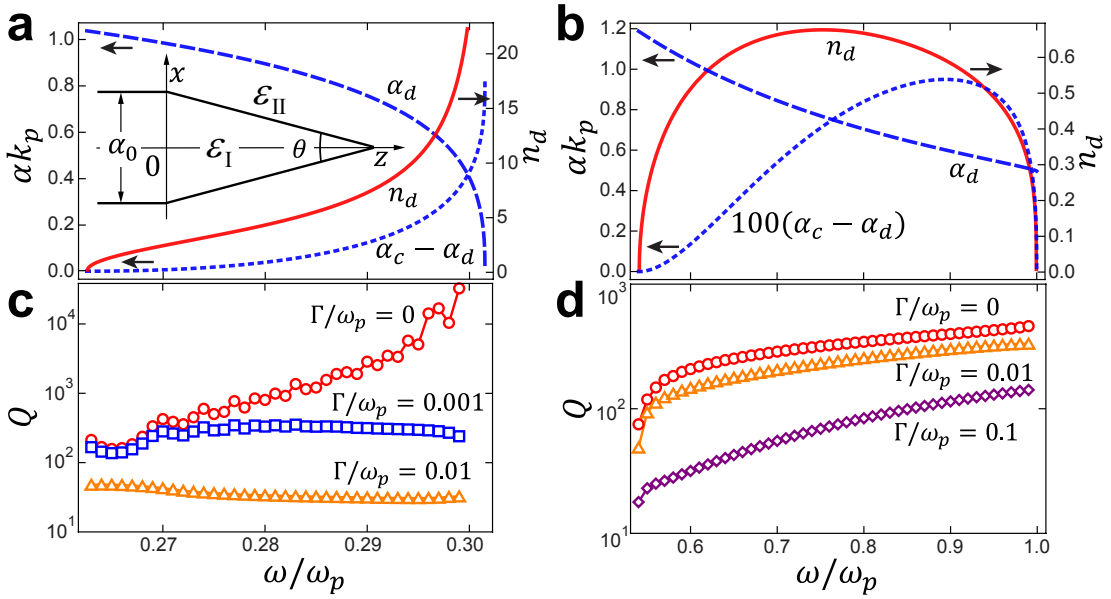

Figure 2.4: α_d (blue dashed), $\alpha_c - \alpha_d$ (blue dotted, 100 times magnified in (b)) and n_d, the effective phase index of the mode at $\alpha = \alpha_d$ (red solid) of MIM ($\epsilon_{\mathrm{I}} = 10$, $\theta = 2^\circ$) (a) TM_1 and (b) TM_2 modes versus ω/ω_p. α_d and α_c are normalized by $k_p^{-1} = c/\omega_p$. The inset in (a) shows the schematic of a MIM rainbow trapping structure. Q versus ω/ω_p of (c) TM_1 modes for $\Gamma/\omega_p = \{0$ (red circles), 0.001(blue squares), 0.01(orange triangles)$\}$ and (d) TM_2 modes for $\Gamma/\omega_p = \{0$ (red circles), 0.01(orange triangles), 0.1(purple diamonds)$\}$.

can be trapped in the structure (Table 2.1). We plot α_d, α_c and n_d as functions of ω in Fig. 2.4(b). As a measure of trapping performance, we calculate the quality factor Q from electric and magnetic field distribution in the steady state. Q is defined by

$$Q = \omega \frac{U}{P}, \tag{2.7}$$

where P is the power dissipated and U is the energy stored in the rainbow trapping structure ($z > 0$) having the entrance thickness α_0 (see inset of Fig. 2.4(a)). Here, α_0 is chosen to be $\max\{\alpha_c(\omega)\}$ to ensure the structure to be functional for the entire target frequency range. Recognizing that the input power is equal to the dissipated power in steady state, and that the only incoming guided mode at the entrance ($z = 0$) is $|f+\rangle$, P is equal to the incoming power carried by $|f+\rangle$. Since the wave propagates deeper along the taper, Q increases as ω increases for a fixed taper angle $\theta = 2^\circ$ (Fig. 2.4(d)). It is worth noting that Q is directly proportional to the light trapping time $\tau = Q/\omega$. For instance, for $\theta = 2^\circ$ and $\omega/\omega_p = 0.6$, τ is calculated to be around 33 periods, which is quite a long time since the distance between the entrance and the degeneracy point is only about 1.5 effective wavelengths. We confirm that τ corresponds to the actual signal trapping time by measuring the time it takes by a pulse to escape a rainbow trapping structure by FDTD simulations. Interestingly, the signal trapping time does not vary significantly from the value of the lossless case but only causes the outgoing signal to attenuate as Γ becomes larger.

When material loss is present ($\Gamma \neq 0$), the degeneracy between $|f\rangle$ and $|b\rangle$ is removed and v_E thus has finite value everywhere (Fig. 2.2(f)). However, the overall power flow and optical dispersion characteristics v_E drops down significantly and that the effective indices of $|f\rangle$ and $|b\rangle$ get very close to each other around $\alpha = \alpha_d$ are preserved. Thus the previously described light trapping mechanism is still valid except at very high loss. For a fixed frequency, Q is found to be almost inversely proportional to the taper angle. As $\theta \to 0$, Q becomes limited by ohmic loss inside the metal alone, asymptotically approaching $c/2v_E\mathrm{Im}\{n_{\mathrm{eff}}^{f+}(\alpha = \alpha_0)\}$ (Fig. 2.5(b)).

We also calculate the effective area A_{eff} for our two-dimensional rainbow trapping

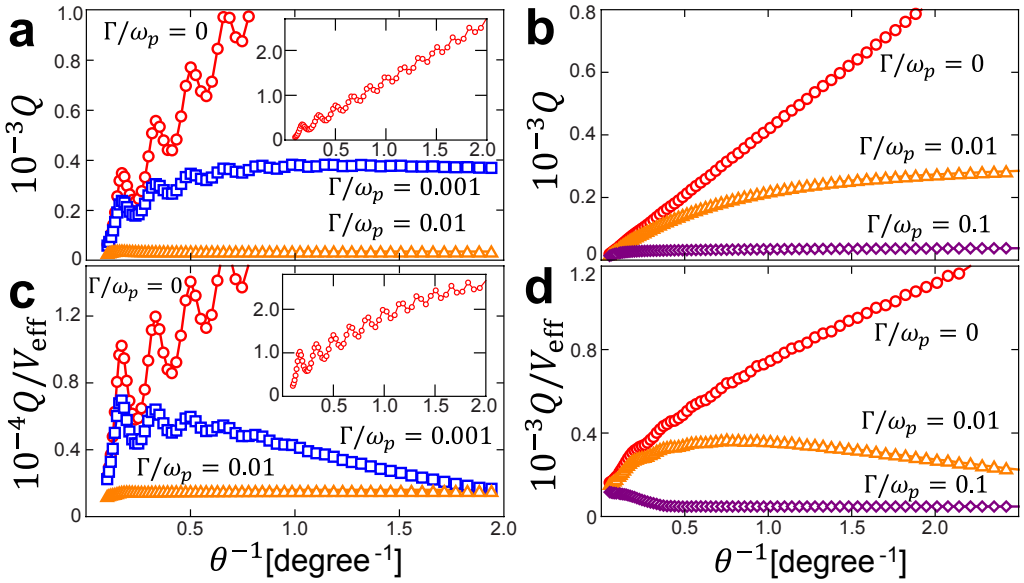

Figure 2.5: Q and Q/V_{eff} versus θ^{-1} of (a), (c) MIM ($\epsilon_{\text{I}} = 10$) TM_1 modes at $\omega/\omega_p = 0.277$ for $\Gamma/\omega_p = \{0$(red circles), 0.001(blue squares), 0.01(orange triangles)$\}$ and (b),(d) TM_2 modes at $\omega/\omega_p = 0.6$ for $\Gamma/\omega_p = \{0$(red circles), 0.01(orange triangles), 0.1(purple diamonds)$\}$. The insets in (a) and (c), respectively, plot Q and Q/V_{eff} for $\Gamma = 0$ in full range. Q/V_{eff} is normalized by $(\lambda_0/n_{\text{I}})^{-3}$.

structure as a measure of light localization, $A_{\text{eff}} = U/\max\{u(x,z)\}$, where (x,z) reside in the dielectric core where an object may be placed to interact with the eld. By conservatively assuming a diffraction-limited height $L_y = \lambda_0/2n_{\text{I}}$, the effective volume can be approximated as $V_{\text{eff}} \sim A_{\text{eff}}\lambda_0/2n_{\text{I}}$. Figure 2.5(d) displays Q/V_{eff} of TM_2 modes as a function of inverse angle θ^{-1}. When $\Gamma = 0$, Q/V_{eff} monotonically increases since adiabatic condition holds up to α closer to α_d as θ gets smaller. In the presence of material loss, the effect of rainbow trapping and propagation losses compete. The Q/V_{eff} is dominated by propagation loss for very small taper angle whereas the rainbow trapping effect dominates it for relatively large θ, because propagation loss exponentially increases as a function of propagation distance. Therefore Q/V_{eff} has a maximum where both effects are balanced. For greater values of Γ, the optimal θ increases to compensate higher propagation loss.

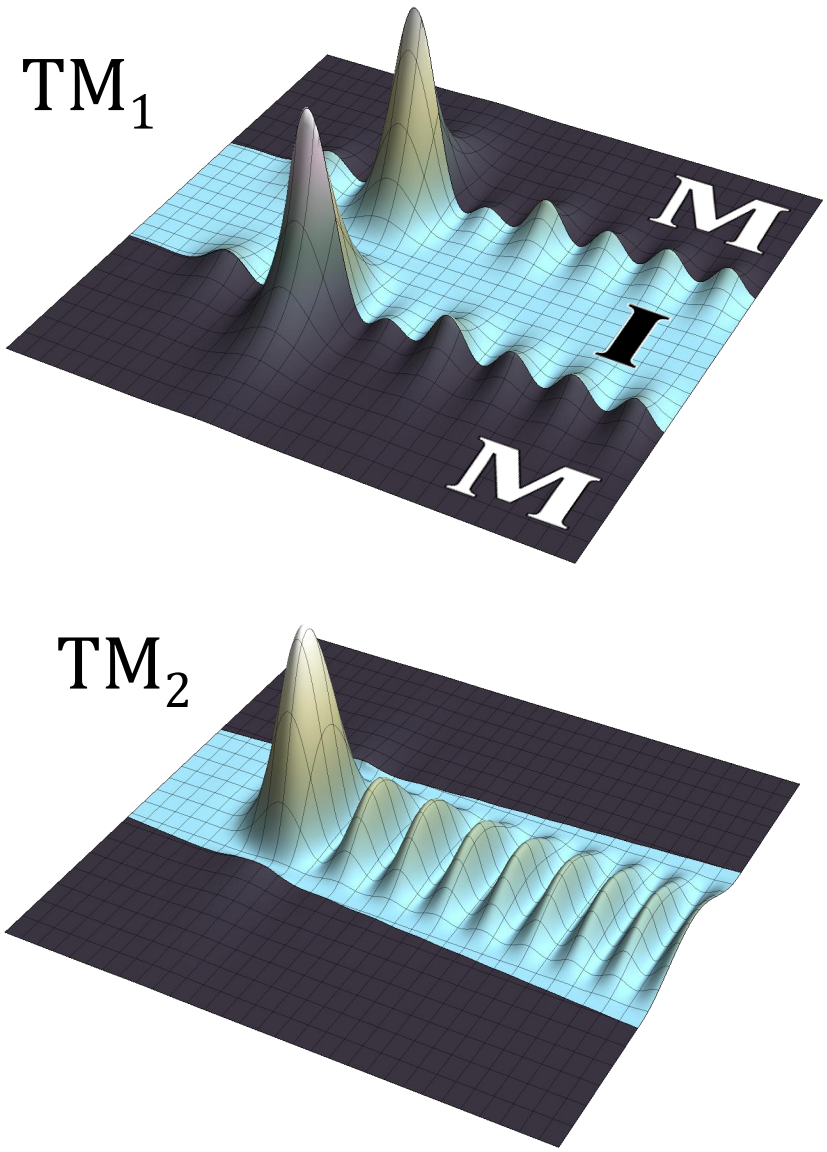

Figure 2.6: Time averaged magnetic field intensity distribution in MIM rainbow trapping structures with taper angle $\theta = 2°$, $\sigma_\epsilon = 1.2$ (TM_1, top), and $\sigma_\epsilon = 0.1$ (TM_2, bottom).

2.4.2 MIM TM_1 Mode Trapping

We note that TM_1 modes at

$$\frac{\omega}{\omega_p} \in \left((1.3510\epsilon_{\mathrm{I}}+1)^{-1/2}, (\epsilon_{\mathrm{I}}+1)^{-1/2}\right) \tag{2.8}$$

can also be trapped in the MIM taper structures. The parameters α_d and α_r of TM_1 modes have similar order of magnitude to those TM_2 modes, implying that both type of modes can be trapped in a single structure (Fig. 2.4(a)). However, unlike TM_2 or higher-order photonic modes, TM_1 modes are mostly antisymmetric superpositions of surface plasmon polariton modes. Their field intensity is greatest at the metal/dielectric interfaces and exponentially decays as a function of distance from the interface, making them slow compared to the photonic modes and very sensitive to changes at the vicinity of the surface. Because of the small energy velocity, Q of TM_1 modes tends to be much higher than that of photonic modes and even diverges when ω approaches to surface plasmon resonance frequency if the metals are lossless (Fig. 2.4(c)). Moreover, since the energy of TM_1 modes is highly confined at the interfaces, they can have very small A_{eff} well below the diffraction limit (Fig. 2.5(c)). However, because of the significant energy penetration into the metal, TM_1 modes are much sensitive to the material loss than TM_2 modes, making it difficult for them to exhibit a rainbow trapping effect for the realistic damping constant $\Gamma/\omega_p \sim 0.01$ [45]. They also undergo nonnegligible reflection due to the tapering. This adds distinctive Fabry-Perot type oscillations as a function of the taper length, as illustrated in Figs. 2.5(a) and (c). The TM_1 modes might not be suitable for signal processing since the shape of a signal can be significantly distorted by this reflection.

2.4.3 Trapped Rainbow in Real Materials

In order to exhibit rainbow trapping effect for a wide range of frequencies, dielectric core materials should have sufficiently high index and the metal cladding should have low ohmic loss and simultaneously satisfy the conditions specified in Table 2.1. In

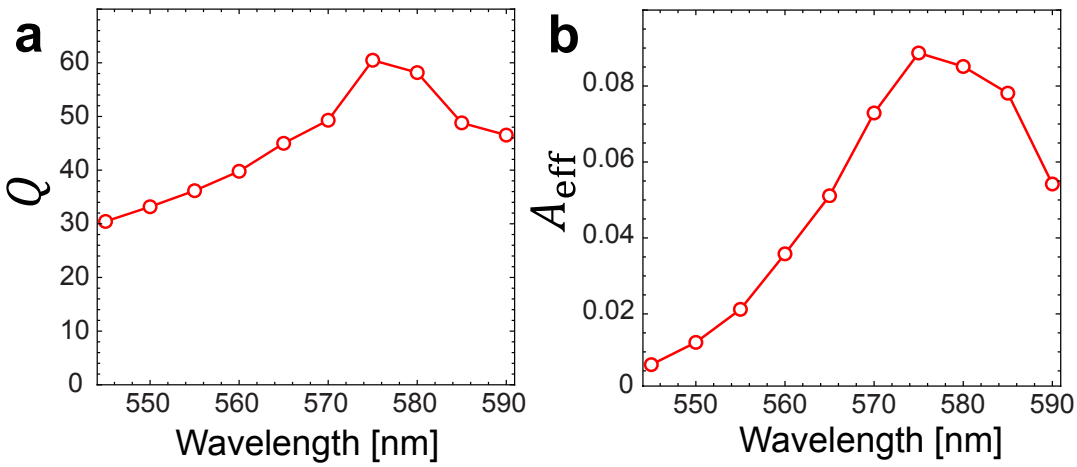

Figure 2.7: (a) Q and (b) A_{eff} of TM_1 modes in a Ag/GaP/Ag rainbow trapping structure as functions of free space wavelength. For $\alpha = 50$ nm and $\theta = 5°$, we obtain Q ∼30–60 and A_{eff} ∼0.01–0.1 throughout the target wavelength range. As the excitation wavelength approaches the surface plasmon resonance wavelength (∼540 nm), the mode becomes highly lossy and more confined near Ag/GaP interfaces. In this regime, the system is dominated by propagation loss rather than the effect of rainbow trapping. Therefore, small A_{eff} near the surface plasmon resonance wavelength is not the direct consequence of the rainbow trapping effect. A_{eff} is normalized by $(\lambda_0/n_{\text{I}})^2$.

the optical frequency range, MIM rainbow tapers with Ag [45] as the metallic layer and GaP [75] as the dielectric are able to trap TM_1 modes for wavelengths ranging from 540 to 590 nm at α of 22–48 nm. For a Ag/GaP/Ag taper of $\alpha_0 = 50$ nm and $\theta = 5°$, we obtain $Q \sim$ 30–60 and $A_{\text{eff}}(\lambda_0/n_{\text{I}})^{-2} \sim$ 0.01–0.1 throughout the target wavelength range (Fig. 2.7). One could also trap infrared light by utilizing polar dispersive materials that support phonon-polariton modes as negative permittivity claddings. For instance, SiC/Si/SiC heterostructures are able to localize TM_2 modes in infrared regime near the SiC phonon polariton resonance (∼10.5 μm) where the permittivity of SiC varies from positive to negative with very small damping [97].

2.5 Summary and Outlook

In summary, rainbow trapping structures composed of insulating core and metal claddings offer better trapping performance compared to INI or IMI structures. We have also shown that MIM rainbow trapping structures can exhibit large broadband

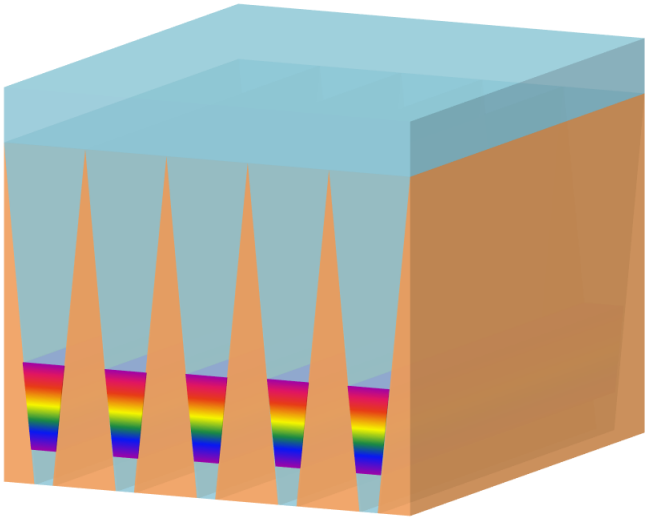

Figure 2.8: Schematic of an arrayed rainbow trapping structure for photovoltaic applications. The structure traps different frequency bands of the solar spectrum into semiconductors of different band gaps arrayed along the taper in order to maximize the solar absorption.

Q and Q/V_{eff} comparable to those of existing plasmonic cavities [69, 71]. It should also be possible to reduce the propagation loss by configuring the taper profile of rainbow trapping structures to be other than linear. Rainbow trapping structures may also find application as materials that surpass the classical light trapping limit [107] and which enhance the efficiency of solar cells by trapping different frequency bands of the solar spectrum into semiconductors of different band gaps arrayed along the taper in order to maximize the solar absorption (Fig. 2.8). Further investigations may also lead to applications in optical signal processing by utilizing the electro-optic effect.

Chapter 3

Electron Optics in Graphene

We develop a finite difference time domain (FDTD) method for simulating the dynamics of graphene electrons, denoted GraFDTD. We then use GraFDTD to study the temporal behavior of a single localized electron wavepacket, showing that it exhibits optical-like dynamics including the Goos-Hänchen effect [37] at a heterojunction and the Rainbow trapping effect [98] in a tapered electron waveguide, but the behavior is quantitatively different than for electromagnetic waves. This suggests issues that must be addressed in designing graphene-based electronic devices analogous to optical devices. GraFDTD should be useful for studying such complex time-dependent behavior of quasi-particle in graphene.[1]

3.1 Introduction

The graphene two-dimensional (2D) carbon material has two π electrons and two atoms per unit cell, resulting a semimetallic electronic band with a conical intersection at the Fermi energy (the K point of the Brillouin Zone). Thus charge carriers near the Fermi energy behave like 2D massless relativistic particles exhibiting a linear (photonlike) dispersion relation, which is effectively described by the Dirac equation with Fermi velocity $v_F \approx 10^6$ m/s [13]

$$\left[-i\hbar v_F \boldsymbol{\sigma} \cdot \vec{\nabla} + U\right] \Psi = i\hbar \frac{\partial \Psi}{\partial t}, \tag{3.1}$$

[1] This chapter is a slightly modified version of Refs. [42, 50].

where U is the external electric potential, and $\boldsymbol{\sigma} = (\sigma_x, \sigma_y)$ are the Pauli matrices.

This enables an analogy between the quantum wave nature of graphene electronics and the electromagnetic (EM) waves in dielectrics described by Maxwell equations within the electron mean free path scale. For example, graphene electrons can exhibit electronic left-handed materials [15], quantum Goos-Hänchen (GH) shift [7, 113], Bragg reflectors [35], and wave guides [114]. All previous theoretical studies of these properties for graphene were carried out analytically, limiting the analysis to stationary solutions such as finding confined modes [81, 114] or describing plane waves [7, 15, 35, 47, 113]. Such descriptions do not provide an understanding of the dynamics of *localized electron wavepackets*, which can be essential in tracing the position of the electron.

This chapter addresses the following questions: (1) Do the optical-like behavior formulated in the wave-like point of view of the graphene electron remains valid when one includes the particle-like character of spatially localized electron wave packets? (2) Can the graphene electron's exotic tunneling behavior (Klein tunneling) or the GH shift be observed in the time-resolved dynamics? In order to clarify such questions, we developed the "GraFDTD" method to calculate numerically the time evolution of the de Broglie wave for the excited graphene electrons. In this chapter, we use GraFDTD to investigate the scattering behavior of an electron wavepacket at a heterojunction boundary. Then we study the rainbow trapping effect in a tapered electron waveguide, which is made of symmetric quantum well with varying width. We also compare our results with the dynamics of EM waves in the corresponding optical systems.

3.2 Real-Time Numerical Simulation of Graphene Electrons: GraFDTD

3.2.1 Finite-Difference Time Domain Method

The electronic wavefunction in graphene is described by a two-component isospinor $\Psi = (\psi_1, \psi_2)$ resulting from having two atoms per unit cell. To describe the time

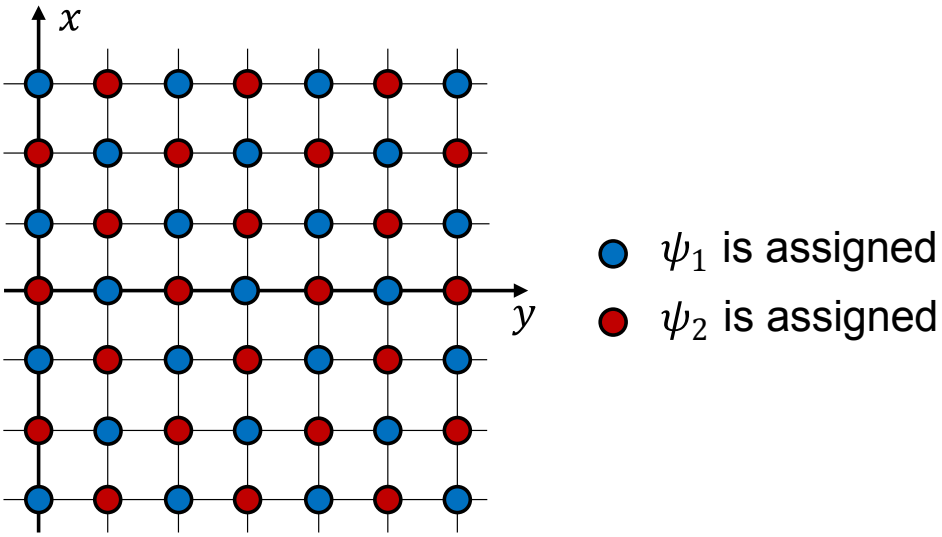

Figure 3.1: Schematic of GraFDTD space discretization. Graphene is represented as a $(M \times N)$ rectangular grid with the pseudospin components of ψ_1 and ψ_2 alternatively assigned on the grid points due to the symmetric shape of the update scheme. The external potential $U(x, y)$ is applied on each grid point. An electron wavepacket is excited from the $y = 0$ boundary, and then propagates along $+y$ direction.

evolution of Eq. (3.1), we discretize the time domain using the velocity Verlet algorithm, which has the virtue that it is a second order simplectic integrator allowing us to sample both ψ_1 and ψ_2 simultaneously. The update of $\Psi = (\psi_1, \psi_2)$ during the time step Δt is carried out via the following three steps:

1. Update of $\psi_1(t + \Delta t/2)$ from $\psi_1(t)$ and $\psi_2(t)$,

$$\psi_1\left(t + \frac{\Delta t}{2}\right) = \left(1 - i\frac{U\Delta t}{2\hbar}\right)\psi_1(t) - \frac{v_F \Delta t}{2}(\partial_x - i\partial_y)\psi_2(t)\,. \tag{3.2}$$

2. Update of $\psi_2(t + \Delta t)$ from $\psi_1(t + \Delta t/2)$ and $\psi_2(t)$,

$$\psi_2(t + \Delta t) = \frac{1 - iU\Delta t/2\hbar}{1 + iU\Delta t/2\hbar}\psi_2(t) - \frac{v_F \Delta t}{1 + iU\Delta t/2\hbar}(\partial_x + i\partial_y)\psi_1\left(t + \frac{\Delta t}{2}\right). \tag{3.3}$$

3. Update of $\psi_1(t + \Delta t)$ from $\psi_1(t + \Delta t/2)$ and $\psi_2(t + \Delta t)$,

$$\psi_1(t + \Delta t) = \frac{1}{1 + iU\Delta t/2\hbar}\psi_1\left(t + \frac{\Delta t}{2}\right) - \frac{v_F \Delta t/2}{1 + iU\Delta t/2\hbar}(\partial_x - i\partial_y)\psi_2(t + \Delta t)\,. \tag{3.4}$$

To treat the spatial derivatives of ψ_1 and ψ_2 numerically, we discretize the two-dimensional space with Δx and Δy, yielding a $(M \times N)$ rectangular grid. Using finite difference method, ∂_x and ∂_y are simply given by

$$\partial_x \psi_a\,(m,n) = \frac{\psi_a\,(m+1,n) - \psi_a\,(m-1,n)}{2\Delta x}, \tag{3.5}$$

$$\partial_y \psi_a\,(m,n) = \frac{\psi_a(m,n+1) - \psi_a(m,n-1)}{2\Delta y}, \tag{3.6}$$

where $a \in \{1,2\}$, and m and n are integer values satisfying $1 \leq m \leq M$ and $1 \leq n \leq N$. $\psi_a(m,n)$ denotes the value of ψ_a at the spatial grid point of (m,n).

In the implementation of the update scheme, the spatial derivatives of ψ_1 is involved in the update of ψ_2 and that of ψ_2 is involved in the update of ψ_1. Hence, by assigning ψ_1 and ψ_2 on the spatial grid as a checker board pattern as depicted in Fig. 3.1, we reduce the computational cost by factor of 2. In addition to that, this "staggered fermion" formalism resolves the issue of "fermion doubling" by effectively increasing the size of the unit cell in real space [53].

This simulation scheme which updates two pseudospin components alternately resembles the finite-difference time-domain (FDTD) simulation method for EM wave modeling [111], which updates electric field and magnetic field alternately.

Here, we consider a square shaped graphene and choose ordinary Cartesian coordinates with the x and y axes parallel to the sides of the graphene sheet as depicted in Figs. 3.1 and 3.2.

3.2.2 Excitation of an Electronic Gaussian Wavepacket

The localized Gaussian wavepacket is generated at $y = 0$ boundary as

$$\Psi(x;t)|_{y=0} = N \begin{pmatrix} 1 \\ i \end{pmatrix} \exp\left(-\frac{x^2}{4\sigma_x^2} - \frac{t^2}{4\sigma_t^2} - i\frac{E_F}{h}t \right), \tag{3.7}$$

where N is the normalization constant, $\sigma_x = 50$ nm and $\sigma_t = 50$ fs. This excitation process leads an isotropic Gaussian wavepacket of 50 nm size.

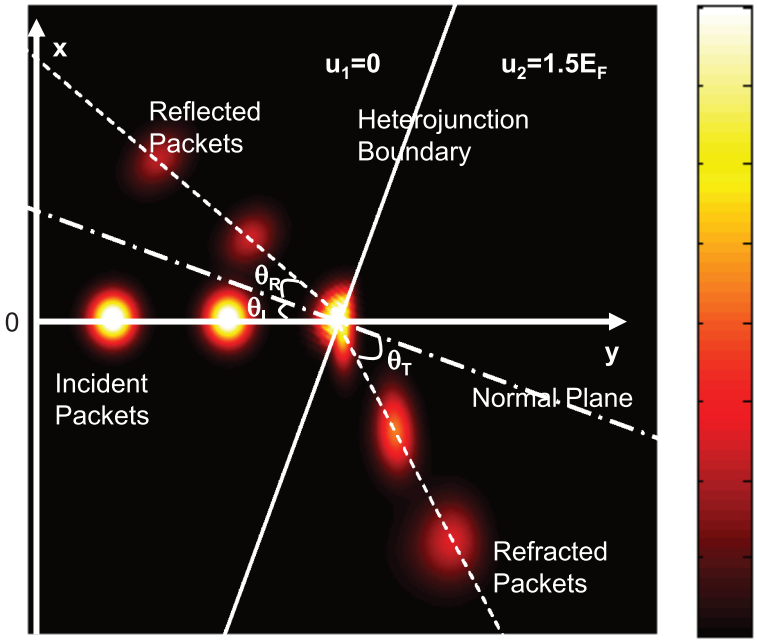

Figure 3.2: Dynamics of a Gaussian electron wavepacket at a heterojunction interface. Snapshots are taken at every 400 fs and displayed simultaneously. Wavepacket is colored by the probability density. The incident packet is introduced along the y-axis. Physical parameters are chosen to be $\theta_I = 20°$ and $(n_1, n_2) = (1, -0.5)$.

3.3 Photonlike Behavior of Graphene Electron at a Heterojunction Interface

Experimentally, a heterojunction of graphene can be achieved by electrostatic gating or by doping molecules area-selectively on the graphene [18]. Either of them can be modeled by an application of electric potential U. When a de Broglie wave of an electron approaches the heterojunction interface, the electron wave is split into two parts, one transmitted and one reflected similar to the behavior of electromagnetic wave at the interface of two different media. In this section, we discuss how those reflected and transmitted graphene electronic waves behave similarly to/different from the electromagnetic waves.

We set an external electric potential U depending on the incident angle θ_I as u_1 where $y < x \tan\theta_I$ and u_2 where $y \geq x \tan\theta_I$. We use four potential profiles $(u_1, u_2) = (0, 0.5E_F)$, $(0, 1.5E_F)$, $(0.5E_F, 0)$, and $(1.5E_F, 0)$. The Fermi energy is

chosen to be $E_F = 0.276$eV which leads to $\lambda = hv_F/E_F$ =15 nm for the de Broglie wavelength.

The localized electron (described as a Gaussian wavepacket of 50 nm size) is generated at $y = 0$ boundary in Section 3.2.2. Since the linear dispersion relation is valid within the ballistic transport regime, spatial localization within the mean free path is a more reasonable model of the graphene electron rather than a plane wave description. Experimentally, the graphene system is known to have a mean free path of several 100nm [9, 26], much larger than the lattice constant of 0.247nm. Thus, we consider that a spatial localization of 50nm provides a reasonable description of the graphene electrons.

3.3.1 Snell's Law

Consider a plane wave of an electron of Fermi energy E_F hitting an electric potential wall of height U with an incident angle θ_I. The momentum conservation along the interface, in addition to the linear dispersion relation $E = v_F\hbar k$, determines Snell's law:

$$\frac{\sin\theta_I}{\sin\theta_T} = \frac{E_F - U}{E_F}, \tag{3.8}$$

where θ_T is the angle of refraction. Therefore, the effective refractive index for graphene electrons in the gated region relative to the ungated region can be defined as the ratio of Fermi energies [15],

$$n = \frac{E_F - U}{E_F} = 1 - \frac{U}{E_F}. \tag{3.9}$$

This is numerically confirmed from the time-dependent Gaussian wavepacket dynamics using GraFDTD. When the Gaussian wavepacket is introduced to the heterojunction interface with the incident angle of (θ_I), it is split into two parts; transmitted one and reflected one as shown in Fig. 3.2. The angle of reflection θ_R and refraction

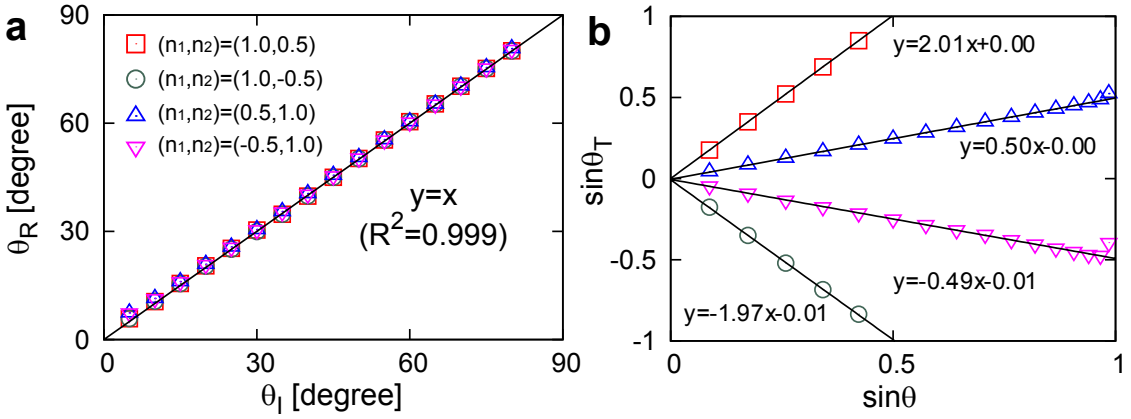

Figure 3.3: Demonstration that the Gaussian electron wavepacket obeys the law of reflection and the Snell's law [42]. (a) Plot of θ_R versus θ_I for $(n_1, n_2) = (1, 0.5)$ (red squares), $(1, -0.5)$ (green circles), $(0.5, 1)$ (blue triangles), and $(-0.5, 1)$ magenta reverse-triangles). These are aligned on top of $y = x$ line (R^2 =0.999), indicating $\theta_I = \theta_R$. (b) Plot of $\sin\theta_T$ versus $\sin\theta_I$ for four different cases, each of which shows a linear fit. The slope of each line is determined by n_1/n_2 which is 2, -2, 0.5, and -0.5 respectively. This is in excellent agreement with the slopes determined from numerical simulations: 2.01, -1.97, 0.50, and -0.49.

θ_T obtained by numerically tracking the position of wavepacket,

$$\langle x \rangle = \int \Psi^\dagger x \Psi dx dy, \tag{3.10}$$

are shown in Fig. 3.3. Clearly, all data points of θ_R as a function of θ_I (Fig. 3.3(a)) lie on the lines of $y = x$, indicating that the law of reflection remains valid in the graphene electron system. From Fig. 3.3(b), one can find that the $\sin\theta_T$ linearly depends on $\sin\theta_I$, and the slope is determined as n_1/n_2.

When $\mathrm{sign}(n_1/n_2) < 0$, the graphene electron is refracted in the reverse sense to that normally expected (negative refraction). To realize such an effect in optical systems, one needs to fabricate a metamaterial which is an artificial material designed to achieve a negative value for both electric permittivity ϵ and magnetic permeability μ.

Although metamaterial system has a wide applicability such as cloaking devices [86], superlenses [80], and metamaterial antennas [28] due to its exotic physics, the actual fabrication of wide-bandwidth metamaterial is still demanding. Using a graphene

electronic system, however, one can easily achieve an analogue simply by applying a local gate voltage.

3.3.2 Klein Tunneling

From his gedanken experiment, Klein obtained a counterintuitive result referred as a "Klein paradox"—perfect tunneling of one-dimensional massless Dirac particle through a step potential regardless of the potential height. No experimental test on such a quantum electrodynamic phenomenon had been available using any elementary particle since it is impossible to generate a potential drop within a short range ($\sim$Compton length scale) which yields an enormous electric fields ($> 10^{16}\mathrm{Vcm}^{-1}$). Using a graphene electron, which is a two-dimensional Dirac-like quasiparticle, however, people were able to confirm the Klein tunneling to the electrostatic barrier experimentally [91, 112].

At a heterojunction, we calculate the probability of transmission T_{GE} by integrating the probability density over the region $y \geq x \tan\theta_I$. On the other hand, analytical solutions of T_{GE} for a electronic plane waves can be expressed in terms of θ_I and θ_T [14, 47],

$$T_{GE}(\theta_I) = \frac{\cos\theta_I \cos\theta_T}{\cos^2\left[(\theta_I + \theta_T)/2\right]}. \tag{3.11}$$

In the case of normal incidence ($\theta_I = 90°$), T_{GE} approaches unity regardless of the potential height, which refers the Klein tunneling. The numerical results from GraFDTD exhibit a perfect agreement with Eq. (3.11) as demonstrated in Fig. 3.4 for various potential heights. When $\theta_I \geq \theta_c = \sin^{-1}(n_2/n_1)$, graphene electron is totally internally reflected at the heterojunction boundary.

When the impedances of two optical media are matched, the transmittance of electromagnetic wave, T_{EM}, becomes identity for normal incidence similar to the Klein tunneling of graphene electrons. Therefore, this impedance matched interface can be regarded as an optical counterpart for the heterojunction of the graphene system. For an impedance matched interface, the transmittances of the transverse electric (TE) and transverse magnetic (TM) wave become identical to each other,

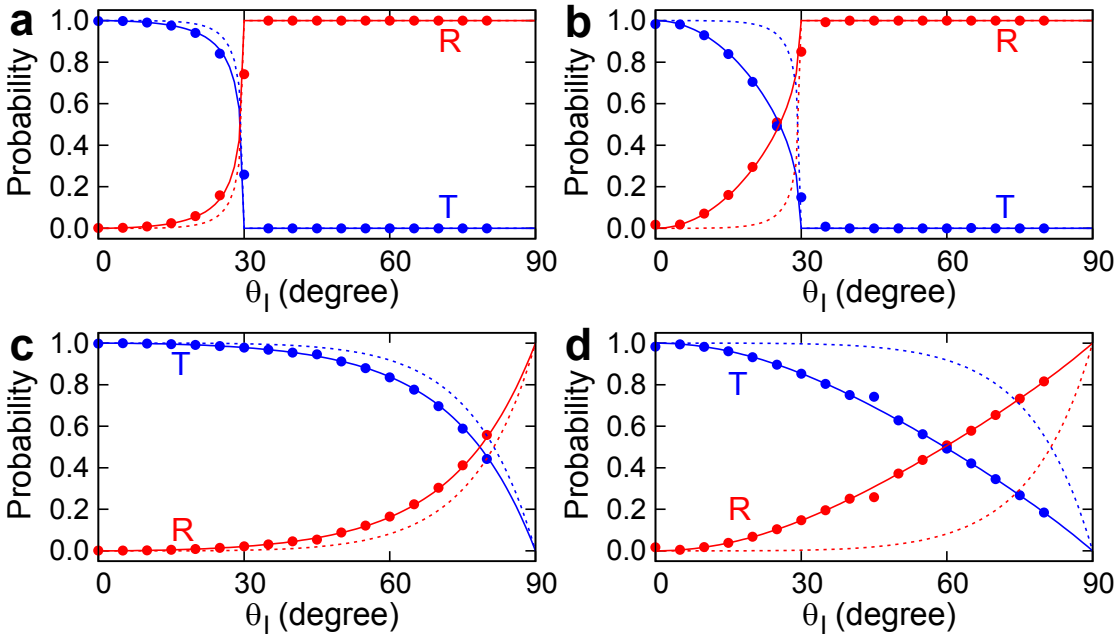

Figure 3.4: Transmittance (T; blue) and reflectance (R; red) versus incidence angle θ_I for (a) $(n_1, n_2) = (1, 0.5)$, (b) $(1, -0.5)$, (c) $(0.5, 1)$, and (d) $(-0.5, 1)$. Simulation results for T_{GE} and R_{GE} (circles) agree with the analytic results (solid lines) and are compared with the T_{EM} and R_{EM} for EM waves (dotted lines).

which is expressed as [11]

$$T_{EM}(\theta_I) = \frac{\cos\theta_I \cos\theta_T}{\left[(\cos\theta_I + \cos\theta_T)/2\right]^2}. \tag{3.12}$$

Interestingly, T_{GE} and T_{EM} have similar mathematical forms, which are graphically compared in Fig. 3.4.

A square potential barrier with a finite width is also an interesting system since it resembles the bar shaped gate potential in typical graphene field effect transistors. Transmission probability through the square barrier of height U and width D can be obtained by matching the boundary condition of the wavefunction [47]:

$$T_{GE}(\theta_I) = \frac{\cos^2\theta_I \cos^2\theta_T}{\left[\cos(Dq_x)\cos\theta_I\cos\theta_T\right]^2 + \sin^2(Dq_x)\left[1 - ss'\sin\theta_I\sin\theta_T\right]^2}, \tag{3.13}$$

with $s = \mathrm{sign}(E_F)$, $s' = \mathrm{sign}(E_F - U)$, and $\theta_T = \tanh(k_y/q_x)$ where $k_y = k_F \sin\theta_I$

and

$$q_x = \sqrt{\frac{(U - E_F)^2}{v_F^2} - k_y^2}. \tag{3.14}$$

Note that Eq. (3.13) becomes unity when $\theta_I = 0$. This indicates that the bar shaped gate potential is almost transparent for the electrons hitting the gate potential with small angle of incidence θ_I. This leads a substantial off-current of graphene based field-effect transistors (FET) fabricated with bar shaped gate electrodes [58, 67], which is a major problem for the device applications of graphene.

3.3.3 Quantum Goos-Hänchen Effect

When a linearly polarized light beam is totally internally reflected, it undergoes a lateral shift along the boundary of two optical media, which is called as a Goos-Hänchen (GH) effect [37]. It is interpreted in terms of a horizontal energy flow of an evanescent wave in the medium having a lower index of refraction during the total internal reflection. When both media have positive refractive indices, GH shift is along the forward direction. On the contrary, at the boundary between right and left handed media, GH shift is along the backward direction. The optical GH shift distance d_EM at the impedance matched interface is given by [8]

$$d_{EM}(\theta_I) = \frac{\lambda}{\pi} \frac{n \cos\theta_I}{(1 - n^2) \sin\theta_I \sqrt{\sin^2\theta_I - n^2}}, \tag{3.15}$$

with $n = n_2/n_1$ when the EM wave propagates from medium 1 to medium 2. The electronic analogue of the GH effect has been proposed by Beenakker et al., [7] including relativistic corrections in the limit of massless electrons relevant for graphene (i.e., quantum version of GH effect). When one considers an incident beam of graphene electron on the heterojunction with $\theta_I \geq \theta_c$, it undergoes a total internal reflection (see Section 3.3.2) and the position of the reflected beam is shifted depending on the pseudospin (sublattice) degree of freedom. The total GH shift distance of graphene

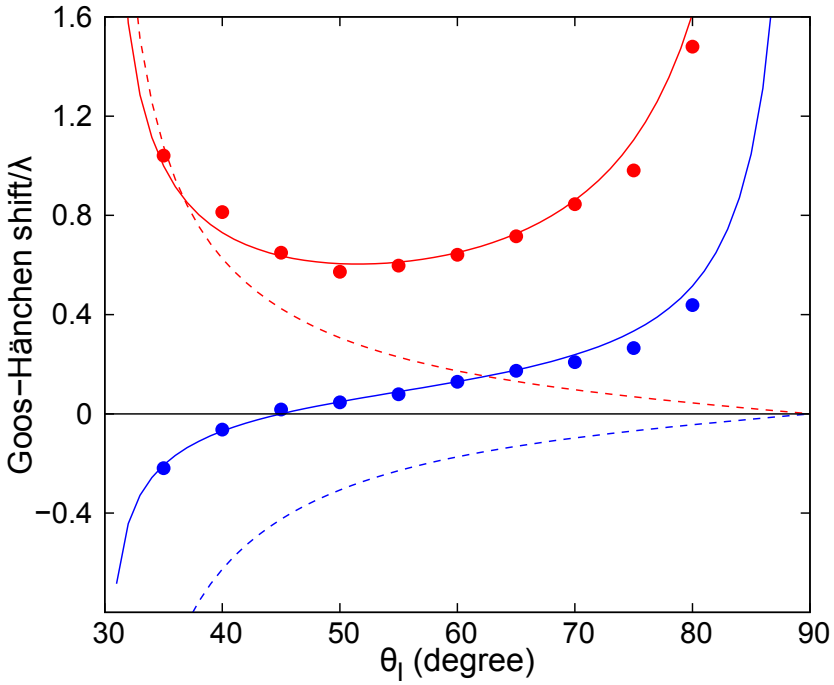

Figure 3.5: Goos-Hänchen shift versus the incidence angle θ_I for $(n_1, n_2) = (1, 0.5)$ (red) and $(1, -0.5)$ (blue). Simulation results for d_{GE} (circles) agree with the previous analytical results (solid lines) and are compared with the GH effect for EM waves d_{EM} (dotted lines).

electron d_GE is

$$d_{GE}(\theta_I) = \frac{\lambda_F}{2\pi} \frac{\sin^2\theta_I + n}{\sin\theta_I \cos\theta_I \sqrt{\sin^2\theta_I - n^2}}, \tag{3.16}$$

When the signs of the effective refractive indices at both sides are same (n-n or p-p junction), d_GE is positive analogous to the positive GH shift d_EM at an interface between materials having the same sign of refractive index. At a p-n junction, graphene electron experiences either a positive GH shift or a negative GH shift depending on the angle of incidence; $d_GE \leq 0$ when $\theta_I \leq \theta^* = \sin^{-1}\sqrt{\sin\theta_c}$, and $d_GE > 0$ when $\theta_I > \theta^*$.

From the wavepacket dynamics using GraFDTD, one can measure the actual amount of shift by tracking the center of the wavepacket. Equation (3.16) is numerically confirmed in Fig. 3.5, demonstrating a perfect agreement to each other including the sign change behavior around θ^* (which is 45° for this case).

Fig. 3.5 compares d_{GE} with d_{EM}, the optical GH shift at impedance matched interfaces, showing that the limiting behavior at $\theta_I \to \theta_c$ is analogous for both optical and graphene systems. However, the limiting behavior at $\theta_I \to 90°$ is totally different since d_{EM} is suppressed while d_{GE} diverges to infinity. Additionally, the optical system does not exhibit the sign change behavior. These differences lead to a more restricted incident angle window for the graphene system to exhibit the negative GH effect compared to the optical systems.

3.4 Electron Rainbow Trapping in Graphene

3.4.1 Graphene Electron Waveguide

A dielectric slab waveguide which consists of three dielectric layers with different refractive indices is one of the simplest geometries of optical waveguides. Light is confined in the middle layer by total internal reflection under the condition that the refractive index of the layer is higher than those of the surrounding layers.

Recently, researchers have investigated the guided eigenmodes in graphene quantum well as an electronic analogue of optical slab waveguide [114]. Let us consider a symmetric quantum well waveguide structure of the electron potential profile

$$U(x) = \begin{cases} 0 & |x| \leq \alpha, \\ U & |x| > \alpha. \end{cases} \tag{3.17}$$

The condition for having guided modes, which is equivalent to the condition for total internal reflection at the boundary between the core and the cladding, is defined by Snell's law, $|n| = |1 - U/E_F| < 1$, i.e., $0 < U < 2E_F$, where n is the refractive index for graphene electrons in the claddings relative to the core. Solving Dirac equation by applying the continuity of the wavefunction, we obtain the dispersion relation of the guided modes as follows.

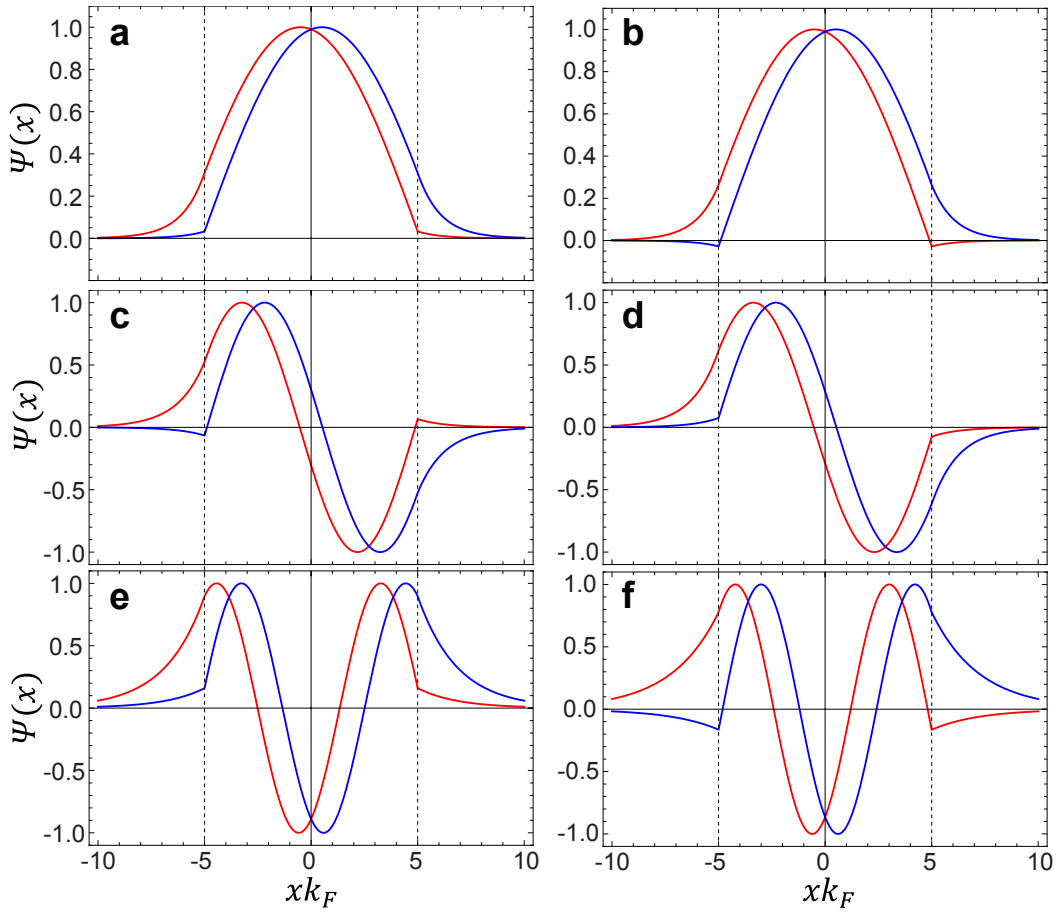

Figure 3.6: The wave function of the guided modes in (a), (c), (e) n-n-n ($U/E_F = 0.8 \leftrightarrow n = 0.2$) and (b), (d), (f) p-n-p ($U/E_F = 1.2 \leftrightarrow n = -0.2$) electron waveguides in graphene. The transverse profiles of three lowest eigenmodes are represented. The red and blue curves respectively correspond to ψ_1 and $-i\psi_2$ where ψ_1 and ψ_2 are pseudospin components of the graphene electron wavefunction $\Psi = (\psi_1, \psi_2)$.

$$\alpha' = \frac{1}{\kappa}\left[\text{atan}\left(\frac{\gamma}{\kappa}\frac{\beta+1}{\beta+n}\right) + \frac{m\pi}{2}\right] \quad m \in \mathbb{Z}, \tag{3.18}$$

where $\alpha' = \alpha k_F$ is the normalized half-width of the core, $\beta = k_y/k_F$ is the normalized propagation constant, $\kappa = \sqrt{1-\beta^2}$, and $\gamma = \sqrt{\beta^2 - n^2}$. The corresponding wavefunction is

$$\Psi(x', y'; \alpha') = \begin{cases} \begin{bmatrix} \cos(-\kappa\alpha' + \phi + m\pi/2) \\ i\cos(-\kappa\alpha' - \phi + m\pi/2) \end{bmatrix} e^{\gamma(x'+\alpha')} e^{i\beta y'} & \text{where } x' < -\alpha', \\ \begin{bmatrix} \cos(\kappa x' + \phi + m\pi/2) \\ i\cos(\kappa x' - \phi + m\pi/2) \end{bmatrix} e^{\gamma(x'+\alpha')} e^{i\beta y'} & \text{where } |x'| \le \alpha', \\ \begin{bmatrix} \cos(\kappa\alpha' + \phi + m\pi/2) \\ i\cos(\kappa\alpha' - \phi + m\pi/2) \end{bmatrix} e^{-\gamma(x'-\alpha')} e^{i\beta y'} & \text{where } x' > \alpha', \end{cases} \tag{3.19}$$

where $\phi = \text{atan}(\kappa/(1+\beta))$. $x' = k_F x$ and $y' = k_F y$ are the normalized coordinates. The wavefunctions of guided modes for $U < E_F$ and $U > E_F$ are depicted in Fig. 3.6. It is worth noting that each pseudospin component experiences negative quantum Goos-Hänchen shifts upon total internal reflection in the latter case (Fig. 3.6(b),(c),(d), and (f)), resulting in slow group velocity which can even vanish under certain conditions. We further note that the gate-controlled electron guiding has been experimentally achieved by using the device parameter of $d \sim$25nm [106].

3.4.2 Electron Rainbow Trapping

As a light storage device, many slow light devices have been proposed. One of them is a heterostructure of the left-handed metamaterial core inside the usual right-handed materials with a shape of a tapered waveguide [98]. The power flow of the guided wave inside the left-handed core should be opposite to that of the evanescent wave in

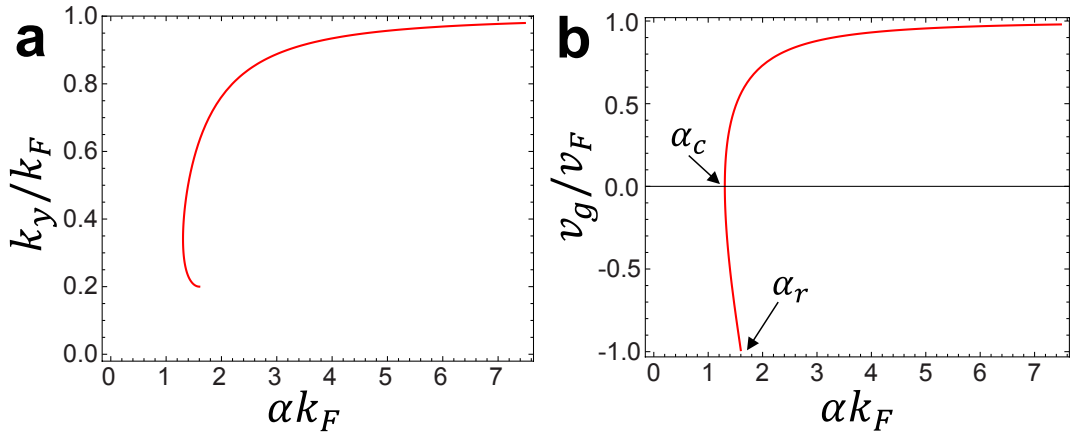

Figure 3.7: Dependence of (a) propagation constant and (b) group velocity of the fundamental eigenmode in *p*-*n*-*p* graphene electron waveguide on the core thickness α. When $\alpha \in \{\alpha_c, \alpha_r\}$, the mode consists of two branches one with positive and the other with negative v_g. Those two branches degenerate at $\alpha = \alpha_c$ where the group velocity of the modes vanishes.

the right-handed claddings. Hence, the wave can be trapped at the critical thickness where the total power flow becomes zero. Since this critical thickness varies as a function of wavelength, this stopped (or stored) light is named as a "trapped rainbow."

As an analogue, one can consider a tapered electron waveguide that can slow down the graphene electron. The guided modes in a quantum well vary as a function of the width of the well (=2α). Figure 3.7(a) shows the change of the group velocity of the guided mode (v_g) while varying α for the fundamental guide mode. Here the sign of v_g is chosen to be plus when it is parallel to the direction of the wavevector and minus when antiparallel. When $\alpha > \alpha_r$, there exists only a forward propagating mode ($v_g > 0$). When $\alpha_c < \alpha < \alpha_r$, there are both forward propagating mode ($v_g > 0$) and backward propagating mode ($v_g < 0$). Especially when $\alpha = \alpha_c$, the group velocity of the graphene electron becomes zero. This implies that the graphene electron can be trapped using a tapered waveguide if α changes adiabatically. Analytically α_c and α_r are expressed as

$$\alpha_c = \frac{\lambda_F}{2\pi} \frac{\sin^2\theta_I + n}{\sin^2\theta_I \sqrt{\sin^2\theta_I - n^2}}, \tag{3.20}$$

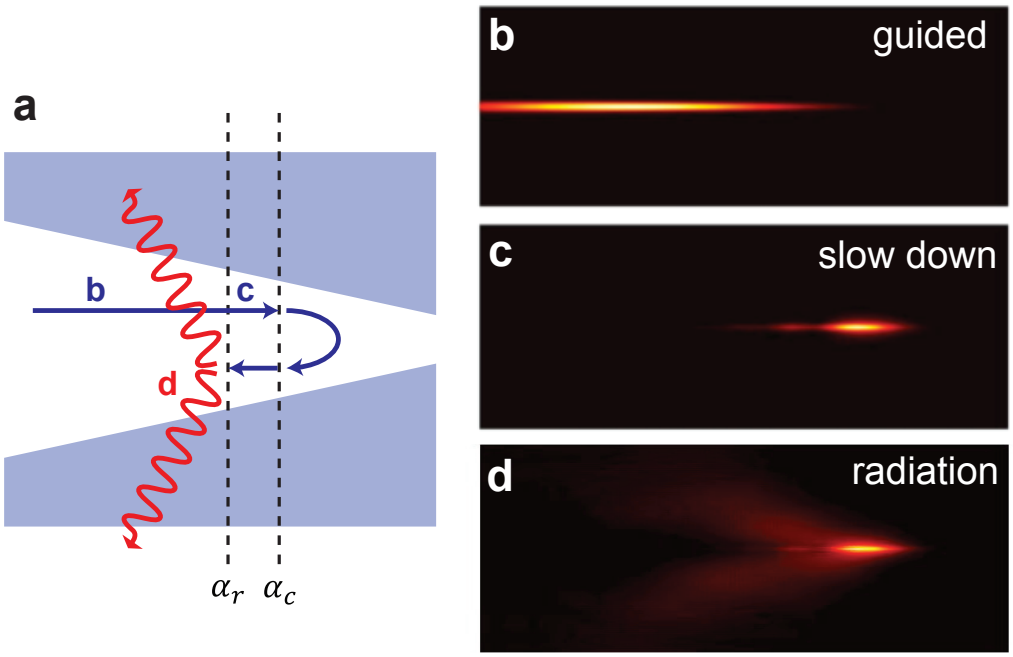

Figure 3.8: (a) Schematic description of electron trapping and releasing mechanism in tapered graphene waveguide structure. (b), (c), (d) Snapshots from trapped rainbow in graFDTD simulations. As α decreases, (c) electron wave is slowed down and becomes to be localized in a position space. When the electron reaches $\alpha = \alpha_c$, the forward propagating mode excites the backward propagating mode, then travels back. (d) When α becomes α_r (at which the backward propagating mode branch ends), guided electron wave is converted into the oscillatory radiation modes in the cladding part and escape the structure.

and

$$\alpha_r = \frac{\lambda_F}{4\sqrt{1-n^2}}, \tag{3.21}$$

with n, the refractive index of the cladding relative to the core. Interestingly, the Eq. (3.20) is related with the negative Goos-Hänchen shift Eq. (3.16) through

$$\alpha_c = d_{GE} \cot \theta_I, \tag{3.22}$$

which leads to a graphical interpretation of the path of the electron beam forming a clepsydra. This interpretation is analogous to the trapped rainbow in photonic system [98].

However there is no practical manner to have an adiabatically changing α. To investigate how the lack of adiabatic approximation affects on the dynamics of guided graphene electrons, we performed GraFDTD simulation. We consider a tapered waveguide of α changing from $6.377k_F^{-1}$ to $1.377k_F^{-1}$ with a slope of 1/100 as shown in Fig. 3.8. We applied $U = 1.2E_F$ of electric potential. Then, the analytic solution of fundamental guided mode at the wider entrance, $\Psi(x', y'; \alpha' = 6.377)$ is excited, and it travels along the forward direction (Fig. 3.8(b)). As α decreases, the electron wave is slowed down and becomes to be localized in a position space (Fig. 3.8(c)). When the electron reaches α_c, the forward propagating mode excites the backward propagating mode, then travels back a bit. When α becomes α_r (at which the backward propagating mode branch ends), guided electron wave is converted into the oscillatory radiation modes in the cladding part and escape the structure (Fig. 3.8(d)). This mechanism is schematically summarized in Fig. 3.8(a).

We numerically demonstrated that the tapered quantum well waveguide can slow down electrons, but the trapping performance is limited due to the inevitable non-adabaticity. Optimizing the curvature of the quantum well taper may increase the trapping time, and thus lead new applications in quantum information processing using electrons.

3.5 Summary and Outlook

Summarizing, we developed the GraFDTD method and used it to study the dynamics of low energy excited graphene electrons. These numerical simulations lead the demonstrations of Snell's law, negative refraction, Klein tunneling, quantum Goos-Hänchen effect, and rainbow trapping effect for graphene electrons using temporally and spatially resolved electron wave packets. These results extend the previous plane wave based analytical findings focused on the wave-like character of the graphene electron to the temporal behavior of the electron possessing the particle-like character. Additionally, we thoroughly discuss the similarities and differences of the graphene electron dynamics with their optical counterparts. Each of these is a key issue for

graphene based device applications based on the optical analogy framework [15, 113]. We can now use this validated GraFDTD for investigation of graphene electron dynamics under nontrivial chemical potential geometries, which is the topic of the next chapter.

Chapter 4

Dispersion Engineering in Graphene: Graphene Field Effect Transistor without Energy Gap

Graphene is a room temperature ballistic electron conductor [9, 26, 66, 73] and also a very good thermal conductor [5]. Thus it has been regarded as an ideal material for post-silicon electronic applications. A major complication is that the relativistic massless electrons in pristine graphene exhibit unimpeded Klein tunneling penetration through gate potential barriers [87]. Thus previous efforts to realize a field-effect transistor for logic applications [3], have assumed that introduction of a band gap in graphene is a prerequisite [6, 16, 27, 39, 67, 62, 94, 95]. Unfortunately extrinsic treatments designed to open a band gap seriously degrade device quality, yielding very low mobility and uncontrolled on/off current ratios. To solve this dilemma, we propose a gating mechanism that leads to a hundred-fold enhancement in on/off transmittance ratio for normally incident electrons without any band gap engineering. Thus our saw-shaped geometry gate potential (in place of the conventional bar-shaped geometry) leads to switching to an off-state while retaining the ultrahigh electron mobility in the on-state. Our switching mechanism demonstrates that intrinsic graphene can be used in designing logic devices without serious alteration of the conventional field-effect transistor architecture. This suggests a new variable for the optimization of the graphene-based device: geometry of the gate electrode.

4.1 Introduction

Due to the semi-metallic electronic band with a conical intersection at the Fermi energy in graphene, low energy charge carriers behave like 2-dimensional massless relativistic particles, which is effectively described by the Dirac equation with Fermi velocity $v_F \sim 10^6$m/s [13]. This linear dispersion relation enables electrons to pass through a potential with a high transmittance (100% for normal incidence) via Klein tunneling without backscattering [91, 112]. Thus, conventional bar type gate electrodes that provide a step barrier potential cannot backscatter normally incident carriers, which leads to a substantial off current [47]. This has led a poor on/off current ratio of $I_{\text{on}}/I_{\text{off}} \sim 7$ for fabricated graphene transistors [67].

To improve gate modulation, several schemes have been proposed to open a band gap in graphene. For example the spatial confinement in graphene nanoribbons [39, 94, 95, 16], leads to substantial bandgaps depending on their width. However this results in significant reduction in carrier mobility in addition to fabrication challenges due to the sensitivity of the band gap on the width and edge states [62]. An alternative is to chemically modify graphene, e.g., with patterned hydrogenation [6]. This transforms sp^2 carbons of graphene into sp^3 carbons, breaking the long-range π-π overlap and opening a bandgap. However, these sp^3 carbons provide many scattering centres for conduction electrons, leading to substantial mobility degradation [27]. Switching schemes using a magnetic barrier [22] or nanomesh structure [4] have also been suggested, but it has not been possible to achieve satisfactory fabrication of field-effect transistors while preserving the superior carrier mobility of pristine graphene. Therefore, we need a new mechanism to enhance the electron backscattering without damaging the intrinsic properties of graphene.

Here we show how to design a specific gate electric potential to induce efficient electron backscattering through use of the optical-like character of graphene electron without introducing an external band gap engineering (which would degrade on-current). We show that this can be accomplished using the saw-shaped gate electrode shown in Fig. 4.1(a) instead of a conventional bar-shaped gate electrode. Geomet-

rically, the gate potential profile $U(x, y)$ can be decomposed into a saw-tooth part at the bottom and a bar-shaped blade back part connecting teeth to form a single piece of electrode (Fig. 4.1(b)). Due to the symmetry in the graphene band, the hole dynamics of p-type channel can be also modulated using exactly identical physics on the electron dynamics as for the n-type channel discussed hereafter.

4.2 Method

4.2.1 GraFDTD Simulations

To solve the time-dependent Dirac equation (Eq. 3.1), on a two dimensional spatial grid, we discretize the time-domain using the velocity Verlet algorithm while the spatial derivatives are treated by using finite difference methods. The details of our simulation method were fully described in Section 3.2.

4.2.2 Boundary Conditions

Since the potential profile has translation invariance along the x-direction with the periodicity of W, the wave function will have the form of a Bloch wave,

$$\Psi(x + W) = e^{iWk_F \sin\theta}\Psi(x), \tag{4.1}$$

where θ is the angle of incidence. Therefore, we impose a Bloch boundary condition on the left ($x = 0$) and the right ($x = W$) boundaries of our simulation cell, such as $\Psi_R = \exp\left(iWk_F \sin\theta\right)\Psi_L$.

An electron wave function is excited from the bottom boundary by the second order approximation of

$$\Psi(x, t) = A\int_{\infty}^{\infty} dq \exp\left[\frac{\Delta_y(q - k_y)^2}{2} + i\left(k_x x - i\omega(q)t\right)\right]\begin{pmatrix} 1 \\ ie^{-i\alpha(q)} \end{pmatrix}, \tag{4.2}$$

where $\mathbf{k} = (k_x, k_y) = k_F(\sin\theta, \cos\theta)$, $\omega(q) = v_F\sqrt{k_x^2 + q^2}$, $\alpha(q) = \mathrm{atan}(k_x/q)$, and A

is the normalization factor. Unless otherwise specified, the width of the wave packet Δ_y is taken to be 100–120nm.

4.2.3 Transmission Probability Calculation

We determine the transmission probability $T(E)$ for an electron with energy E by integrating the probability density ($|\Psi|^2$) over the drain region ($y > L + L_{\text{bar}}$). We define the average transmittance

$$\bar{T} = \int T(E)F(E)dE, \tag{4.3}$$

where

$$F(E) = \frac{f_S(E) - f_D(E)}{\mu_S - \mu_D} \tag{4.4}$$

is the energy distribution of electrons participating in conduction [19]. $f_{S(D)}$ is the Fermi distribution function of the source (drain) reservoir. Note that, when the chemical potentials of the source and the drain are equal ($\mu_D = \mu_D = E_F$), the energy distribution reduces to

$$F(E) = -\frac{df(E)}{dE}. \tag{4.5}$$

At zero temperature, $F(E) = \delta(E - E_F)$, resulting in $\bar{T} = T(E_F)$. Unless otherwise specified, we assume zero temperature.

4.3 Electron Eigenmode Dispersion Relation

Graphene electron dynamics can be described in analogy to optical mode propagation [42, 77, 103]. The applied gate potential region is an analogue to waveguide cladding with an effective refractive index, $n_{\text{eff}} = 1 - U_0/E_F$, where U_0 is the potential height and E_F is the incident electron energy [42]. Here each valley region between sawtooth elements can be regarded as a tapered waveguide. We note that single tapered optical

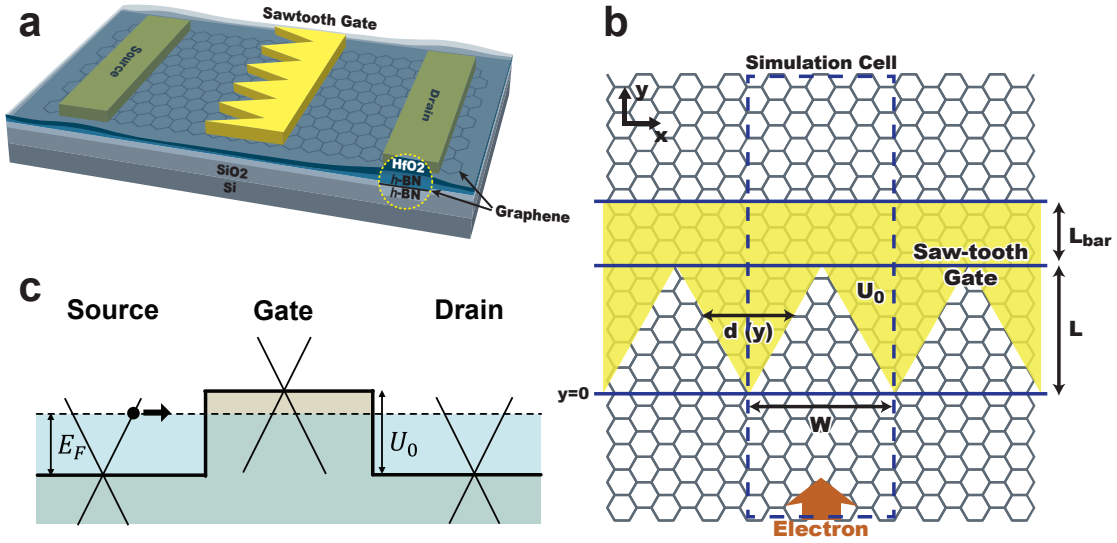

Figure 4.1: (a) Schematic of sawtooth gate electrode used to implement the backscattering mechanism based on the optical analogy for graphene electrons for the design of a graphene field effect transistor. To maintain its high mobility, the graphene is sandwiched between h-BN sheets. The source/drain electrodes are located on top of the graphene sitting on a Si/SiO2 substrate. Then, the saw-shaped top gate electrode with an insulating layer (HfO_2) is deposited. The top gate electrode is composed of sawtooth part and bar-shaped blade back part.
(b) Top view of the simulation cell where periodic (or Bloch) boundary conditions are applied along the x direction. The sawtooth gate potential (transparent yellow colored region) is characterized with a width W, the lengths of the sawtooth L, and the blade back part L_{bar}. The intervalley distance d linearly increases from 0 to W while the y coordinate changes from 0 to L. The electron wave is excited from the bottom boundary, and then travels along $+y$ direction (c) Fermi energy E_F and gate potential U_0 are illustrated with the graphene energy band diagrams.

waveguide using metamaterials has been proposed as a light capturing device which effectively reduces the group velocity of guided electromagnetic waves [43, 98].

The sawtooth part of the gate potential can also be interpreted as a Kronig-Penney type potential with a continuously varying barrier width d. To understand the electron transport through this structure, consider how eigenmodes of the Kronig-Penney potential are connected from source side ($d = 0$) to drain side ($d = W$). If an eigenstate connects smoothly across the gate potential, it serves as an electron transmitting channel; otherwise, it serves as an electron reflecting channel. In the optical analogy, these eigenmodes can be also viewed as guided modes in tapered waveguides. The longitudinal momentum eigenvalues (k_y) of these states are good quantum numbers defining the longitudinal electron propagation through the sawtooth potential, often used in optical waveguide analysis [93].

Interestingly, we found that the total number of electron transmitting channels depends strongly on U_0, and eventually drops to 1 when $U_0 \geq E_F$ regardless of the sawtooth pitch W. From detailed analysis of the variation of eigenvalues (k_y) as a function of d and U_0, we find that the connectivity of only the fundamental mode is independent of U_0 (thus always forming a transmitting channel), while that of the higher modes can be regulated by appropriate choices of U_0. For a sufficiently high gate potential of $U_0 \geq E_F$ all transmitting channels except the fundamental mode are eventually transformed into reflecting channels (a representative case is shown in Fig. 4.2(b)).

This suggests that the higher population in excited modes can induce the more backscattering of the graphene electron. An electron plane wave at normal incidence is entirely coupled to the fundamental eigenmode at the bottom end of the gate ($d = 0$) since their spatial profiles are identical. If the aspect ratio of a sawtooth, $a = L/W$ is large enough to make the entire structure adiabatic, the electron would stay in the fundamental eigenmode throughout propagating the structure and escapes to the other end, resulting in a perfect transmission regardless of the gate voltage. On the other hand, if the aspect ratio is very small, a sawtooth geometry asymptotically resembles to a straight bar and thus the Klein tunneling recovers. Therefore, the

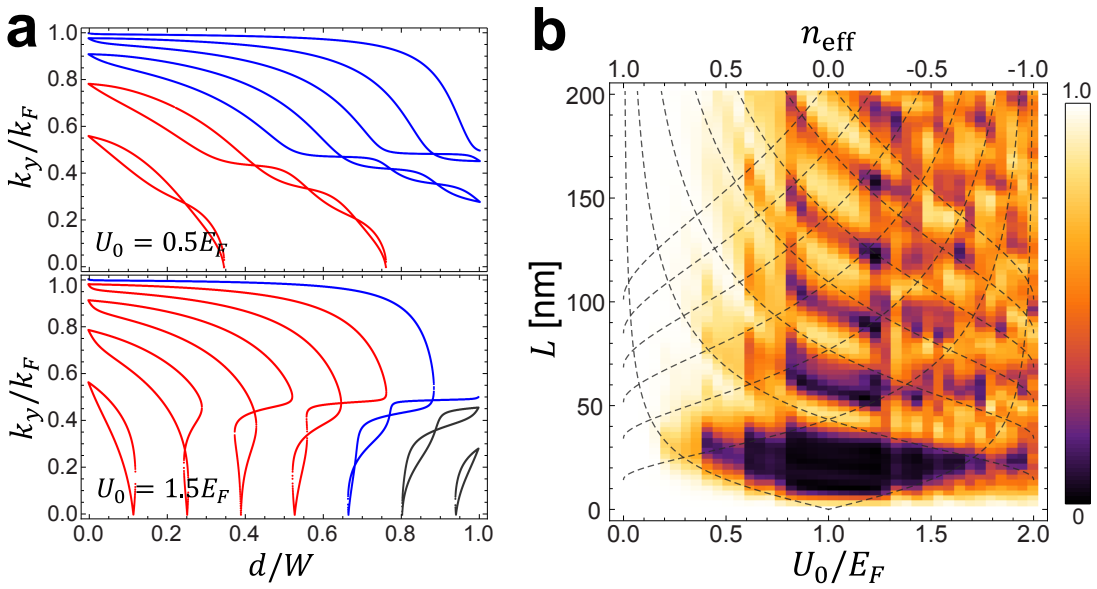

Figure 4.2: (a) The dependence of the eigenmodes formed in the valley regions (identified using the longitudinal momentum k_y) on the intervalley width d. This demonstrates how the connectivity of modes from $d = 0$ to $d = W$ can be transformed depending on the gate potential height U_0 (parameters here are chosen as $U_0 = 0.5E_F$ (top panel) and $1.5E_F$ (bottom panel), $W = 50$nm, and $E_F = 0.4$eV). When $U_0 = 0.5E_F$ (top panel), 5 eigenmodes at the bottom end ($d = 0$) are smoothly connected to the modes at the opposite top end ($d = W$), forming 5 electron transmitting channels out of total 9 modes. When $U_0 = 1.5E_F$ (bottom panel), only the fundamental mode is smoothly connected to the other end, while all higher order modes form electron reflecting channels. This illustrates that the guided mode connectivity is modulated through U_0.
(b) Transmittance (T) of a normally incident electron propagating through the sawtooth potential system for L ranging from 0 to 200nm and U_0 ranging from 0 to $2.0E_F$ ($W = 50$nm, $L_{\mathrm{bar}} = 20$nm). Dashed lines show the conditions for the total internal reflections of an electron ray. Within this range of device size, low T and high T regimes are well separated depending on U_0, which is explained in terms of (1) mode connectivity modulation and enhanced intermodal coupling due to nonadiabatic change of d (from the wave nature of graphene electrons) also by (2) the total internal reflection at the potential barrier interface (from the particle nature of the graphene electrons). The presence of well-defined low T regime implies that the conductance modulation is possible using sawtooth gate potential.

aspect ratio of the sawtooth must sufficiently small to ensure significant coupling between the eigenmodes, yet not too small to prevent the Klein tunneling.

Indeed, our numerical simulations (GraFDTD) [42], solving graphene electronic dynamics assuming ballistic and phase coherent transport, reveal that the electron tunneling can be substantially modulated by changing U_0, when L and W are of similar order of magnitude, as shown in Fig. 4.2(b). Electron ray tracing analysis adds more intuition on this system. The boundaries between high T and low T regions correspond well to the condition for total internal reflection, which is imposed by Snells law, $|\sin\Theta_m| \geq |n_{\text{eff}}|$, where Θ_m is the angle of incidence of an electron ray on the sawtooth boundaries at m-th reflection. The correspondence is apparent when a is small so that each electron ray undergoes only one reflection before it escapes the structure, but becomes less vivid in the opposite regime where the system acts more like a wave guiding structure. However, the ray tracing analysis does not provide a quantitative description. Particularly, even when the total internal reflection condition is satisfied, T never vanishes but has a finite value due to the wave nature of the electron, which is directly related to the off current of the device.

The bar-shaped blade back part, required to structurally connect the saw teeth into a single gate structure, also helps suppress the transmittance. Since the bar-shaped potential can only transmit electrons at nearly normal incidence [47], the blade back part further reflects the non-normal angle component of the transmitted electron through the sawtooth potential.

4.4 Device Parameter Optimization

The choice of proper device dimensions is vital to realize substantial backscattering. To illustrate this, consider an electron wave with $E_F = 0.4$eV, yielding the Fermi wavelength $\lambda_F = 10.3$nm, and $L = 60$nm. Transmittance through the sawtooth potential is a minimum when the aspect ratio of a sawtooth, $a \sim 3/8$, independent of the overall structure size, as shown in Fig. 4.3(a). Thus a is an important figure of merit of the sawtooth gate structure. Therefore, we choose $W(= L/a)$ as 160

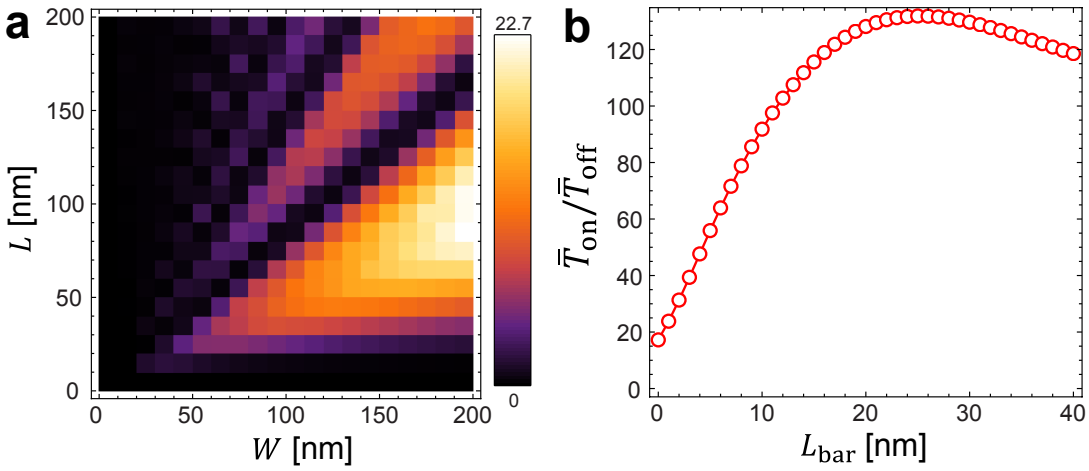

Figure 4.3: (a) Dependence of $\bar{T}_{\rm on}/\bar{T}_{\rm off}$ for normally incident electrons on the length dimensions of the sawtooth potential, L and W ($L_{\rm bar}$ is set as zero). The off state is defined as $U_0 = 1.1E_F$ =0.44eV. We observe that $\bar{T}_{\rm on}/\bar{T}_{\rm off}$ shows similar value for the same aspect ratio $a = L/W$, inferring that a is the key physical quantity determining the electron backscattering of sawtooth gate. The on/off ratio is nearly maximized when $a = 3/8$.
(b) Dependence of $\bar{T}_{\rm on}/\bar{T}_{\rm off}$ for normally incident electrons on the length of the blade back part of the gate electrode $L_{\rm bar}$. The device parameters are chosen as W =160nm and L =60nm. The off state is defined as $U_0 = 1.1E_F$ =0.44eV. Due to the further reflection from the blade back part, the on/off ratio increases up to ∼130 until $L_{\rm bar}$ ∼20nm, and then slowly degrades.

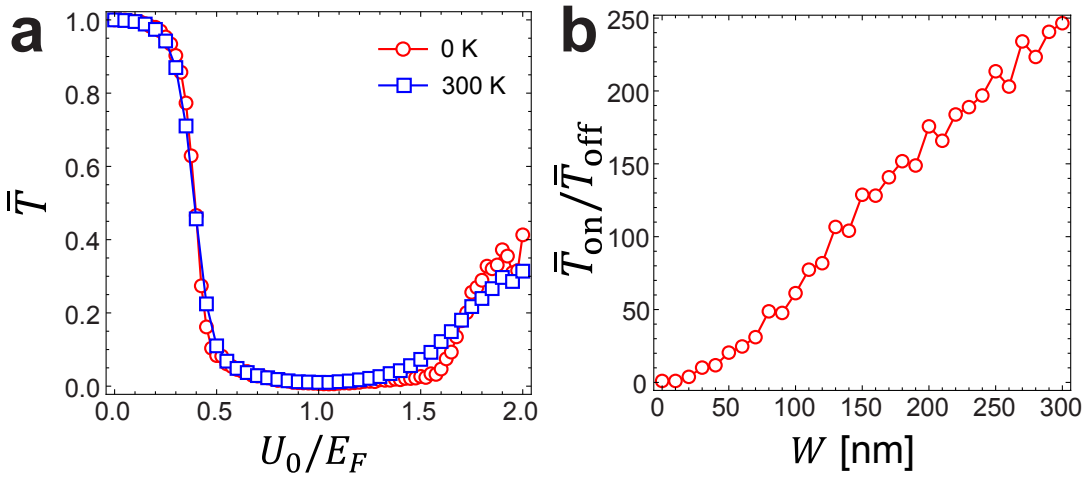

Figure 4.4: (a) The average transmittance ($\bar{T}$) of normally incident electrons is evaluated using finite difference time domain simulations for the case L =60nm, W =160nm, L_{bar}=20nm, and E_F =0.4eV while varying the top gate potential U_0. We observe a well-defined on/off behavior, showing $\bar{T}_{on}/\bar{T}_{off}$ =128 times enhanced compared to the bar-shaped gate for normally incident electrons (red circles). Considering the thermal broadening effect on the density of states at 300K, the well-defined on/off behavior is still pertained with $\bar{T}_{on}/\bar{T}_{off}$ =82 (blue squares).
(b) Dependence of $\bar{T}_{on}/\bar{T}_{off}$ on W is shown. The other length scales, L and L_{bar}, are chosen to be $3W/8$ and $W/8$ respectively; so that all the length scales of the gate electrode are scaled. When the device is scaled up with respect to the electron wavelength (λ_F), the on/off ratio increases linearly (the off current is measured at $U_0 = 1.1E_F$ =0.44eV). This implies that there is more room for optimization in between the device size (or the Fermi energy) and the on/off ratio.

nm. As L_{bar} increases for given L and W, the transmittance through the entire gate potential reaches its maximum when $L_{bar} \sim$ 20nm (Fig. 4.3(b)). Therefore, we set $L_{bar} = 20$nm.

4.5 Gate Modulation Properties

Figure 4.4(a) shows that the average transmittance $\bar{T}$ (defined in Section 4.2.3) of the optimized saw-shaped gate under normal incidence exhibits a sharp on/off behaviour depending on U_0. We demonstrate a maximum of $\bar{T}_{on}/\bar{T}_{off} \sim$130 for 0K and $\bar{T}_{on}/\bar{T}_{off} \sim$80 for 300K, which provides dramatic enhancements compared to the bar shaped gate. The on/off ratio can be further enhanced by decreasing λ_F of the elec-

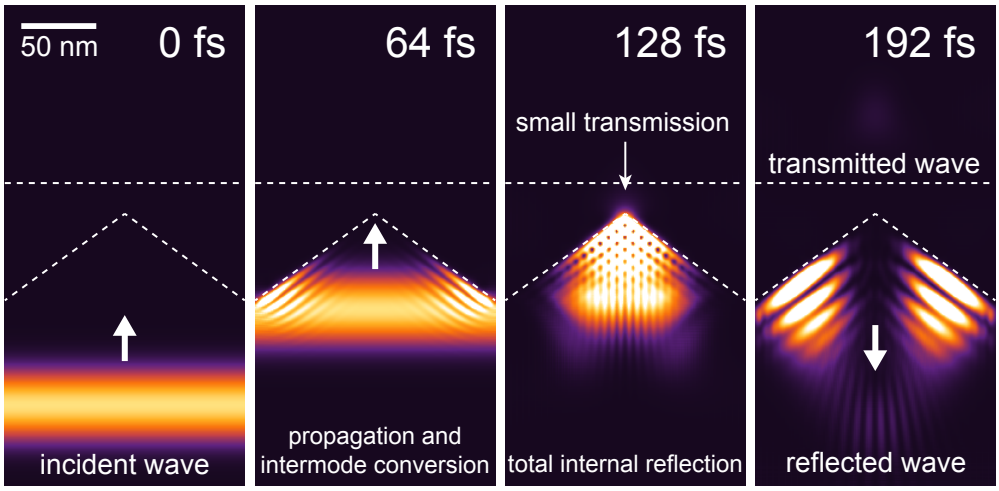

Figure 4.5: Snapshots of an electron probability density profile when the device is at the off state illustrate the electron backscattering mechanism (to track its position, the packet is localized in the y direction with the size of Δ_y =20nm nm). The device parameters are chosen as L =60nm, W =160nm, L_{bar} =20nm, E_F =0.4eV, and $U_0 = 1.1E_F$. The electron is introduced from the bottom boundary at $t = 0$. The Free standing electron travels, then it is coupled to the guided modes in the valley region of the gate potential (t =64fs). It further propagates along the y direction, and the electron wave undergoes a total internal reflection. Most parts of the electron wave are reflected back while small amount transmits the potential barrier induced by the top gate (t =128–196fs).

tron, either making the structure bigger or increasing E_F (Fig. 4.4(b)). This can be understood in terms of the decreased wave nature of the electron (responsible for the non-zero transmittance) as the length scale of the structure becomes larger with respect to the electron wavelength. From snapshots of GraFDTD simulations such as in Fig. 4.5, we find that most of the incident electron plane wave undergoes a total internal reflection and escapes the structure (ray tracing point of view). In other words, the incident fundamental eigenmode is converted to the backward propagating modes consisting electron reflecting channels due to the strong intermodal coupling inside the structure (waveguide point of view).

For obliquely incident electrons, we find that the highly suppressed transmission through the gate potential is still preserved for incidence angles in the range $|\theta| < 20^\circ$ even at room temperature. By applying Bloch boundary conditions along the transverse direction, we calculate $\bar{T}(\theta)$ for $U_0 = 1.1E_F = 0.44$eV (Fig. 4.6). This

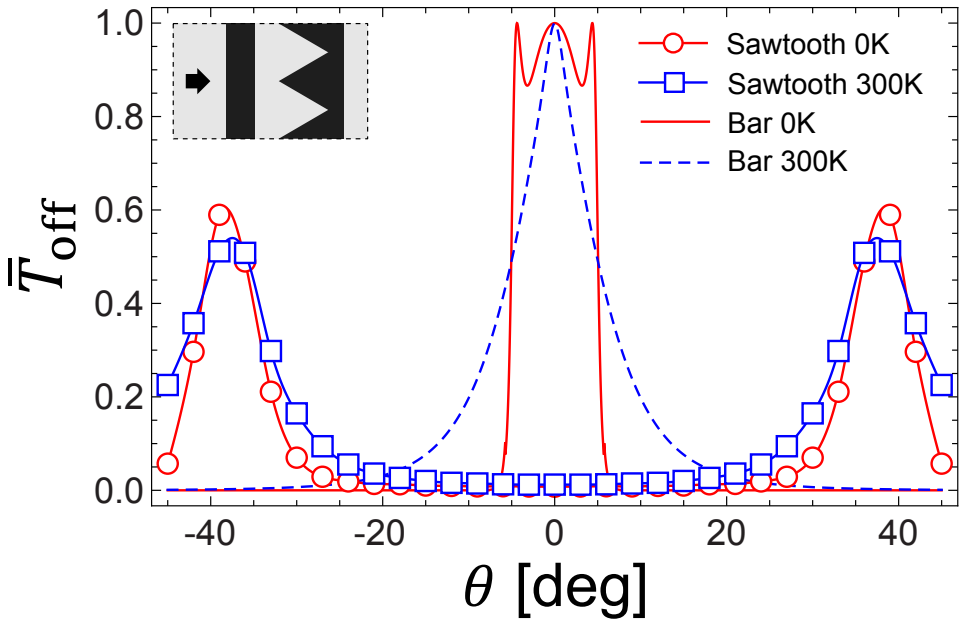

Figure 4.6: Dependence of the off state transmittance ($\bar{T}_{\rm off}$; measured at $U_0 = 1.1E_F$ =0.44eV) on the incident angle (θ) for the sawtooth gate potential with L =60nm, W =160nm, and $L_{\rm bar}$ =20nm at zero temperature (red circles) and at room temperature (blue squares). For comparison, same plots for the bar-shaped gate potential with the gate length of $L + L_{\rm bar}$ =80nm are shown for 0K (red solid) and 300K (blue dashed). The sawtooth gate potential shows highly suppressed transmission near normal incidence $|\theta| < 20°$ even at room temperature, while the bar-shaped gate potential shows considerably high transmittance for the same range of θ. Note that the electrons with smaller incident angle contribute more on the total current flow compared to those have larger θ. Recognizing that the bar-shaped gate potential exhibit little transmittance for large angle of incidence $|\theta| > 20°$, it may further enhance the size of the θ window for low T by placing a bar-shaped gate and a sawtooth gate in series (see the inset).

shows that the saw-shaped gate potential exhibits large electron backscattering over a substantial angular range near 0 degrees, which is the dominant incident angle for electron current flows driven by the electric field applied from the source to the drain electrode. Furthermore, we propose a dual gate system composed of a saw-shaped gate electrode and a bar-shaped gate electrode in series could be used to suppress electron transmittance by reflecting both normally incident and non-normally incident electrons in series (see the inset of Fig. 4.6).

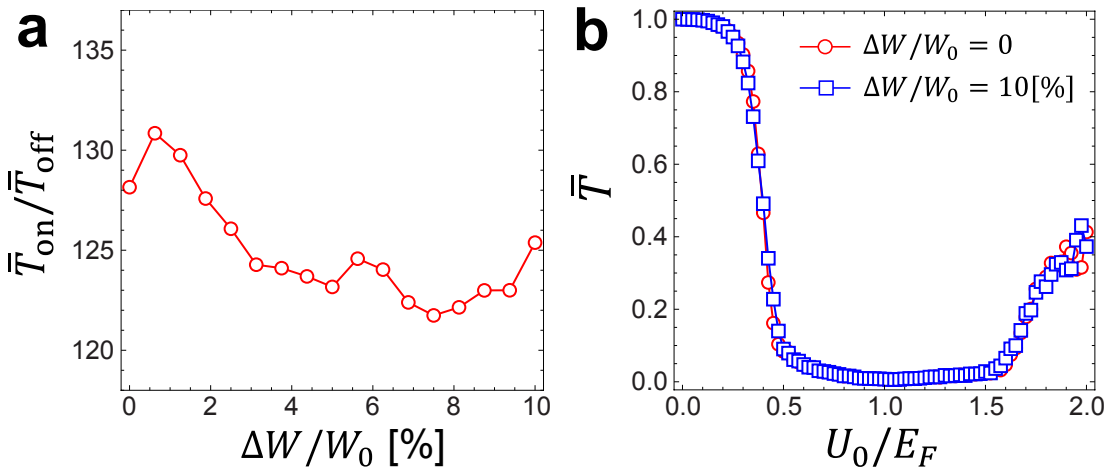

Figure 4.7: (a) $\bar{T}_{\rm on}/\bar{T}_{\rm off}$ for normally incident electrons when the perfect periodicity of the sawtooth potential structure is broken by including two different tooth-widths of $W_\pm = W \pm \Delta W$. While changing $\Delta W/W$ up to 10%, the on/off ratio is marginally varied. (b) Gate modulation when the periodicity of the sawtooth potential is perfect (red circles) and perturbed by 10% (blue squares). Both exhibit well-defined on/off switching behaviors.

4.6 Robustness Analysis

To further check the robustness of our switching mechanism, we perform several analyses on the effects of (a) periodicity perturbation (Fig. 4.7), (b) potential blurring (Fig. 4.8), and (c) finite temperature (Fig. 4.9(a)). Finally, we demonstrate our proposed mechanism is still working even under a combination of the aforementioned conditions by showing on/off behavior of a realistic device (Fig. 4.9(b)). Throughout the analyses, the device parameters are chosen to be W_0 =160nm, L =60nm, and $L_{\rm bar}$ =20nm. The off state is defined as $U_0 = 1.1E_F$ =0.44eV.

4.6.1 Periodicity Perturbation

We study the case when the perfect periodicity of the sawtooth potential structure is broken by including two different tooth-widths of $W_\pm = W_0 \pm \Delta W$. While changing $\Delta W/W_0$ up to 10%, the on/off ratio varies less than 5% (Fig. 4.7(a)) We also observe a well-defined on/off behavior in the presence of the perturbation (Fig. 4.7(b)).

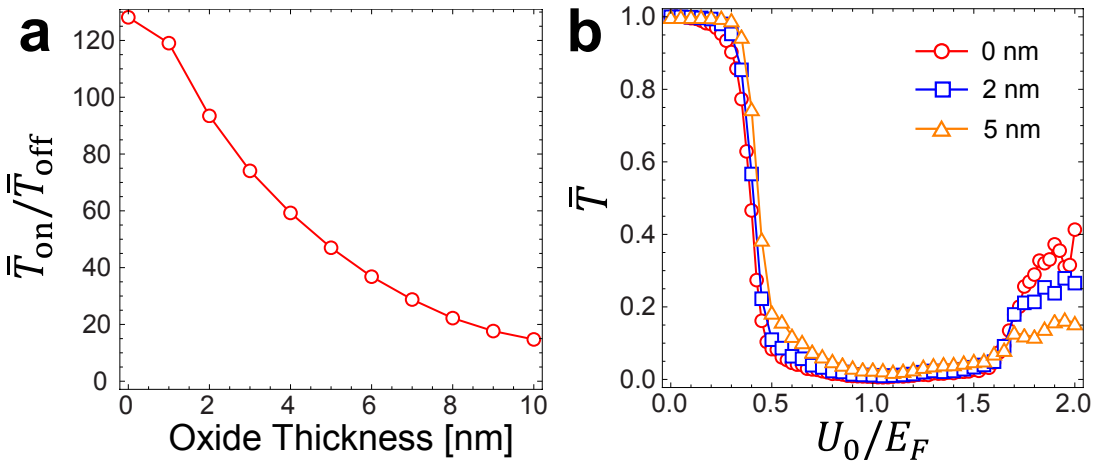

Figure 4.8: (a) $\bar{T}_{\rm on}/\bar{T}_{\rm off}$ for normally incident electrons when the sawtooth gate potential is blurred due to the finite thickness of the HfO_2 oxide layer with relative permittivity of 25. The top gate potential profile for given oxide thickness is calculated by solving Poisson equation using finite element method. As the oxide thickness increases, i.e., as the potential is blurred, the on/off ratio degrades. The current fabrication technique allows the deposition of HfO_2 layer with ∼2nm thickness, where the calculated on/off ratio is as high as 95. (b) When the HfO_2 oxide thickness is finite (2nm case is shown with blue squares, 5nm case is shown with orange triangles, and the case without oxide layer is shown with red circles), we still observe well-defined on/off behaviors.

4.6.2 Potential Blurring

It is practically challenging to apply an electric potential which has a subnanometer sharp spatial profile due to the inclusion of an oxide layer between graphene and the gate electrode. To investigate the effect of the potential blurring, we first solve the electrostatic equations using the finite element method and obtain the spatial profile of the carrier density $n(x, y)$ throughout the simulation region. Here the top gate electrode is assumed to have the perfect sawtooth shape, and the space between the gate electrode and graphene is filled with an oxide layer of thickness h. For the gate oxide material, we choose HfO_2 which has the dielectric constant of 25 [105]. We then convert the carrier density profile to the potential profile applied by the top gate $U(x, y)$ by using

$$n(x,y) = \frac{(E_F - U(x,y))^2}{\pi v_F^2 \hbar^2}, \tag{4.6}$$

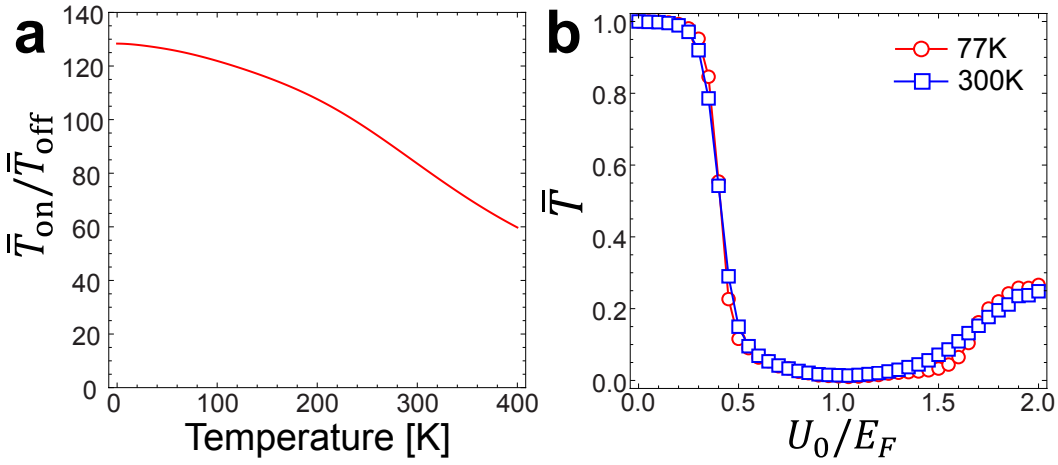

Figure 4.9: (a) Temperature dependence of $\bar{T}_{on}/\bar{T}_{off}$ for normally incident electrons. Electron transport is assumed to be phase coherent. (b) A realistic behavior of the average transmittance $\bar{T}$ as a function of U_0. The thickness of the HfO_2 oxide layer is assumed to be 2 nm. $\bar{T}_{on}/\bar{T}_{off}$ is as high as 95 at zero temperature, 92 at 77K (red circles), and 65 at room temperature (blue squares).

where v_F is the Fermi velocity and E_F is the Fermi energy outside the barrier. Finally, our finite difference time domain simulator solves the time dependent Dirac equations for two dimensional massless fermions with the potential profile $U(x, y)$. The simulation results show that the on/off ratio degrades as the oxide thickness increases, i.e., as the potential gets more blurred (Fig. 4.8(a)). The current fabrication technique allows the deposition of HfO_2 layer with ~2nm thickness [89], where the calculated on/off ratio is as high as 95. As shown in Fig. 4.8(b), we still observe well-defined on/off behavior even when the oxide layer thickness is 5nm. These results suggest that the development of high-K dielectric materials and precise fabrication will be of importance to minimize the performance degradation.

4.6.3 Finite Temperature

When temperature τ is nonzero, the average transmittance in equilibrium ($\mu_S = \mu_D = E_F$) can be written as

$$\bar{T} = \int dE\ T(E)\frac{df(E)}{dE} = \int dE \frac{T(E)}{\tau} \frac{e^{(E-E_F)/\tau}}{\left(e^{(E-E_F)/\tau}+1\right)^2}. \tag{4.7}$$

The effect of thermal broadening becomes significant when the temperature is comparable to the other energy scales such as the Fermi energy or the applied potential energy. The performance degradation turns out to be 30% at room temperature (Fig. 4.9(a)). Further theoretical investigation using the non-equilibrium Greens function formalism combined with tight binding model [36] or density functional theory will enable us to take into account the effects of finite drain source bias and high temperature dephasing.

4.7 Summary and Outlook

In this chapter, we proposed a sawtooth shaped gate geometry for graphene field effect transistors and theoretically demonstrated that our gate design leads to a hundred-fold enhancement in on/off ratio for normally incident electrons without any band gap engineering. It may be possible to further reduce the transmission by configuring sawtooth shapes other than linear to engineer the mode conversion in more effectively. Combining our gate design with minimal band gap engineering may also substantially increase the on/off ratio with marginal change in the carrier mobility. Since our proposed mechanism for graphene field effect transistors is quite robust, we anticipate that it can be experimentally realized. Moreover, our current theoretical study opens a new possibility for graphene-based device optimization by *engineering the gate geometry*, which has never been considered before.

Chapter 5

Plasmonic Fano Resonance in Graphene Subwavelength Waveguide Modulator

5.1 Introduction

Graphene has drawn great attention due to its exceptional electronic transport properties [9, 13, 26, 66, 73]. Recent investigations have also revealed that a single layer of graphene can support mid-infrared plasmons with an extremely high confinement factor of ∼100 without too much propagation loss [17, 32, 41, 56, 103]. Moreover, the optical properties of graphene strongly depend on its chemical potential (E_F), which is tunable by electrostatic gating, making it an ideal material for optical modulators. Researchers have demonstrated a graphene based optical waveguide modulator by utilizing the optical absorption due to the interband transitions can be suppressed by raising the Fermi energy above the half of the incident photon energy ($E_F > \omega/2$) [60]. However, long propagation distances are required to achieve a noticeable change in transmittance. Graphene nano resonator *arrays* can also induce a significant modulation in the transmission and the reflection of plane waves [46, 99, 109], but the geometry is not ideal for on-chip switching applications.

In this chapter, we show how to design a deep-subwavelength plasmonic waveguide modulator which regulates the transmission of a metal-insulator-metal (MIM) waveguide by controlling the plasmon resonance in graphene. We first investigate

the mode conversion characteristics at the junction between the MIM waveguide and the graphene modulator using the finite element method (FEM) simulation. We then show that the modulator shows an asymmetric Fano resonance [29] due to the interference between plasmon resonance in graphene and nonresonant background transmission. In particular, we demonstrate that it is possible to almost completely turn off the transmission by employing destructive interference between the resonant and nonresonant transmission. Finally, we discuss the dependence of the device performance on the carrier mobility of graphene.

The structure is composed of two identical MIM waveguides connected by a sheet of graphene (see Fig. 5.1). The MIM waveguide consists of a SiO_2 dielectric slab sandwiched by top and bottom gold layers. The thickness of the core d and the cladding h are chosen to be $d = h = 100$nm. The gap between the waveguides, which corresponds to the active region of the graphene modulator, is $L = 140$nm. The graphene is electrically connected to the top gold layer, which allows us to tune its carrier density by electrostatic gating. The photon energy is chosen to be 0.165eV in order to suppress absorption losses due to the vibration modes in SiO_2 ($\omega \sim 0.133$eV) [75] and the optical phonons in graphene ($\omega \gtrsim 0.2$eV) [41]. The carrier mobility of the graphene is assumed to be $\mu = 10^4 \mathrm{cm}^2\mathrm{V}^{-1}\mathrm{s}^{-1}$ [74].

5.2 Mode Conversion

In this section, we investigate conversion properties between MIM TM_0 mode and graphene TM plasmon.

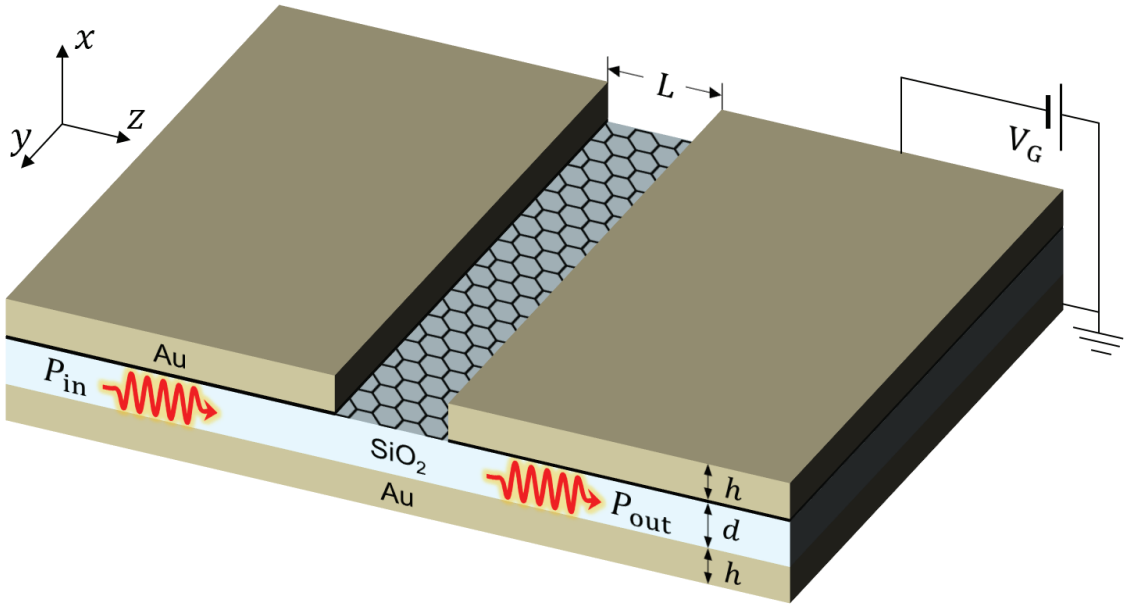

Figure 5.1: Schematic of graphene plasmonic waveguide modulator. Two identical MIM waveguides are connected by a sheet of graphene. The thickness of SiO_2 core d and the gold cladding h, and the gap between the MIM waveguides L are chosen to be $d = h = 100$nm, and $L = 140$nm in order to exhibit good switching behavior at $E_F \sim 0.4$eV. The modulator is designed for photon energy of 0.165eV.

5.2.1 Eigenmode Field Profile

Eigenmodes of MIM and graphene waveguides can be calculated by solving Maxwell's equations. Let us first assume that the the magnetic field H_y has the form

$$H_y(x,z) = \begin{cases} De^{i\beta z}e^{\gamma_3(x+d/2)} & \text{where } x < -d/2, \\ e^{i\beta z}\left(Be^{\gamma_2(x-d/2)} + Ce^{-\gamma_2(x-d/2)}\right) & \text{where} |x| \leq d/2, \\ Ae^{i\beta z}e^{-\gamma_1(x-d/2)} & \text{where } x > d/2, \end{cases} \tag{5.1}$$

where d is the thickness of the dielectric core, β is the propagation constant , and $\gamma_i = \sqrt{\beta^2 - k_0^2\epsilon_i}$ is defined for each layer of permittivity ϵ_i. The electric field profile

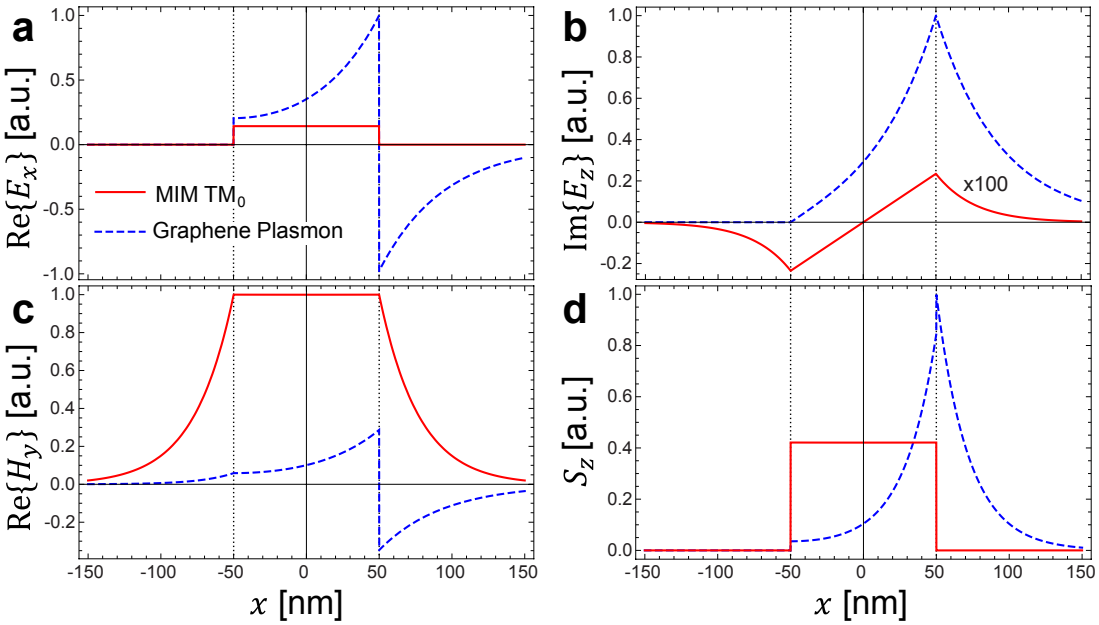

Figure 5.2: (a) Re$\{E_x\}$, (b) Im$\{E_z\}$, (c) Re$\{H_y\}$, and (d) z component of the time averaged Poynting vector $S_z = \text{Re}\{(\mathbf{E} \times \mathbf{H}^*)_z\}/2$ profiles of MIM TM$_0$ (red solid) and graphene TM plasmon (blue dashed) modes at $E_F = 0.4$eV. Field amplitudes are normalized such that the power flow $\int S_z dx$ of both modes are identical. The effective mode indices of MIM TM$_0$ (n_{MIM}) and graphene plasmons (n_G) are respectively $n_{\text{MIM}} = 1.11 + 0.033i$ and $n_G = 27.1 + 0.27i$.

is directly deduced from H_y,

$$E_x(x,z) = \frac{\beta}{\omega\epsilon_0\epsilon} H_y(x,z), \tag{5.2}$$

$$E_z(x,z) = \frac{i}{\omega\epsilon_0\epsilon} \frac{\partial H_y(x,z)}{\partial x}. \tag{5.3}$$

At the material interfaces ($x = \pm d/2$), each field component obeys the following boundary conditions,

$$E_z\left(x \to \pm d/2^+\right) = E_z\left(x \to \pm d/2^-\right), \tag{5.4}$$

$$H_y\left(x \to -d/2^+\right) = H_y\left(x \to -d/2^-\right), \tag{5.5}$$

$$H_y\left(x \to d/2^+\right) - H_y\left(x \to d/2^-\right) = \sigma E_z\left(x = d/2\right), \tag{5.6}$$

where σ is the tunable sheet conductivity of graphene. By inserting the ansatz to the

boundary conditions and solving the resulting linear equations, we obtain the field profiles and the effective indices of the modes.

For the MIM waveguides, $\epsilon_1 = \epsilon_3 = \epsilon_{\mathrm{Au}} = -1880 + 670i$ and $\epsilon_2 = \epsilon_{\mathrm{SiO_2}} = 0.81$ at $\omega = 0.165\mathrm{eV}$ [75]. The field profile of MIM TM_0 mode is plotted in Fig. 5.2 (red solid lines). Note that the surface parallel electric field E_z of MIM TM_0 mode nearly vanishes, and so does the current flow in the graphene. This implies the properties of MIM TM_0 mode are little perturbed by the graphene layer, because the left side of Eq. (5.6) is negligible. In the graphene modulator region, the topmost layer is switched to air (i.e., $\epsilon_3 = 1$), which allows the graphene to support plasmon modes depicted in Fig. 5.2. The effective mode indices of MIM TM_0 (n_{MIM}) and graphene plasmons (n_G) are calculated to be $n_{\mathrm{MIM}} = 1.11 + 0.033i$ and $n_G = 27.1 + 0.27i$ respectively.

5.2.2 Mode Conversion between MIM TM_0 and Graphene Plasmon

To numerically investigate the conversion between MIM TM_0 and graphene plasmon modes, we model the graphene as a thin film of the thickness δ =0.3nm and impose the permittivity

$$\epsilon_G = 1 + i\frac{\sigma}{\epsilon_0 \omega \delta}. \tag{5.7}$$

We calculate the steady state solution of the system using the finite element method, and then decompose the resulting field distribution into the eigenmodes.

Figure 5.3(a) shows the electric field distribution at the MIM and graphene waveguide interface at $E_F = 0.4\mathrm{eV}$. The incident MIM TM_0 mode, which is launched from the left side, split into backward propagating MIM TM_0 mode (reflection), forward propagating graphene TM plasmons (transmission), unbound radiation and weakly bound surface plasmon polaritions (SPP) on gold surface. The mode conversion properties are identified as the complex transmission (t_{MG}) and reflection (r_{MG}) co-

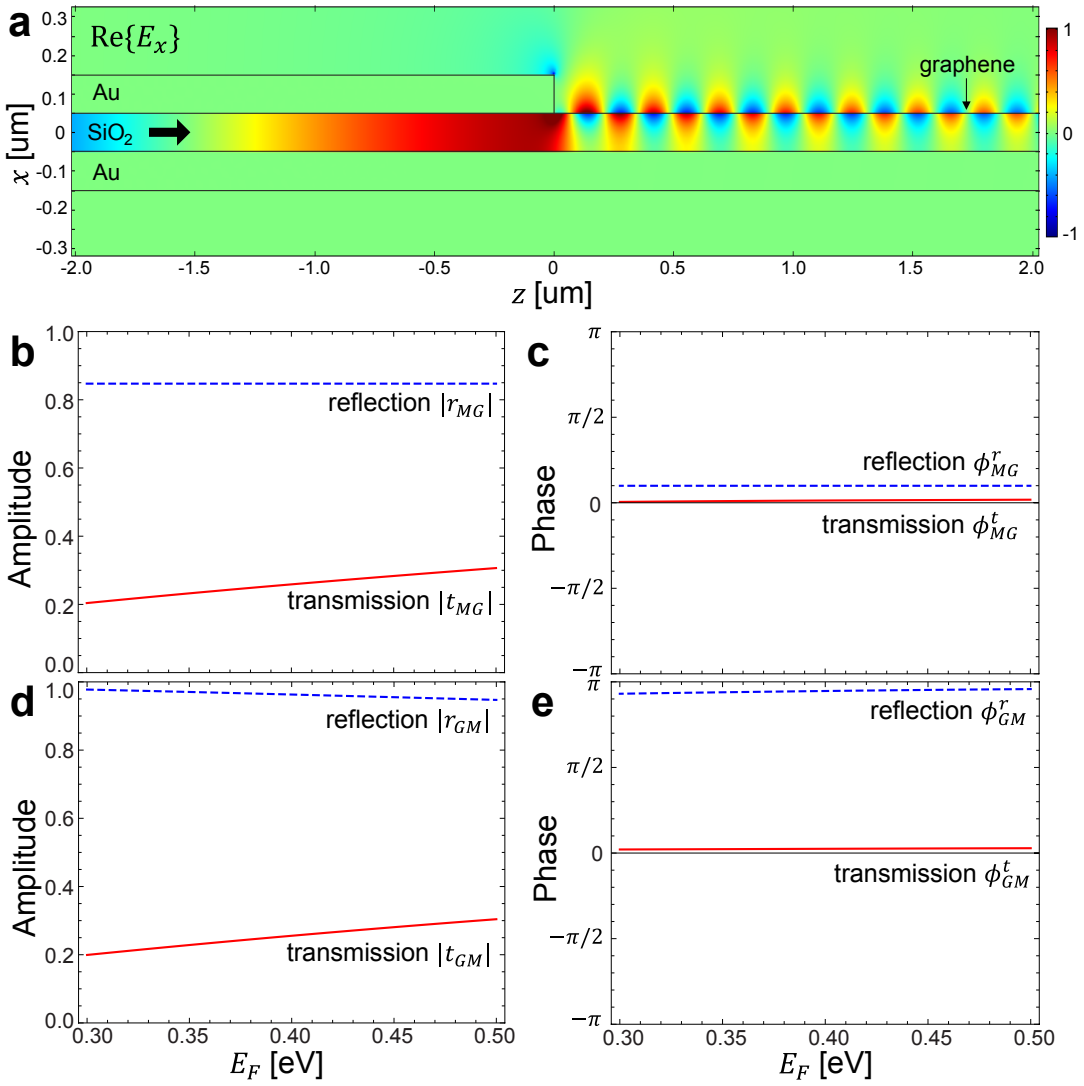

Figure 5.3: (a) Re$\{E_x\}$ distribution at the MIM and graphene waveguide interface at $E_F = 0.4$eV. MIM TM_0 mode is launched from the left side and split into backward propagating MIM TM_0 mode (reflection), forward propagating graphene plasmons (transmission), unbound radiation, and weakly bound surface plasmons on gold surface. The Fermi energy dependence of (b) the amplitude and (c) the phase of the reflection ($r_{MG} = |r_{MG}| \exp(i\phi^r_{MG})$, blue dashed) and the transmission ($t_{MG} = |t_{MG}| \exp(i\phi^t_{MG})$, red solid) coefficients for the incoming MIM TM_0. (d) The amplitude and (e) the phase of the reflection ($r_{GM} = |r_{GM}| \exp(i\phi^r_{GM})$, blue dashed) and the transmission ($t_{GM} = |t_{GM}| \exp(i\phi^t_{GM})$, red solid) coefficients for the incoming graphene plasmon mode.

efficients. Similarly, we also examine the mode conversion characteristics for the incoming graphene plasmons.

The amplitude of the each coefficient is defined as $|t|^2 = P_t/P_i$ and $|r|^2 = P_r/P_i$, where P_i, P_t, and P_r are the time averaged power carried by the incident, transmitted, and reflected modes. The phase term is determined such that

$$\phi^{t,r} = \arg\left[\frac{E_x^{t,r}}{E_x^i}\right]_{x=0}, \tag{5.8}$$

where the complex electric field components E_x^i, E_x^t, and E_x^r are evaluated at the junction. We immediately notice the correspondence between the conversion efficiency from MIM TM_0 to the graphene plasmon $|t_{MG}|^2$ and that from the graphene plasmon to MIM TM_0 $|t_{GM}|^2$, which is likely due to the reciprocity of the system. Depending on the Fermi energy, the conversion efficiency varies from 4% to 9% (Fig. 5.3 (c) and (d)). Note that $|r_{MG}|^2 + |t_{MG}|^2$ is only around 0.8. This indicates that there is a substantial coupling to the continuum of unbound radiation modes and the weakly bounded SPP on gold surface, which is crucial for the modulator to exhibit a sharp switching behavior originated from Fano resonance that we will revisit in the next section. In contrast, the graphene plasmons do not significantly scatter into the free space continuum ($|r_{GM}|^2 + |t_{GM}|^2 \sim 1$). The vertical air-metal interface at the waveguide junction imposes a π phase shift upon reflection of the graphene plasmon ($\phi_{GM}^r \sim \pi$), but little phase change on MIM TM_0 reflection ($\phi_{MG}^r \sim 0$).

5.3 Modulation Mechanism

Now let us discuss how our graphene waveguide modulator behaves as we change the Fermi level E_F. The overall transmittance of an incident MIM TM_0 wave shows a peak at $E_F = E_{\text{on}} = 0.38\text{eV}$, but suddenly drops down and almost vanishes at $E_F = E_{\text{off}} = 0.395\text{eV}$, as depicted in Fig. 5.4(a). This sharp modulation is ideal for on-chip optical switch applications. Imagine the graphene sheet is chemically doped such that the carrier density $n_{\text{on}} = E_{\text{on}}^2/(\pi\hbar^2 v_F^2) \approx 1.06 \times 10^{13}\text{cm}^{-2}$, which is the

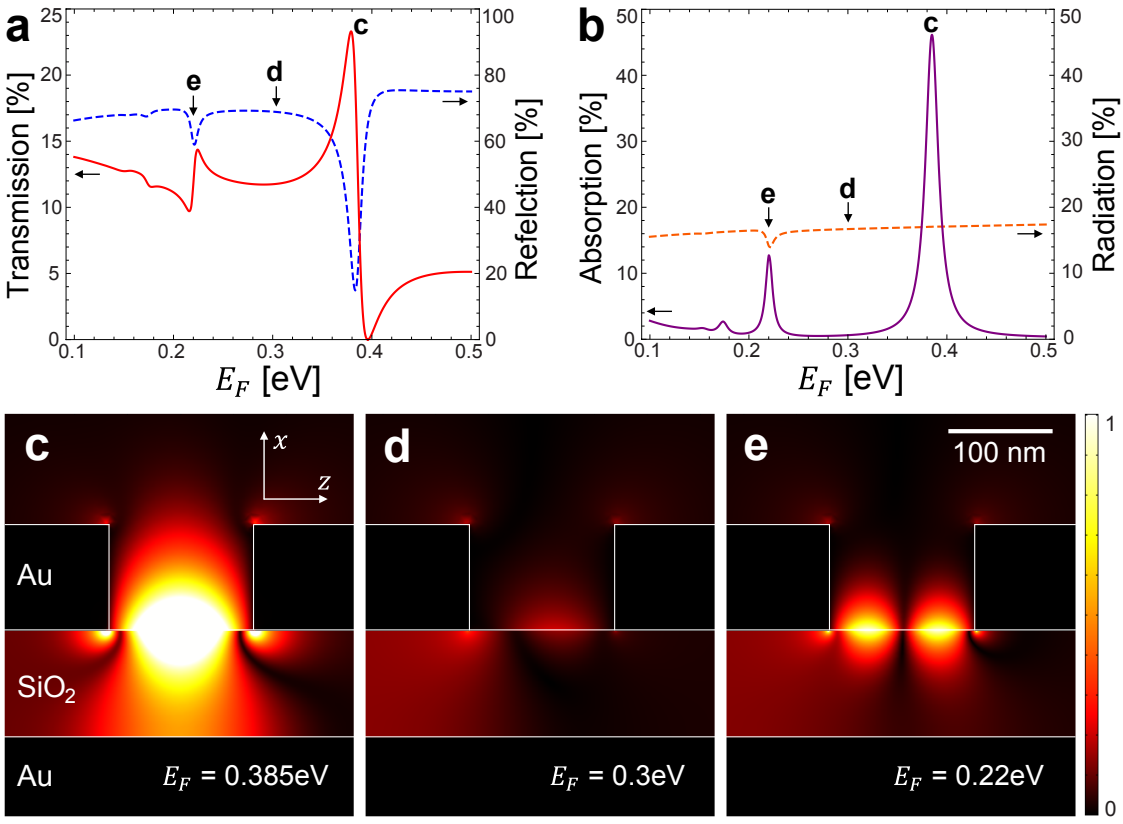

Figure 5.4: (a) The transmittance (red solid), the reflectance (blue dashed), (b) the absorption (purple solid), and the radiation loss (orange dashed) of the graphene waveguide modulator. The geometrical parameters are chosen as $d = h = 100$nm and $L = 140$nm, and the carrier mobility of the graphene is assumed to be $\mu = 10000\text{cm}^2\text{V}^{-1}\text{s}^{-1}$. The amplitude of the x component of the electric field ($|E_x|$) at (c) $E_F = 0.385$eV (fundamental resonance), (d) 0.3eV (off resonance), and (c) 0.22eV (second-order resonance) are plotted in the same scale.

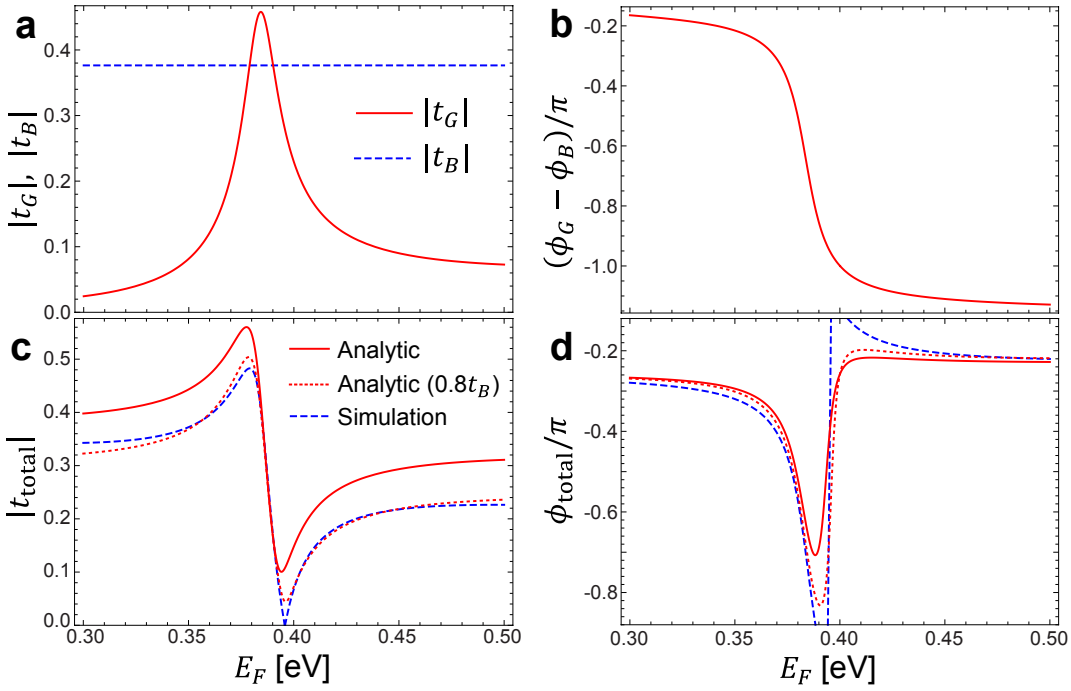

Figure 5.5: (a) The amplitude of the transmission through the graphene plasmon resonance (t_G, red solid) and through background (t_B, blue dashed) versus E_F. (b) The phase difference between t_G and t_B, $\phi_G - \phi_B = \arg(t_G) - \arg(t_B)$. The dependence of (c) the amplitude and (d) the phase of the total transmission coefficient, $t_{\text{total}} = t_G + t_B$, on E_F. t_B is crudely approximated as the transmission through the same device but in the absence of graphene layer (red solid). The analytic calculation using $t'_B = 0.8t_B$ (red dotted) shows better accordance to the full simulation result (blue dashed), because t_B is overestimated.

"on" state. To turn the switch "off", we need to apply a static gate voltage V_G between the bottom metal layer and the graphene to raise the carrier concentration by $\Delta n = (E_{\text{off}}^2 - E_{\text{on}}^2)/(\pi\hbar^2 v_F^2) \approx 8.5 \times 10^{11}\text{cm}^{-2}$. The capacitance of the system is $C_G = 34.5\text{nF/cm}^2$, leading us to the conclusion that it only requires $V_G = e\Delta n/C_G \approx 3.96\text{V}$ for the switching operation. Due to the symmetry in the graphene electronic band, the above arguments are still valid for the hole doped case.

In addition to the well-defined switching behavior, this modulator design is also advantageous in integration. By conservatively assuming a diffraction-limited width $W \sim \lambda_0 = 7.5\mu\text{m}$, the active volume of the device can be approximated as $V \approx (d + 2h)LW \sim 10^{-3}\lambda_0^3$. Such extreme miniaturization is a consequence of the highly confined nature of the graphene plasmons.

The asymmetric transmission line shape is originated from the interference between the resonant transmission t_G through the graphene plasmons and the background transmission t_B through the continuum of the unbound modes and the weakly bound gold surface plasmons. This type of resonance, which was first explained by Fano [29], generally occurs when a discrete state is embedded in a continuum [61, 70]. The transmission through graphene plasmon t_G is analogous to the Fabry-Perot resonance [11] and can be analytically calculated from the previously obtained transmission coefficients at the waveguide junction,

$$t_G = \frac{t_{MG} t_{GM} \exp\left(i n_G k_0 L\right)}{1 - r_{GM}^2 \exp\left(2 i n_G k_0 L\right)}, \tag{5.9}$$

where k_0 is the free space wavenumber. As a crude approximation, we assume that t_B is the same as the transmission through the same device but in the absence of graphene layer. The resulting analytic transmission coefficient ($t_{\text{total}} = t_G + t_B$) well reproduces the full FEM simulation result, including the distinctive asymmetric line shape and the peak positions, as seen in Fig. 5.5(c) and (d). However, there is a constant offset between the analytic and the simulation transmission amplitudes. This is mainly because t_B is overestimated, since the modes participating in transmission in the device without graphene are not completely orthogonal to the graphene plasmon mode in the actual device. By assuming a reduced background transmission $t'_B = 0.8 t_B$, the analytic calculation almost exactly matches the simulation.

Indeed, the maximum and the minimum transmission occur at opposite sides of the absorption peak coming from the plasmon resonance in graphene at $E_F = 0.385\text{eV}$ (Fig. 5.4(b)). The amplitude distribution of E_x clearly reveals that such changes in transmission are associated with the fundamental resonance of graphene plasmons (Fig. 5.4(c)). A weaker but similar modulation is also observed around $E_F = 0.22\text{eV}$, where the second-order resonance occurs.

5.4 Device Parameter Dependence

The gap between the two MIM waveguides, L, determines the Fermi energy (E_{res}) at which the graphene plasmons are in resonance. The condition for the fundamental resonance is analytically deduced from Eq. (5.9),

$$\phi^r_{GM}(E_{\text{res}}) + \text{Re}\{n_G(E_{\text{res}})\}k_0 L = 2\pi. \tag{5.10}$$

A smaller gap lowers E_{res}, and thus also reduces the gate voltage required for switching operation. As a trade off, the plasmon propagation loss in graphene also increases (Fig. 5.3), resulting in a weaker modulation as presented in Fig. 5.6(a).

To achieve higher on-state transmittance T_{on}, one can enhance either the background transmission or the resonant transmission. The relative phase between both transmission processes also matters, but is less important. For example, thickening the metal cladding monotonically increases T_{on} by enforcing the background transmission (Fig. 5.6(c)). As discussed earlier, the resonant transmission can be enhanced by increasing L, and so is T_{on}. Changing the thickness of the dielectric core d is more complicated, since it considerably affects both on t_B and t_G.

The off-state transmittance, T_{off}, is more subtle. It is a necessary but not sufficient condition for vanishing T_{off} that the resonant transmission is stronger than the background transmission (i.e., $|t_G(E_{\text{res}})| > |t_B|$). To get a totally destructive interference, the phase difference between t_G and t_B also needs to be carefully adjusted. Here we demonstrate that such complete cancellation can be accomplished by engineering the geometry of the system. Figure 5.6(d) plots the on/off transmittance ratio $T_{\text{on}}/T_{\text{off}}$ as a function of h and d. Indeed $T_{\text{on}}/T_{\text{off}}$ sharply diverges along the red dashed line indicating the condition for the total destructive interference. On the other hand, if $|t_G(E_{\text{res}})| < |t_B|$, the transmission can never be totally suppressed.

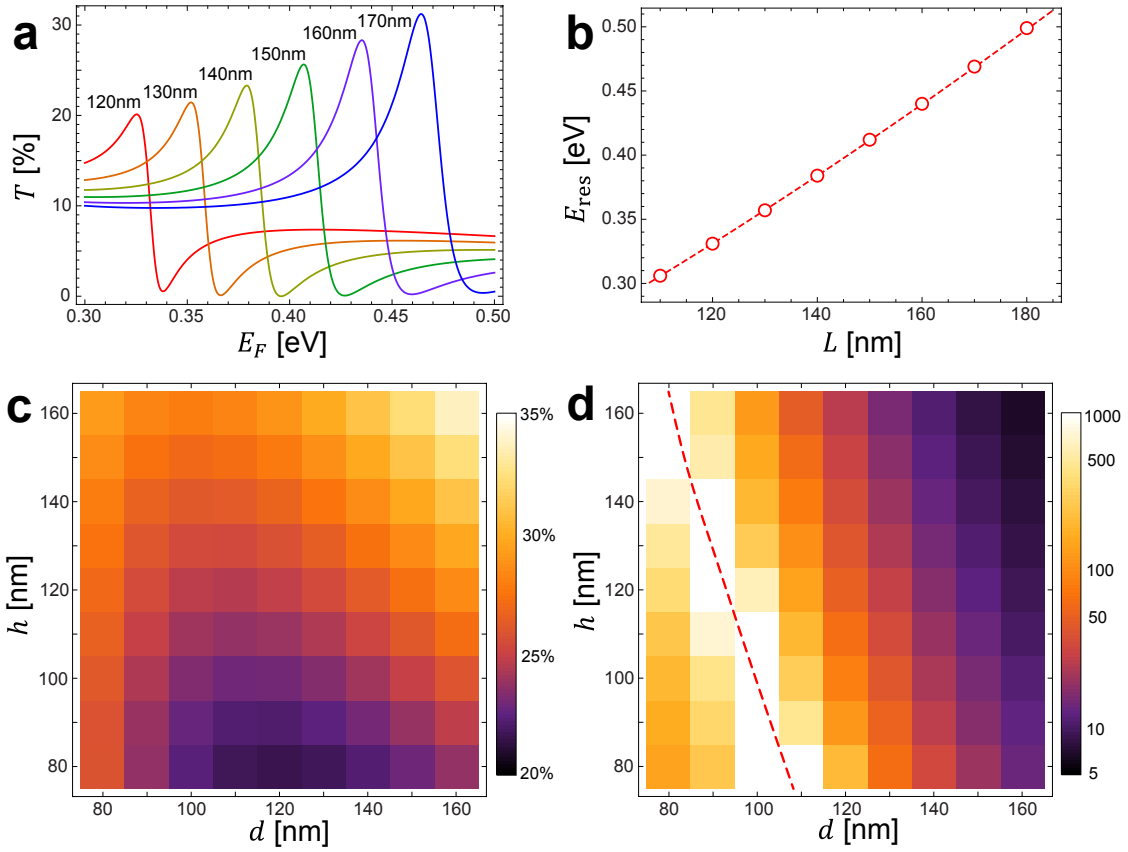

Figure 5.6: (a) The transmittance T versus E_F for modulator length $L = 120$ (red), 130, ..., 170nm (blue). (b) Dependence of E_{res} on L. The analytic curve (red dashed) almost perfectly agrees with the FEM simulation results (red circles). (c) the on-state transmittance T_{on} and (d) the on/off transmittance ratio $T_{\text{on}}/T_{\text{off}}$ are plotted as functions of the dielectric core thickness d and the metal cladding thickness h. The red dashed line in (d) shows the condition for the total destructive interference between the resonant transmission and the background transmission.

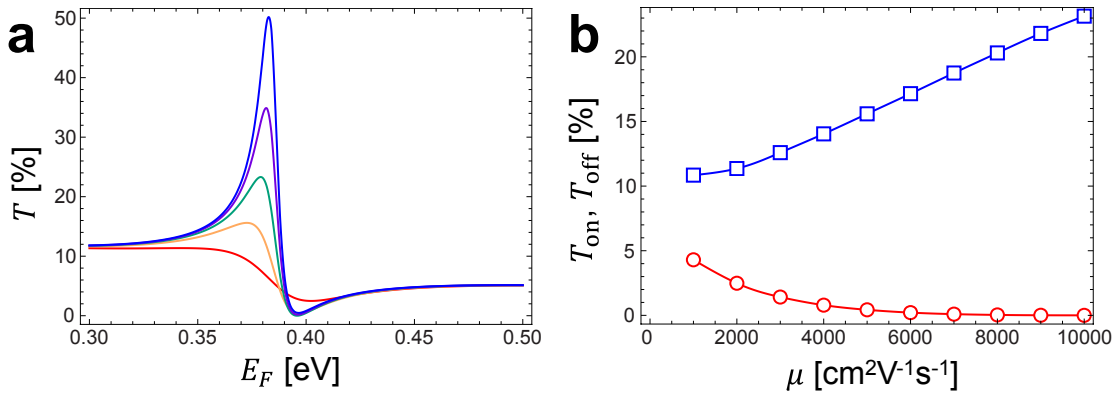

Figure 5.7: (a) The transmittance T versus E_F for carrier mobility $mu = 2000$ (red), 5000, 10,000, 20,000, and 50,000cm^{2}V^{-1}s^{-1} (blue). (b) Dependence of $T_{\rm on}$ (blue squares) and $T_{\rm off}$ (red circles) on μ. As graphene gets more lossy (i.e., μ decreases), the resonant transmission amplitude, $|t_G(E_{\rm res})|$, also diminishes and becomes even smaller than the background transmission $|t_B|$. As a result, the device shows weaker modulation. $|t_G(E_{\rm res})| \geq |t_B|$ for $\mu \geq 4900$cm^{2}V^{-1}s^{-1}.

5.5 Carrier Mobility Dependence

The carrier mobility of graphene μ varies from 10^3 to 10^6cm^{2}V^{-1}s^{-1} depending on the fabrication method [74, 78] and the substrate material [9, 10, 21, 74]. The optical loss of graphene is inversely proportional to μ. We found that $T_{\rm on}$ can be as high as 50% for $\mu = 5 \times 10^5$cm^{2}V^{-1}s^{-1} and decreases down to 11% at $\mu = 1000$cm^{2}V^{-1}s^{-1}. The off state is well defined when $\mu \gtrsim 5000$cm^{2}V^{-1}s^{-1}, which corresponds to the condition for $|t_G(E_{\rm res})| \geq |t_B|$. The $T_{\rm on}/T_{\rm off}$ is predicted to be 2.5 even for a low quality graphene of $\mu = 1000$cm^{2}V^{-1}s^{-1}.

5.6 Summary and Outlook

In summary, we propose a graphene based mid-infrared plasmonic waveguide modulator, which exhibits a sharp switching behavior coming from the Fano interference between the plasmon resonance in graphene and the background transmission. We point out that the resonant and the nonresonant contributions can almost entirely cancel each other, resulting in a vanishing off state transmission, by choosing right geometric parameters. Moreover, the active volume of the device, $V \sim 10^{-3}\lambda_0^3$, is much

smaller than the diffraction limit, making it ideal for on-chip integration. Further investigations with consideration of the electron-phonon interactions in graphene may expand the applicable frequencies over the graphene optical phonon energy (~ 0.2eV) even to the near-infrared telecommunication bands.

Chapter 6

Graphene Nano Cavities at Near-Infrared Frequencies

6.1 Introduction

The field of graphene plasmonics has drawn immense attention because it provides a way to shrink light by factor of 100 without too much propagation loss [17, 32, 41, 56, 103]. Recent experimental endeavours have confirmed the existence of graphene plasmons by acquiring their near field images using the scattering near field scanning optical microscopy (NSOM) [17, 32]. The plasmon resonances in graphene nano structures have also been extensively investigated [46, 99, 109]. Most of the current graphene plasmonics research have focused on mid-infrared frequency regime to suppress the electron-optical phonon interaction occurring at frequencies higher than $\omega_{\mathrm{Oph}} \approx 0.2\mathrm{eV}$.

In this chapter, we investigate the high energy characteristics of plasmon resonance in graphene nano cavities, and predict that the resonance is still observable at near infrared frequencies despite the coupling between electrons and optical phonons. As a simple yet instructive example, we start with discussing the plasmon resonances in graphene nanoribbons. The optical properties of graphene are investigated by taking into account the effect of the phonon interaction. We then theoretically demonstrate that the resonance frequency of a free standing bridge-shaped cavity with 5nm width and 10nm length can reach to the telecommunication bands ($\omega \sim 0.8\mathrm{eV}$) for suffi-

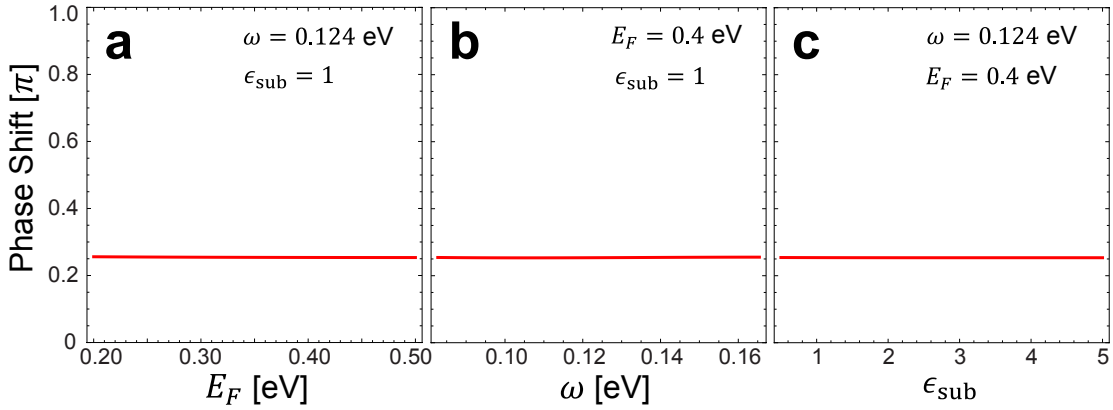

Figure 6.1: The phase shift of graphene plasmons upon reflection at the edges as functions of (a) the Fermi energy E_F, (b) the frequency ω, and (c) the substrate permittivity ϵ_{sub}. Note that the phase shift is approximately $\phi \approx 0.8$ and does not depend much on E_F, ω, or ϵ_{sub}.

ciently high Fermi energy ($E_F \sim 0.7$eV). The quality factor and the mode volume are calculated to be ~ 35 and $\sim 2\times10^{-8}\lambda_0^3$. Finally, we provide experimental evidences of plasmon resonance in graphene nanocavity arrays on SiO_2 using the Fourier transform infrared spectroscopy. In this system, the plasmons in graphene couple with substrate polar phonons to form surface plasmon phonon polaritons (SPPPs), observed in the extinction spectra around $\omega \sim 0.12$eV. Electron-optical phonon coupling in graphene broadens the plasmon resonances above ω_{Oph}.

6.2 Plasmon Resonance in Graphene Nanoribbons

Throughout this chapter, we use the finite element method (FEM) to numerically investigate the properties of graphene plasmon cavities. We model graphene as a thin film of the thickness δ, and impose the relative permittivity $\epsilon_G = 1 + i\sigma/\epsilon_0\omega\delta$, where σ is the complex optical conductivity of graphene [30], ω is the frequency, and the ϵ_0 is the free space permittivity. δ is chosen to be 0.1nm, which shows good convergence with respect to the $\delta \to 0$ limit.

The edges of graphene almost completely reflect incident graphene plasmons because of the high field confinement. The fraction of energy coupled to the unbound radiation is calculated to be much less then 1% for the confinement factor over 20,

which is typical for graphene plasmons. More interestingly, the phase shift ϕ upon reflection is approximately 0.8 and does not depend much on the Fermi level E_F, the permittivity of the substrate material ϵ_{sub}, or ω.

The m-th order resonance frequency ω_{res} of a graphene nanoribbon of width W is now readily obtained by the following phase-matching relation,

$$\beta(\omega_{\text{res}})\, W = m\pi - \phi \approx (m - 0.25)\pi, \tag{6.1}$$

where β is the propagation constant of the surface plasmon mode. As seen in Fig. 6.2(a), Eq. (6.1) well agrees with the full FEM simulation results. The fields are tightly confined near the graphene surface, and decay exponentially as a function of the distance from the surface. Figure 6.2(b) presents the dependence of ω_{res} on the width W of a free standing ribbon for various E_F. We note that ω_{res} can reach to the telecommunication band ($\sim$0.8eV) for narrow ribbons ($W \sim 5$nm) with a sufficient carrier densities ($E_F \sim 0.7$eV). The width of the plasmon resonance can be reasonably estimated from the resistive loss in graphene, because the system does not loose much energy as a form of radiation.

At this point, we also note that the quantum finite size effects could be important for very narrow ribbons. For example, a nanoribbon of $W = 5$nm is only $\sim$40 atoms across. In such small scale, the electronic edge states could substantially alter the properties of plasmon resonance. Reference [100] investigates graphene nano ribbons of various sizes using the tight binding model and concludes that the local electromagnetic (EM) theory corresponds well with the first principle calculation down to $W \sim 5$nm for ribbons with armchair edges. However, for nanoribbons with zigzag edges, the validity of the local EM calculation is limited when $W < 15$nm.

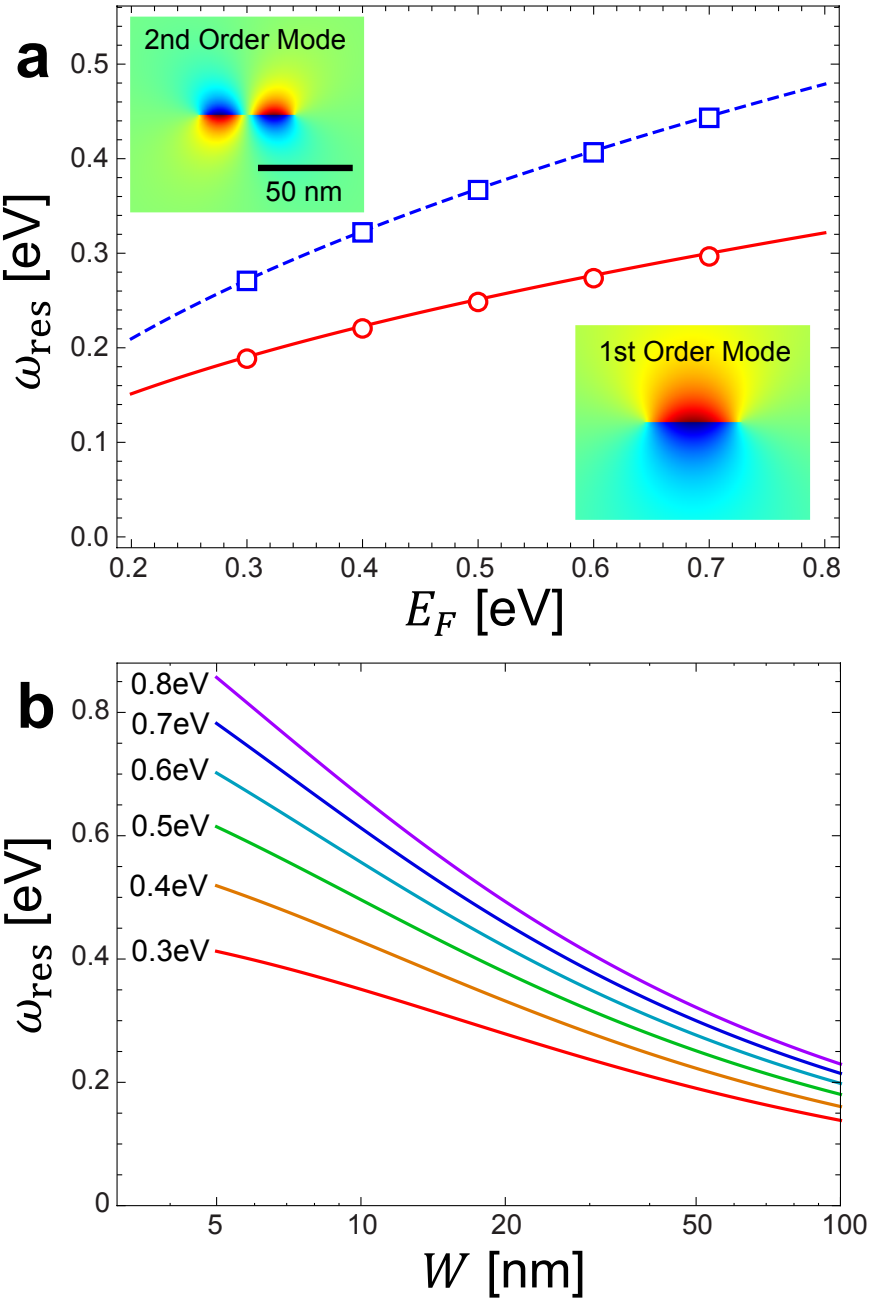

Figure 6.2: (a) The plasmon resonance frequency ω_{res} of a free standing graphene nanoribbon ($W = 50$nm) as a function of the Fermi energy E_F. The fundamental mode (red) and the second order mode (blue) are presented. The analytic calculation using Eq. (6.1) (lines) agrees well with the full FEM simulation result(circles and squares). The insets show the magnetic field profiles $\text{Re}\{H_y(x,z)\}$ of the resonances. (b) ω_{res} versus W for E_F =0.3–0.8eV.

6.3 Graphene Ultrasmall Cavities at Telecommunication Frequencies

6.3.1 Effect of Electron-Optical Phonon Interaction

When the energy of graphene plasmons are lower than the interband threshold, their losses are determined by the scattering rate Γ due to the intraband scattering processes. For sufficiently low frequencies $\omega < \omega_{\mathrm{Oph}} \approx 0.2\mathrm{eV}$, Γ is dominated by impurity scattering, and can be estimated from DC mobility μ_{DC}:

$$\Gamma_{\mathrm{imp}} = \frac{e\hbar v_F^2}{\mu_{\mathrm{DC}} E_F}. \tag{6.2}$$

On the other hand, electron-optical phonon interaction becomes a significant decay mechanism at $\omega > \omega_{\mathrm{Oph}}$ [41].

The intra-band contribution of the optical conductivity, which takes into account the effect of optical phonon coupling, is calculated from the electron self energy $\Sigma(\omega)$ using the following formula given in Ref. [1]

$$\sigma_{\mathrm{intra}}(\omega) = \frac{ie^2 E_F}{\pi\hbar\omega} \int d\omega' \frac{f(\omega') - f(\omega'+\omega)}{\omega - \Sigma(\omega'+\omega+i\eta) + \Sigma^*(\omega'+i\eta)}, \tag{6.3}$$

where $f(\omega)$ is the Fermi distribution function. To obtain Σ, we first assume the self energy is mainly originated from the impurity scattering and the electron-phonon coupling,

$$\mathrm{Im}\left\{\Sigma\right\} = \mathrm{Im}\left\{\Sigma_{\mathrm{Oph}}\right\} + \mathrm{Im}\left\{\Sigma_{\mathrm{imp}}\right\}. \tag{6.4}$$

$\mathrm{Im}\left\{\Sigma_{\mathrm{imp}}\right\}$ is naively approximated to be $-\Gamma_{\mathrm{imp}}/2$. The analytic expression for the imaginary part of Σ_{Oph} is adopted from Ref. [76],

$$\mathrm{Im}\left\{\Sigma_{\mathrm{Oph}}(\omega)\right\} = \begin{cases} -\alpha\left|\omega - \mathrm{sgn}(\omega)\omega_{\mathrm{Oph}} + E_F\right| & |\omega| \geq \omega_{\mathrm{Oph}}, \\ 0 & \text{otherwise}, \end{cases} \tag{6.5}$$

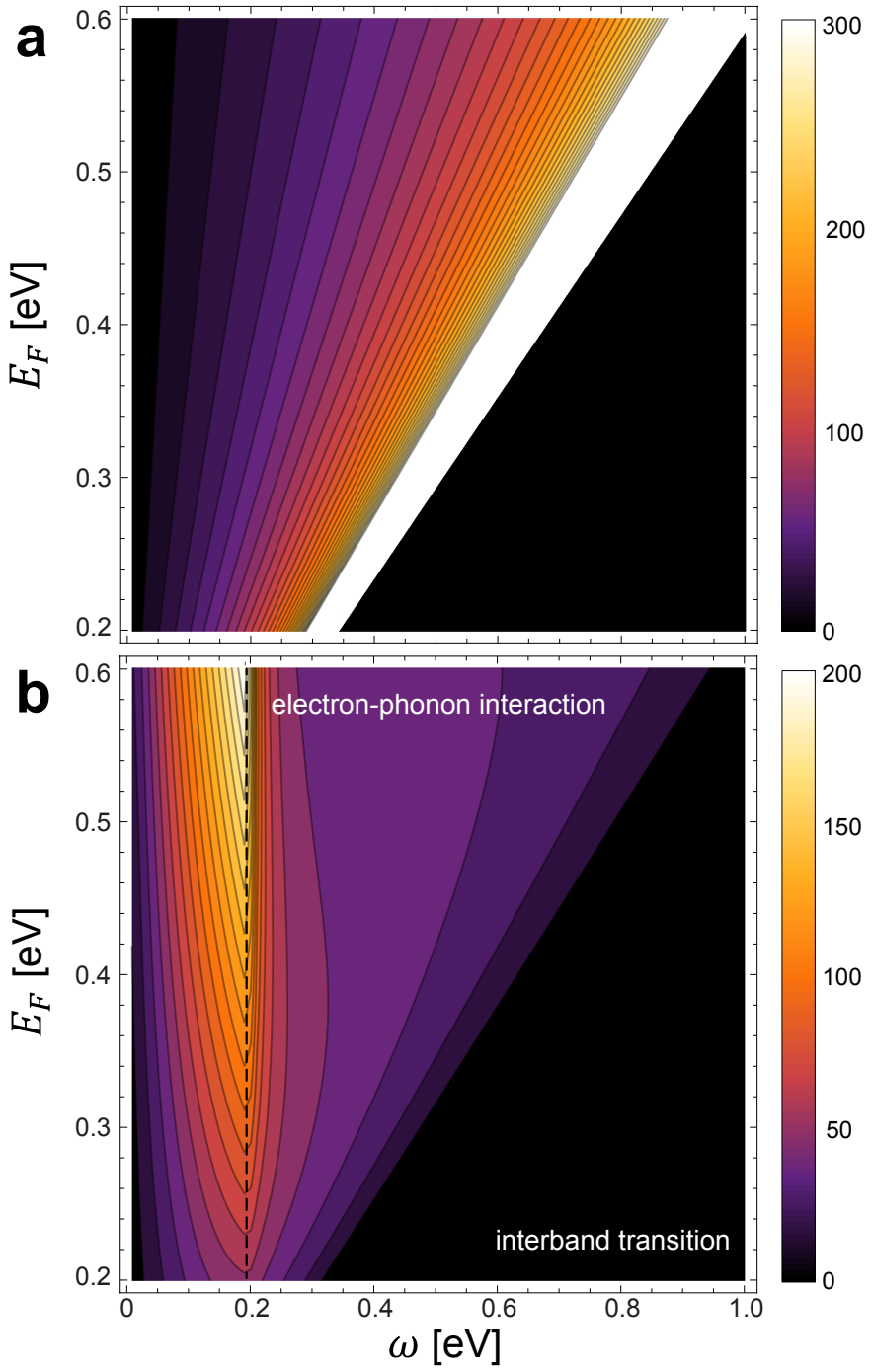

Figure 6.3: (a) The field localization $\mathrm{Re}\{\beta\}/k_0$ and (b) $\mathrm{Re}\{\beta\}/\mathrm{Im}\{\beta\}$ of plasmons in a free-standing graphene as functions of ω and E_F. $\mu_{\mathrm{DC}} = 10^4 \mathrm{cm}^2\mathrm{V}^{-1}\mathrm{s}^{-1}$ is assumed. Due to the electron-optical phonon interaction, the losses increase substantially as ω gets higher than $\omega_{\mathrm{Oph}} \approx 0.2\mathrm{eV}$. At $\omega \leq \omega_{\mathrm{Oph}}$, the optical loss in graphene is dominated by impurity scattering.

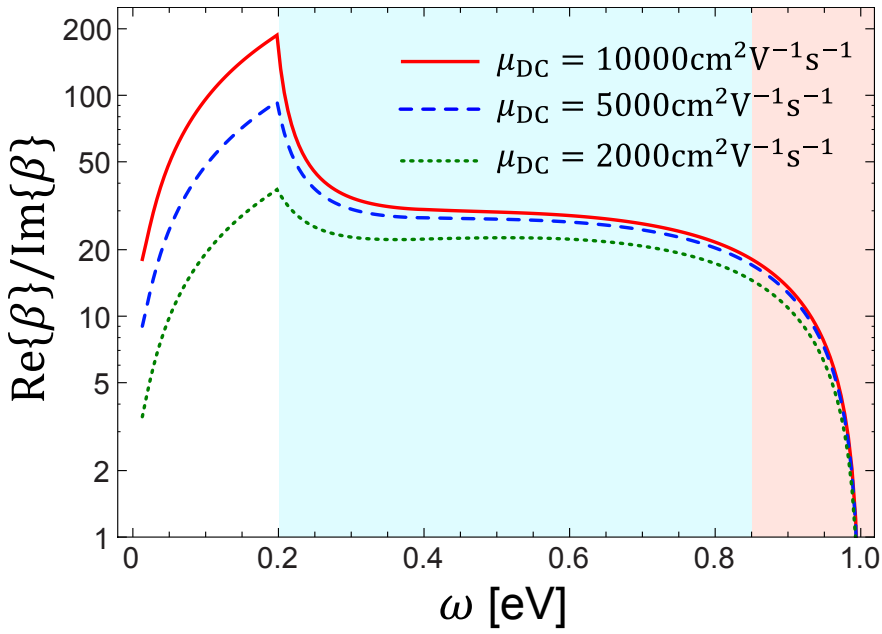

Figure 6.4: $\mathrm{Re}\{\beta\}/\mathrm{Im}\{\beta\}$ of plasmons in a free standing graphene at $E_F = 0.6$eV for $\mu_{\mathrm{DC}} = 2000$, 5000, and $10,000\mathrm{cm}^2\mathrm{V}^{-1}\mathrm{s}^{-1}$. The background colors indicate the mechanism governing losses: the impurity scattering (white), the optical phonon scattering (blue), and the interband transition (red)

with $\alpha = 1.83 \times 10^{-2}$. Here we ignore the angular dependence of the self energy, which is valid within 2.5eV from the Dirac point [76]. The real part of Σ is evaluated using the Kramers-Kronig relation,

$$\mathrm{Re}\left\{\Sigma_{\mathrm{Oph}}(\omega)\right\} = \frac{1}{\pi}\mathrm{PV}\int \frac{\mathrm{Im}\left\{\Sigma_{\mathrm{Oph}}(\omega')\right\}}{\omega' - \omega} d\omega'. \tag{6.6}$$

We verified that the resulting conductivity is almost unaffected by the choice of the cutoff energy for the integral in the range of 4–9eV. Throughout this section we neglect the effect of finite temperature. This is justifiable recognizing that the plasmon energy and the Fermi energy we are interested in are much higher than room temperature ~ 26meV. It would be also worth noting that the electron-phonon coupling strength at room temperature is not too much different from the low temperature value [101].

Figure 6.3 plots the field localization $\mathrm{Re}\{\beta\}/k_0$ and losses $\mathrm{Re}\{\beta\}/\mathrm{Im}\{\beta\}$ of plasmons in a free standing graphene as functions of ω and E_F. The propagation constant β is evaluated from Eq. (1.29). As anticipated, the losses increase substantially as ω

gets higher than ω_{Oph}. $\mathrm{Re}\{\beta\}/\mathrm{Im}\{\beta\}$ does not vary much for typical values of μ_{DC} (Fig. 6.4), indicating the electron-phonon interaction is more important loss mechanism than the impurity scattering in this regime.

6.3.2 Near-Infrared Nano Bridge Cavity

We note that the near-infrared frequency regime is accessible by raising E_F, which is directly proportional to the interband transition threshold. Even though the electron-phonon coupling makes graphene more lossy at $\omega > \omega_{\mathrm{Oph}}$, the propagation length $L_p/\lambda_p = \mathrm{Re}\{\beta\}/2\pi\mathrm{Im}\{\beta\}$ of ~ 4 could be good enough for certain applications (Fig. 6.4). In this section, as an example, we investigate a near-infrared graphene-based plasmonic cavity, whose resonance frequency can be tuned up to the telecommunication bands ~ 0.8eV.

Here we consider the plasmon resonances of a bridge shaped graphene suspended in the free space as illustrated in Fig. 6.5(a). The width and the length of the bridge is chosen to be 5 and 10 nm respectively. When the Fermi level of the nanobridge cavity is 0.6eV, the system exhibits the fundamental plasmon resonance at $\omega = 0.70$eV, close to the telecommunication band. The quality factor Q of the resonance is calculated to be 38, which means that the resonator loses half of the stored energy in approximately 4 cycles. The fields are tightly confined near the bridge as depicted in Fig. 6.5 (c) and (d). The high field confinement results in an extremely small mode volume,

$$V_{\mathrm{eff}} = \frac{\int \epsilon \mathbf{E}^2 dV}{\epsilon \mathbf{E}^2(x = y = 0, z \to +0)} = 1.83 \times 10^{-8} \lambda_0^3, \tag{6.7}$$

which has never been achieved previously. The high local density of optical states near the cavity leads to a large spontaneous emission enhancement (Purcell factor of $F_P = 1.7 \times 10^8$) [82].

We also note that the resonance frequency can reach and even exceed the telecommunication band by compromising the quality factor (Fig. 6.5(b)). ω_{res} of the fundamental resonance coincides with the telecommunication frequency at $E_F \approx 0.7$eV. The higher-order resonances also offer a way to access to higher frequencies. Fig-

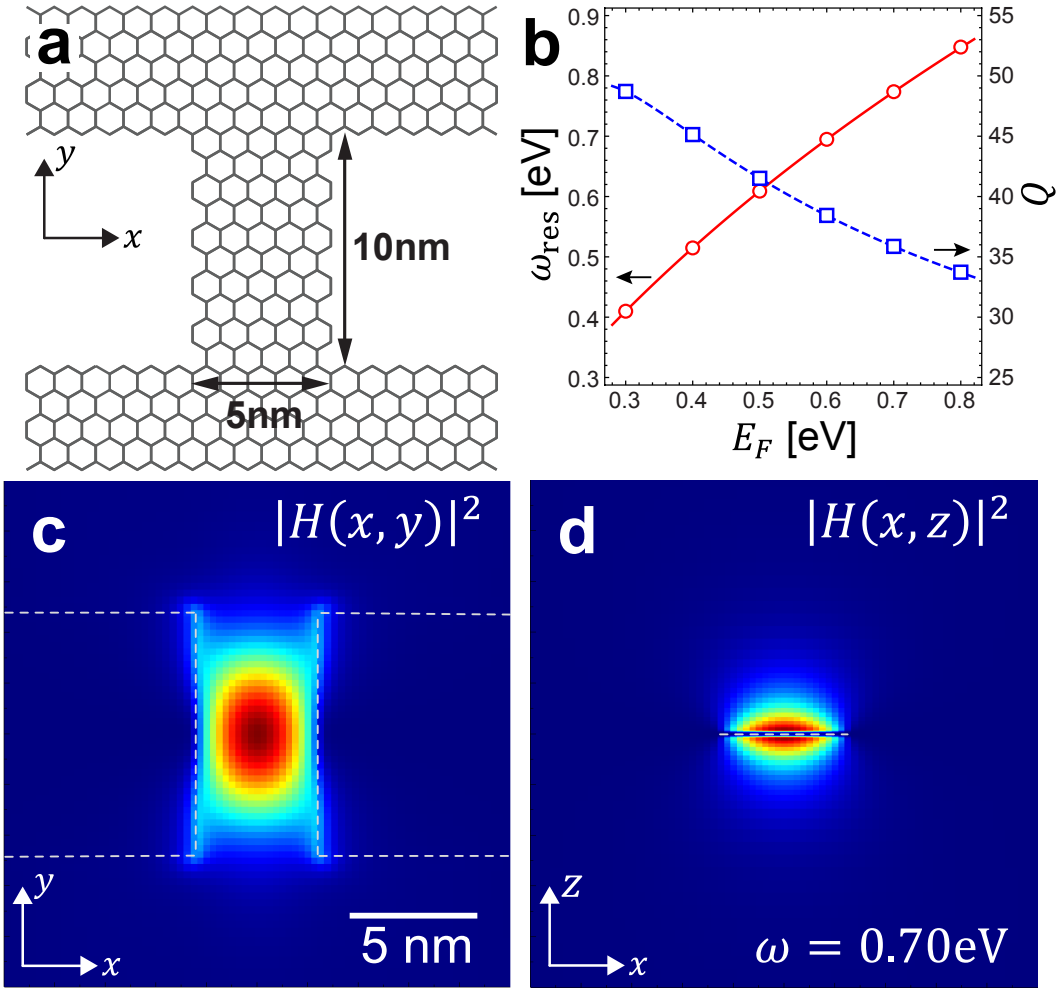

Figure 6.5: (a) Schematic of a graphene nanobridge cavity. (b) The resonance frequency ω_{res} (red solid) and the quality factor Q (blue dashed) of the fundamental plasmon resonance as a function of E_F. (c) The top view ($z0 = +0$ plane) and (d) the side view ($y = 0$ plane) of the magnetic field intensity distribution of the fundamental mode at $E_F = 0.6$eV. $\mu_{\mathrm{DC}} = 10,000\mathrm{cm}^2\mathrm{V}^{-1}\mathrm{s}^{-1}$ is assumed.

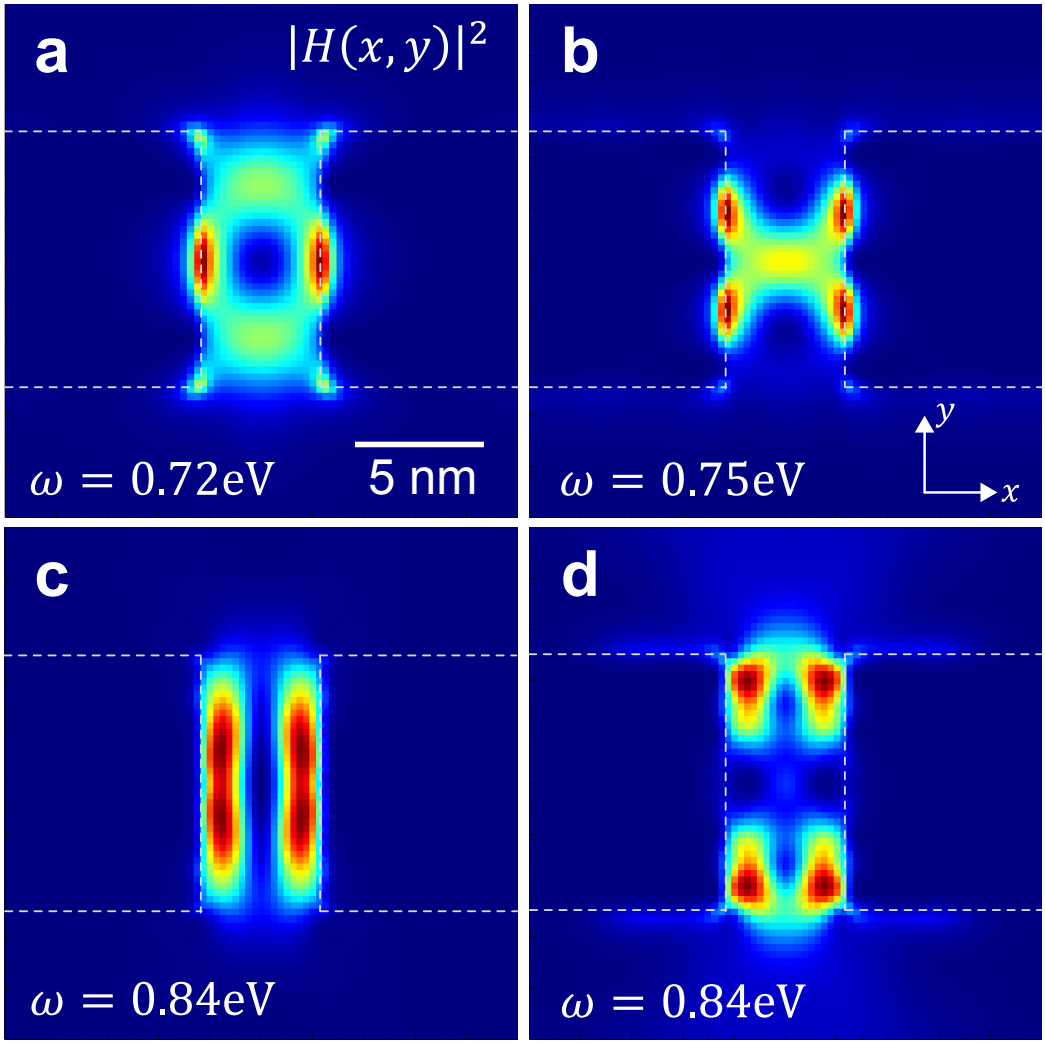

Figure 6.6: The magnetic field intensity profiles of the higher plasmon resonances. $E_F = 0.6$eV and $\mu_{\mathrm{DC}} = 10,000\mathrm{cm}^2\mathrm{V}^{-1}\mathrm{s}^{-1}$ are assumed.

ure 6.6 shows the magnetic field profiles and the resonance frequencies of some of the higher order modes at $E_F = 0.6$eV.

As pointed out earlier, the quantum finite size effect could play an important role in such small scale, and thus the actual frequency and the width of the resonance could deviate from the local electromagnetic calculation depending on the edge termination [100]. First principle calculations using the density functional theory may offer a more accurate estimate of the plasmon resonance properties.

6.4 Graphene Resonator Arrays on SiO_2

Although the extinction cross section of a graphene nanocavity could be an order of magnitude larger than its geometrical area [99], it is still challenging to detect the resonance of a single cavity in far-field measurements. Alternatively, one can fabricate an array of resonators to amplify the intensity of the signal. Current state-of-the art nanofabrication technology, combined with large-area synthesis of graphene using chemical vapor deposition [57], enables us to pattern graphene into arrays of over a million nanocavities. In this section, we experimentally investigate the properties of plasmon resonance in graphene nanocavity arrays on SiO_2.

6.4.1 Sample Preparation and Measurement Methods

We grew graphene on Cu foils by chemical vapor deposition (CVD)[57]. The graphene was transferred onto SiO_2(285nm)/Si substrates with the aid of polymethyl methacrylate (PMMA) [48, 57]. The quality of the graphene was characterized by Raman spectroscopy (Fig. 6.8 (a)). Cr/Au electrodes were deposited on top of the graphene surface by thermal evaporation. We then fabricated graphene resonator arrays using standard e-beam lithography followed by oxygen plasma etch. Instead of ribbon arrays, we adopt rectangular grid patterns of a high aspect ratio of ~ 5 to prevent resist pattern collapse during the development process. The size of the arrays is 50μm by 50μm. The width (W) and the pitch (L) of the fabricated resonator patterns were later determined by the atomic force microscope (Fig. 6.7).

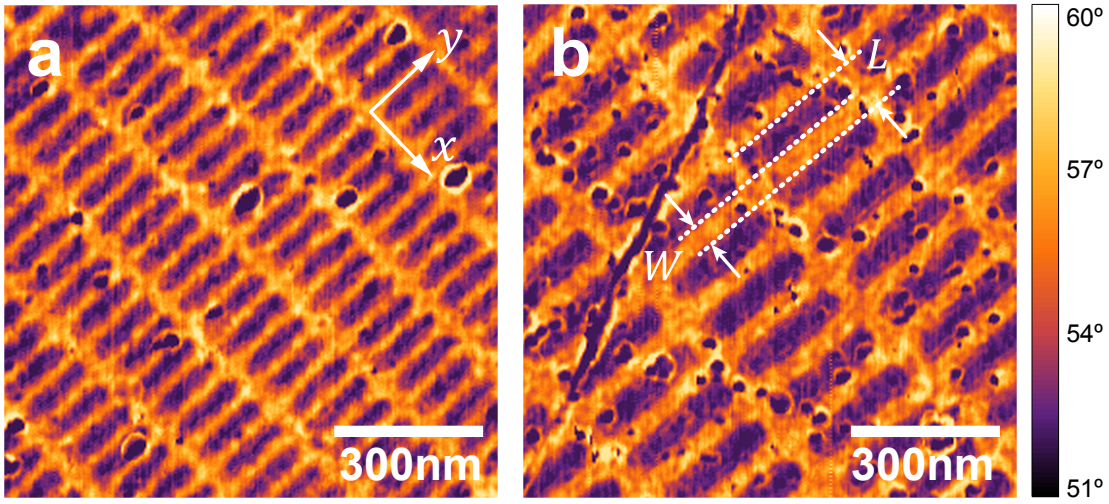

Figure 6.7: The atomic force microscope (AFM) phase images of graphene nanocavity arrays. (a) $(W, L) = (27, 60)$nm and (b) $(W, L) = (50, 100)$nm. Yellow color indicates the region covered by graphene.

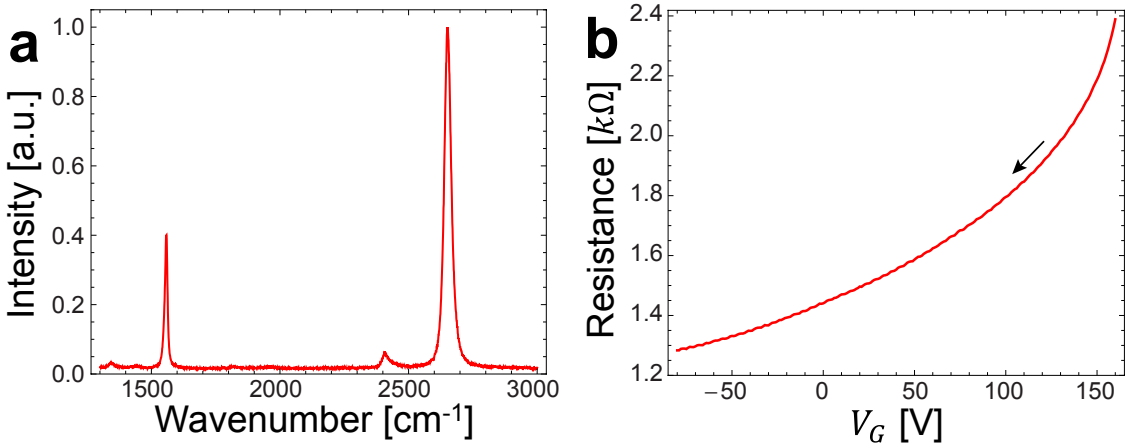

Figure 6.8: (a) The Raman spectrum and (b) the electrical transport measurement of graphene on SiO_2/Si substrate. The resistance between the two electrodes closest to the resonator arrays is plotted as a function of the gate voltage V_G. V_G was swept from 160V to -80V with a rate of 0.2V/s.

The Fermi energy E_F of the sample was tuned by electrostatic gating. Figure 6.8 (b) plots the low frequency (16Hz) resistance between the two electrodes closest to the resonator arrays as a function of the back gate voltage V_G. V_G was swept from 160 to -80V with a rate of 0.2V/s. As prepared, the sample is heavily p-doped. From the electrical transport measurement, the charge neutral point is estimated to be at $V_{\mathrm{CNP}} \approx 180$V. The capacitance between the graphene and the Si back gate is estimated from the thickness ($d = 285$nm) and the dielectric constant ($\epsilon_{\mathrm{sub}} = 3.9$) of the oxide layer, $C_g = \epsilon_{\mathrm{sub}}\epsilon_0/d \approx 12\mathrm{nF/cm}^2$.

To measure the transmission spectra of the graphene resonator arrays, we used a Fourier transformation infrared (FTIR) spectrometer [38] attached to an infrared (IR) microscope. The infrared light emitted from the globar source in the FTIR spectrometer was polarized by the CaF_2 wire grid polarizer, and then was illuminated on and collected from the cavity array area with an aid of IR microscope. The size of the illumination spot was approximately same as the size of the arrays ($\sim 50\mu$m by 50μm). IR transmission spectra from 900 to 3000cm^{-1} were taken at $V_G = 150$, 120, 100, 70, 40, 0, -40, and -80V with the resolution of 3.9cm^{-1}. The spectra were then normalized such that $1 - T/T_0$, where T_0 is the spectrum measured at $V_G = 150$V, closest to the charge neutral point.

6.4.2 Result and Discussion

Figure 6.9 shows the extinction spectra of the $(W, L) = (50, 100)$nm cavity array for polarizations perpendicular (**E** along the x direction, red) and parallel (**E** along the y direction, blue) to the ribbons at $V_G = 80$V. As theoretically predicted, only the perpendicularly polarized light exhibits the peaks around 1000 and 1500cm^{-1} (0.125 and 0.185eV), which are associated with the plasmon resonances. The high energy peak blue-shifts as the carrier density increases by lowering V_G. The position of the low energy peak is much less dependent on V_G (Fig. 6.10).

The multiple resonance peaks are originated from coupling between the graphene plasmons and the substrate phonons. SiO_2 is known to have the vibrational modes

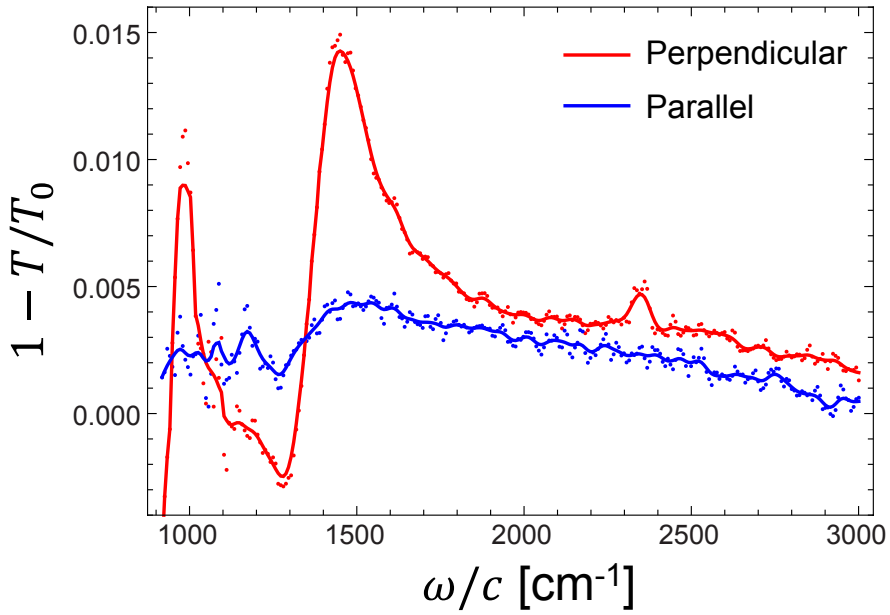

Figure 6.9: The normalized extinction spectra of the $(W, L) = (50, 100)$nm cavity array for polarizations perpendicular (**E** along the x direction, red) and parallel (**E** along the y direction, blue) to the ribbons at $V_G = 80$V. The markers are the raw data and the solid lines are the smoothed spectra. Only the perpendicularly polarized light exhibits the resonance peaks.

around 0.13eV, which alter its dielectric response substantially, as shown in Fig. 6.11 (a) [75]. As a consequence, SiO_2 supports surface phonon polaritons around that frequency. Plasmons in graphene couple with these quasiparticles to form surface plasmon phonon polaritons (SPPPs). The dispersion relation of graphene on SiO_2 is obtained from Eq. (1.29) and plotted in Fig. 6.11 (b) and 6.12 (a). The dotted and the dashed lines indicate the wavenumbers at which the ribbon arrays of $W = 50$nm and $W = 25$nm are in the fundamental resonance. We note that the resonance condition meets at three different frequencies. The lowest and the highest resonances are associated with the SPPPs and the graphene plasmons respectively. The middle resonance is hardly observable because the losses are too high (Fig. 6.11 (b)). As the cavity becomes narrower (i.e., W becomes smaller), the SPPP resonance also gradually disappears. Note that the low frequency peaks in the extinction spectra are less pronounced for the $W = 27$nm cavity array (Fig. 6.10).

Figure 6.12 (b) shows the correspondence between the resonance frequencies $\omega_{\rm res}$

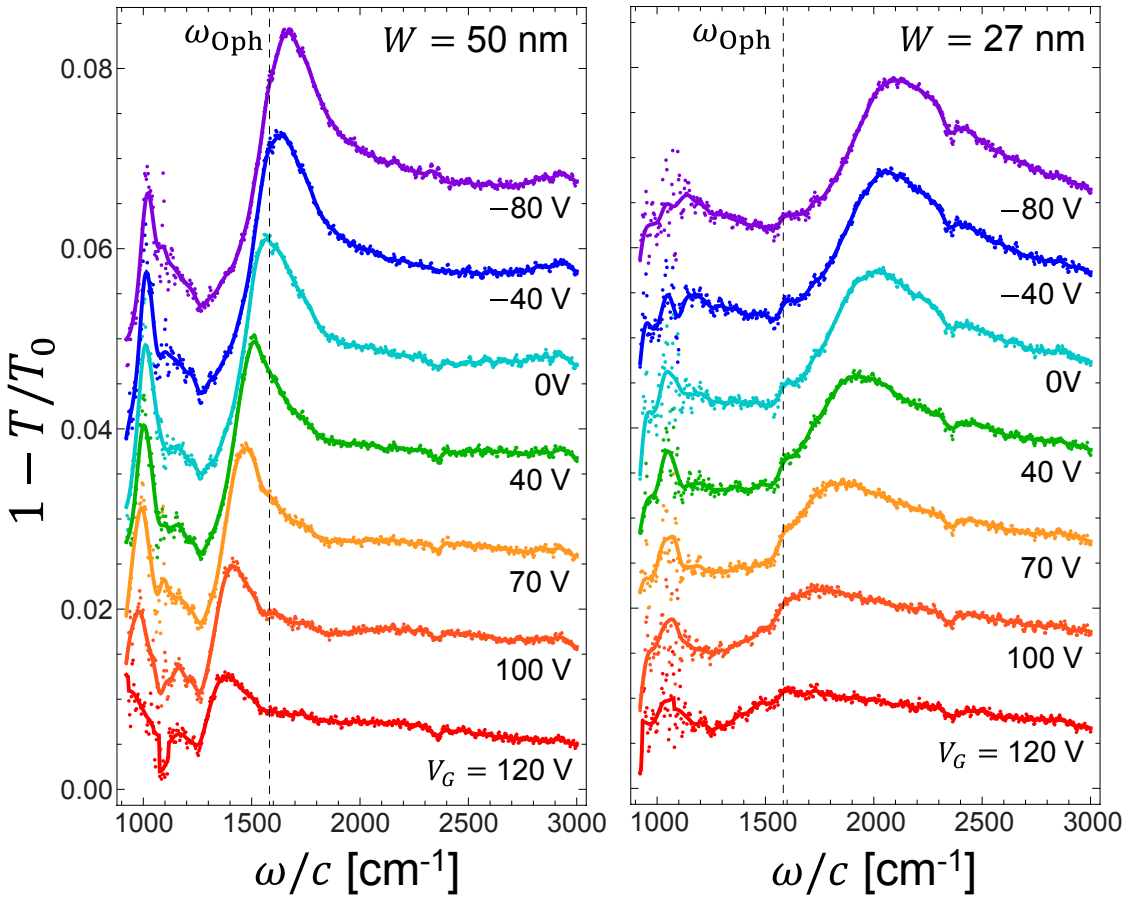

Figure 6.10: The normalized extinction spectra of the $(W, L) = (50, 100)$nm and $(W, L) = (27, 60)$nm cavity arrays for the perpendicular polarization at $V_G = 120$, 100, 70, 40, 0, -40, and -80V. The dashed lines indicate the graphene optical phonon frequency. The spectra are offset for clarity.

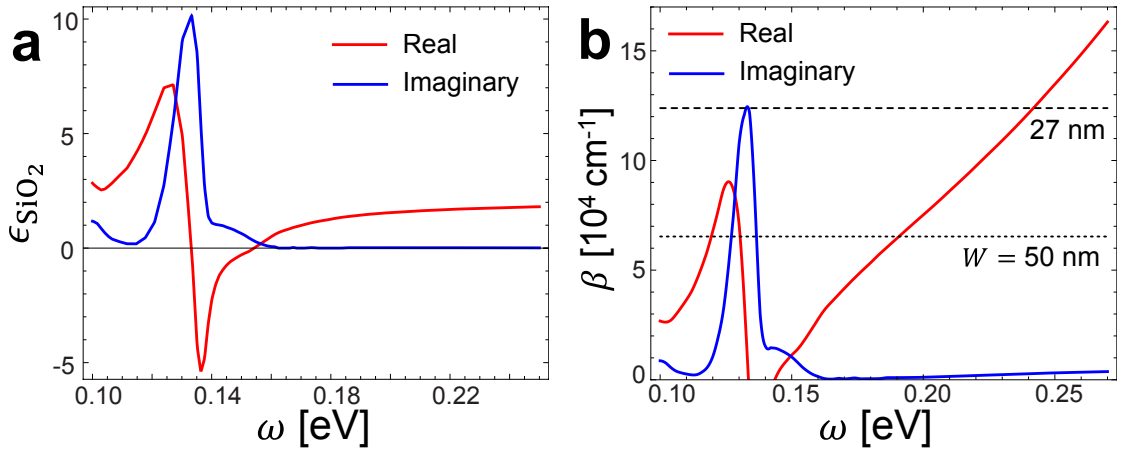

Figure 6.11: (a) The relative permittivity of SiO_2 changes abruptly around $\omega \sim 0.13$eV due to phonon interaction [75]. (b) The dispersion relation of the plasmons in graphene on SiO_2 at $|E_F| = 0.4$eV. The dotted line and the dashed line respectively indicate β associated with $W = 50$nm and $W = 27$nm ribbons. Plasmon-phonon coupling results in multiple resonance modes.

extracted from the extinction spectra and the theoretical prediction. Assuming the carrier density n in the patterned area is not too much different from that in surrounding unpatterned region ($C_g|V_G - V_{\mathrm{CNP}}|/e$), the Fermi energy is determined from the following relation,

$$E_F = \mathrm{sgn}\{V_G - V_{\mathrm{CNP}}\} v_F \hbar \sqrt{\frac{\pi C_g |V_G - V_{\mathrm{CNP}}|}{e}}, \tag{6.8}$$

where $v_F \approx 10^8$cm/s is the Fermi velocity, $C_g \approx 12$nF/cm^2. $V_{\mathrm{CNP}} \approx 180$V is estimated from the electrical transport measurement.

The plasmon resonance becomes broader as it crosses over the graphene optical phonon energy ω_{Oph} (see the $W = 50$nm spectra in Fig. 6.10). We also note that the extinction spectra of the $W = 27$nm ribbons exhibit a slight kink at $\omega = \omega_{\mathrm{Oph}}$, which is likely originated from the electron-phonon coupling in graphene.

The quality factors of the resonances are evaluated from the width of the extinction peaks. The plasmon resonances in the $W = 27$nm and the $W = 50$nm cavity arrays, and the SPPP resonance in the $W = 50$nm ribbons respectively have Q of ~ 4, ~ 6, and ~ 15 at $V_G = -80$V ($E_F = -0.51$eV). The broadening is caused not only by the

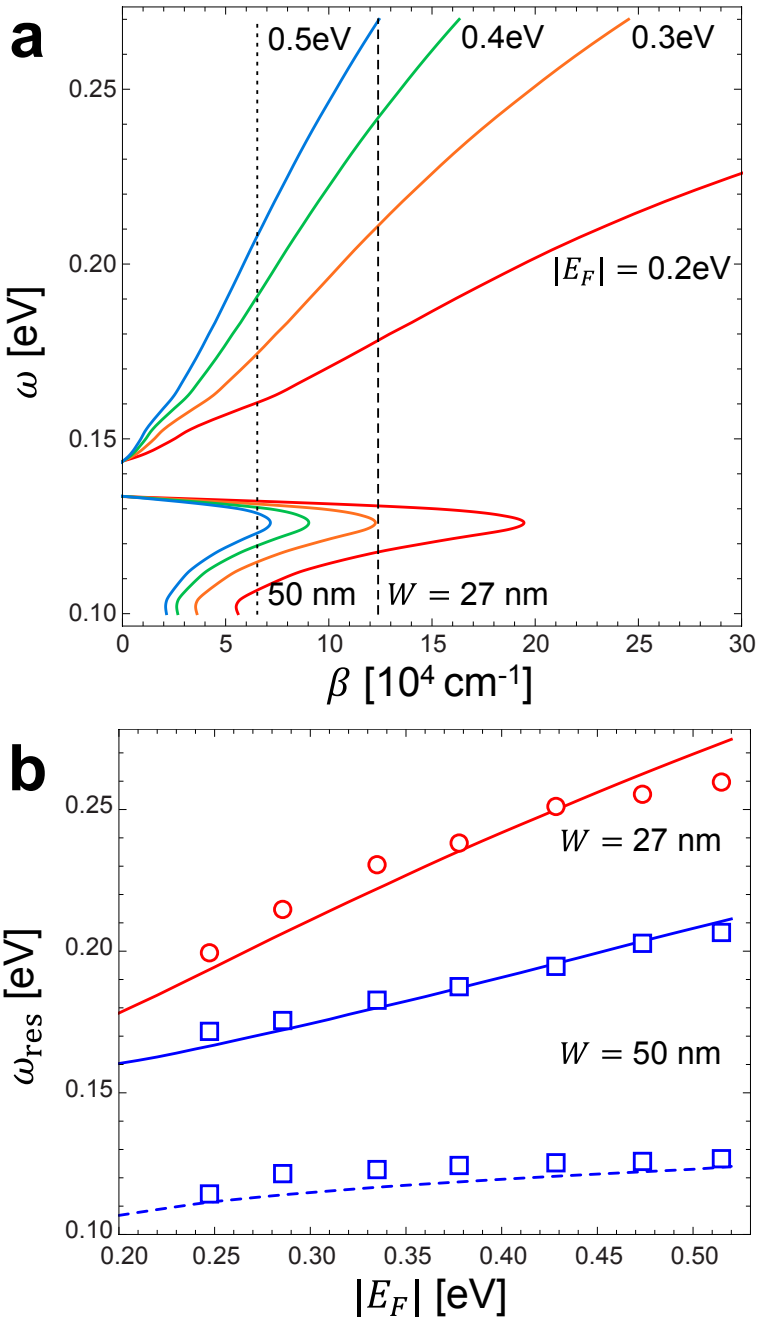

Figure 6.12: (a) The dispersion relation of surface phonon plasmon polaritons in graphene on SiO_2 substrate at $|E_F| = 0.2$, 0.3, 0.4, and 0.5eV. The dotted line and the dashed line respectively indicate β associated with $W = 50$nm and $W = 27$nm ribbons. (b) The resonance frequencies ω_{res} of $(W, L) = (27, 50)$nm (red) and $(W, L) = (50, 100)$nm (blue) cavity arrays. The experimental data (symbols) well agrees with the theory (curves).

finite life time of the quasi particles but also by the ensemble averaging effect. At this point, it is difficult to discriminate between these effects.

6.5 Summary and Outlook

In summary, we experimentally investigate the properties of plasmon resonance in graphene nanocavity arrays on SiO_2 using the FTIR spectroscopy. The system exhibits multiple resonance peaks originated from the coupling with surface phonons in SiO_2 substrate. By changing the size and the Fermi energy of the ribbon arrays, the plasmon resonance frequency ω_{res} was tuned from 0.16 to 0.26eV. The width of the resonance becomes broader due to the electron-optical phonon coupling as ω_{res} crossing over ω_{Oph}.

We also point out that the resonance frequency can be further increased and even reach to the telecommunication bands ($\omega \sim 0.8$eV) by raising E_F and decreasing the size of the cavity sufficiently. The standard electrostatic gating scheme is limited by the oxide breakdown [20], and thus not suitable for E_F over 0.6eV. As an alternative, ion-gel gating offers a way to achieve high E_F even up to 1eV without sacrificing tunability [46, 49]. The state-of-the-art electron beam lithography may facilitate to fabricate graphene nanocavities as small as a few nanometers. In such small scale, the quantum finite size effects could substantially alter the properties of plasmon resonance, which will be addressed in the future.

Bibliography

[1] P. B. Allen, arXiv:cond-mat/0407777 (2004).

[2] N. W. Ashcroft and N. D. Mermin, *Solid State Physics* (Brooks- Cole, Belmont, MA, 1976).

[3] P. Avouris, Nano Lett. **10**, 4285 (2010).

[4] J. W. Bai, X. Zhong, S. Jiang, Y. Huang and X. F. Duan, Nat. Nanotechnol. **5**, 190 (2010).

[5] A. A. Balandin, S. Ghosh, W. Z. Bao, I. Calizo, D. Teweldebrhan, F. Miao and C. N. Lau, Nano Lett. **8**, 902 (2008).

[6] R. Balog, B. Jorgensen, L. Nilsson, M. Andersen, E. Rienks, M. Bianchi, M. Fanetti, E. Laegsgaard, A. Baraldi, S. Lizzit, Z. Sljivancanin, F. Besenbacher, B. Hammer, T. G. Pedersen, P. Hofmann and L. Hornekaer, Nat. Mater. **9**, 315 (2010).

[7] C. W. J. Beenakker, R. A. Sepkhanov, A. R. Akhmerov, and J. Tworzydlo, Phys. Rev. Lett. **102**, 146804 (2009).

[8] P.R. Berman, Phys. Rev. E **66**, 067603 (2002).

[9] K. I. Bolotin, K. J. Sikes, J. Hone, H. L. Stormer, and P. Kim, Phys. Rev. Lett. **101**, 096802 (2008).

[10] K. I. Bolotin, K.J. Sikes, Z. Jiang, M. Klima, G. Fudenberg, J. Honec, P. Kim, and H.L. Stormer, Solid State Commun. **146**, 351 (2008).

[11] M. Born and E. Wolf, *Principles of Optics*, 7th ed. (Cambridge University Press, 1999).

[12] S. P. Burgos, R. de Waele, A. Polman, and H. A. Atwater, Nature Mater. **9**, 407 (2010).

[13] A. H. Castro Neto, F. Guinea, N. M. R. Peres, K. S. Novoselov, and A. K. Geim, Rev. Mod. Phys. **81**, 109 (2009).

[14] V. V. Cheianov and V. I. Fal'ko, Phys. Rev. B **74**, 041403 (2006).

[15] V. V. Cheianov, V. Fal'ko, and B. L. Altshuler, Science **315**, 1252 (2007).

[16] Z. H. Chen, Y. M. Lin, M. J. Rooks and P. Avouris, Physica E **40**, 228 (2007).

[17] J. Chen, M. Badioli, P. Alonso-Gonzlez, S. Thongrattanasiri, F. Huth, J. Osmond, M. Spasenovic, A. Centeno, A. Pesquera, P. Godignon, A. Zurutuza, N. Camara, F. J. Garcia de Abajo, R. Hillenbrand, F. Koppens, arXiv:1202.4996v2 (2012)

[18] C. Coletti,C. Riedl, D. S. Lee, B. Krauss, L. Patthey, K. von Klitzing, J. H. Smet, and U. Starke, Phys. Rev. B **81**, 235401 (2010)

[19] S. Datta, *Electronic Transport in Mesoscopic Systems* (Cambridge University Press, 1995).

[20] B. E. Deal, J. Electrochem. Soc. **110**, 527 (1963).

[21] C. R. Dean, A. F. Young, I. Meric, C. Lee, L. Wang, S. Sorgenfrei, K. Watanabe, T. Taniguchi, P. Kim, K. L. Shepard and J. Hone, Nat. Nanotechnol. **5**, 722 (2010).

[22] A. De Martino, L. Dell'Anna and R. Egger, Phys. Rev. Lett. **98**, 066802 (2007).

[23] J. A. Dionne, L. Sweatlock, H. A. Atwater, and A. Polman, Phys. Rev. B **73**, 035407 (2006).

[24] J. A. Dionne, E. Verhagen, A. Polman, and H. A. Atwater, Opt. Express **16**, 19001 (2008).

[25] P. Drude, Ann. Phys. (Berlin) **1**, 566 (1900).

[26] X. Du, I. Skachko, A. Barker, and E. Y. Andrei, Nat. Nanotechnol. **3**, 491 (2008).

[27] D. C. Elias, R. R. Nair, T. M. G. Mohiuddin, S. V. Morozov, P. Blake, M. P. Halsall, A. C. Ferrari, D. W. Boukhvalov, M. I. Katsnelson, A. K. Geim and K. S. Novoselov, Science **323**, 610 (2009).

[28] S. Enoch, G. Tayeb, P. Sabouroux, N. Gurin, and P. Vincent, Phys. Rev. Lett. **89**, 213902 (2002).

[29] U. Fano, Phys. Rev. **124**, 1866 (1961).

[30] L. A. Falkovsky and A. A. Varlamov, Eur. Phys. J. B **56**, 281 (2007).

[31] L. A. Falkovsky, J. Phys.: Conf. Ser. **129**, 012004 (2008).

[32] Z. Fei, A. S. Rodin, G. O. Andreev, W. Bao, A. S. McLeod, M. Wagner, L. M. Zhang, Z. Zhao, G. Dominguez, M. Thiemens, M. M. Fogler, A. H. Castro-Neto, C. N. Lau, F. Keilmann, D. N. Basov, arXiv:1202.4993v2 (2012).

[33] I. W. Frank, D. M. Tanenbaum, A. M. Van der Zande, and P. L. McEuen, J. Vac. Sci. Technol. B **25**, 2558 (2007).

[34] H. Gersen, T. J. Karle, R. J. P. Engelen, W. Bogaerts, J. P. Korterik, N. F. van Hulst, T. F. Krauss, and L. Kuipers, Phys. Rev Lett. **94**, 073903 (2005).

[35] S. Ghosh and M. Sharma, J. Phys. Condens. Matter **21**, 292204 (2009).

[36] R. Golizadeh-Mojarad and S. Datta, Phys. Rev. B **75**, 081301(R) (2007)

[37] F. Goos and H. Hänchen, Ann. Phys. (Leipzig) **1**, 333 (1947).

[38] P. R. Griffiths, and J. A. de Haseth, *Fourier Transform Infrared Spectrometry* (Wiley, New York, 1986).

[39] M. Y. Han, B. Ozyilmaz, Y. B. Zhang and P. Kim, Phys. Rev. Lett. **98**, 206805 (2007).

[40] J. He, Y. Jin, Z. Hong and S. He, Opt. Express **16**, 11077 (2008).

[41] M. Jablan,H. Buljan,and M. Soljacic, Phys. Rev. B **80**, 245435 (2009).

[42] M. S. Jang, H. Kim, H. A. Atwater, and W. A. Goddard, Appl. Phys. Lett. **97**, 043504 (2010).

[43] M. S. Jang and H. A. Atwater, Phys. Rev. Lett. **107**, 207401 (2011).

[44] T. Jiang, J. Zhao and Y. Feng, Opt. Express **17**, 170 (2009).

[45] P. B. Johnson and R. W. Christy, Phys. Rev. B **6**, 4370 (1972).

[46] L. Ju, B. Geng, J. Horng, C. Girit, M. Martin, Z. Hao, H. A. Bechtel, X. Liang, A. Zettl, Y. R. Shen and F. Wang, Nat. Nanotechnol. **6**, 630 (2011).

[47] M. I. Katsnelson, K. S. Novoselov, and A. K. Geim, Nat. Phys. **2**, 620 (2006).

[48] K. S. Kim, Y. Zhao, H. Jang, S. Y. Lee, J. M. Kim, K. S. Kim, J. H. Ahn, P. Kim, J. Y. Choi, B. H. Hong, Nature **457**, 706 (2009). 710.

[49] B. J. Kim, H. Jang, S. K. Lee, B. H. Hong, J. H. Ahn, and J. H. Cho, Nano Lett. **10**, 3464 (2010).

[50] H. Kim, M. S. Jang, H. A. Atwater, and W. A. Goddard, in *Handbook of Nanoscience, Engineering, and Technology*, 3rd ed., edited by W. A. Goddard, D. Brenner, S. E. Lyshevski, and G. J. Iafrate (CRC Press, 2012).

[51] O. Klein, Z. Phys. A: Hadrons and Nucl. **53**, 157 (1929).

[52] A. F. Koenderink, and A. Polman, Phys. Rev. B **74**, 033402 (2006).

[53] J. B. Kogut, Rev. Mod. Phys **55**, 775 (1983).

[54] A. B. Kuzmenko, E. van Heumen, F. Carbone, and D. van der Marel, Phys. Rev. Lett. **100**, 117401 (2008).

[55] H. J. Lezec, J. A. Dionne, H. A. Atwater, Science **316**, 430 (2007).

[56] Z.Q. Li, E.A. Henriksen, Z. Jiang, Z. Hao, M.C. Martin, P. Kim, H.L. Stormer, and D.N. Basov, Nature Phys. **4**, 532 (2008)

[57] X. Li, W. Cai, J. An, S. Kim, J. Nah, D. Yang, R. Piner, A. Velamakanni, I. Jung, E. Tutuc, S. K. Banerjee, L. Colombo, R. S. Ruoff, Science **324**, 1312 (2009).

[58] L. Liao, Y. Lin, M. Bao, R. Cheng, J. Bai,Y. Liu, Y. Qu, K. L. Wang, Y. Huang, and X. Duan, Nature **467**, 305 (2010).

[59] C. Liu, Z. Dutton, C. H. Behroozi, and L. V. Hau, Nature (London) **409**, 490 (2001).

[60] M. Liu, X. Yin, E. Ulin-Avila, B. Geng, T. Zentgraf, L. Ju, F. Wang, and X. Zhang, Nature **474**, 64 (2011)

[61] B. Luk'yanchuk, N. I. Zheludev, S. A. Maier, N. J. Halas, P. Nordlander, H. Giessen and C. T. Chong, Nat. Mater. **9**, 707 (2010).

[62] Y. H. Lu, R. Q. Wu, L. Shen, M. Yang, Z. D. Sha, Y. Q. Cai, P. M. He and Y. P. Feng, Appl. Phys. Lett. **94**, 122111 (2009).

[63] W. T. Lu, Y. J. Huang, B. D. F. Casse, R. K. Banyal, and S. Sridhar, Appl. Phys. Lett. **96**, 211112 (2010).

[64] S. A. Maier, P. G. Kik, H. A. Atwater, S. Meltzer, E. Harel, B. E. Koel, and A. A. G. Requicha, Nature Mater. **2**, 229 (2003).

[65] S. A. Maier, *Plasmonics: Fundamentals and Applications* (Springer, New York, 2007).

[66] A. S. Mayorov, R. V. Gorbachev, S. V. Morozov, L. Britnell, R. Jalil, L. A. Ponomarenko, P. Blake, K. S. Novoselov, K. Watanabe, T. Taniguchi and A. K. Geim, Nano Lett. **11**, 2396 (2011).

[67] I. Meric, M. Y. Han, A. F. Young, B. Ozyilmaz, P. Kim and K. L. Shepard, Nat. Nanotechnol. **3**, 654 (2008).

[68] S. A. Mikhailov, and K. Ziegler, Phys. Rev. Lett. **99**, 016803 (2007).

[69] B. Min, E. Ostby, V. Sorger, E. U. Avila, L. Yang, X. Zhang, and K. Vahala, Nature (London) **457**, 455 (2009).

[70] A. E. Miroshnichenko, S. Flach, and Y. S. Kivshar, Rev. Mod. Phys. **82**, 2257 (2010).

[71] H. T. Miyazaki, Y. Kurokawa, Phys. Rev. Lett. **96**, 097401 (2006).

[72] L. W. Molenkamp, A. A. M. Staring, C. W. J. Beenakker, R. Eppenga, C. E. Timmering, , J. G. Williamson, C. J. P. M. Harmans, and C. T. Foxon, Phys. Rev. B **41**, 1274 (1990).

[73] R. Murali, Y. X. Yang, K. Brenner, T. Beck and J. D. Meindl, Appl. Phys. Lett. **94**, 243114 (2009).

[74] K. S. Novoselov, A. K. Geim, S. V. Morozov, D. Jiang, Y. Zhang, S. V. Dubonos, I. V. Grigorieva, and A. A. Firsov, Science **306**, 666 (2004).

[75] E. D. Palik, *Handbook of Optical Constants of Solids* (Academic, 1985).

[76] C. H. Park, F. Giustino, M. L. Cohen, and S. G. Louie, Phys. Rev. Lett. **99**, 086804 (2007).

[77] C. H. Park, Y. W. Son, L. Yang, M. L. Cohen and S. G. Louie, Nano Lett. **8**, 2920 (2008).

[78] S. Park and R. S. Ruoff, Nat. Nanotechnol. **4**, 217 (2009).

[79] J. Park, K. Y. Kim, I. M. Lee, H. Na, S. Y. Lee, and B. Lee, Opt. Express **18**, 598 (2010).

[80] J. B. Pendry, Phys. Rev. Lett. **85**, 3966 (2000).

[81] J. M. Pereira, V. Mlinar, F. M. Peeters, and P. Vasilopoulos, Phys. Rev. B **74**, 045424 (2006).

[82] E. M. Purcell, Phys. Rev. **69**, 681 (1946).

[83] M. Quinten, A. Leitner, J. R. Krenn, and F. R. Aussenegg, Opt. Lett. **23**, 1331 (1998).

[84] K. R. Reitz, F. J. Milford, and R. W. Christy, *Foundations of Electromagnetic Theory* 4th ed. (Addison-Wesley Publishing Company, 2008).

[85] R. Ruppin, Phys. Lett. A **299**, 3092 (2002).

[86] D. Schurig, J. J. Mock, B. J. Justice, S. A. Cummer, J. B. Pendry, A. F. Starr, D. R. Smith, Science **314**, 977 (2006)

[87] F. Schwierz, Nat. Nanotechnol. **5**, 487 (2010).

[88] R. A. Shelby, D. R. Smith, and S. Schultz, Science **292**, 77 (2001).

[89] J. H. Sim, S. C. Song, P. D. Kirsch, C. D. Young, R. Choi, D. L. Kwong, B. H. Lee and G. Bersuker, Microelectron. Eng. **80**, 218 (2005).

[90] U. Sivan, M. Heiblum, C. P. Umbach, and H. Shtrikman, Phys. Rev. B **41**, 7937 (1990).

[91] N. Stander, B. Huard, and D. Goldhaber-Gordon, Phys. Rev. Lett. **102**, 026807 (2009).

[92] T. Stauber, N. M. R. Peres, and A. H. Castro Neto, Phys. Rev. B **78**, 085418 (2008).

[93] A. Snyder and J. D. Love, *Optical Waveguide Theory* (Chapman and Hall, New York, 1983).

[94] Y. W. Son, M. L. Cohen and S. G. Louie, Phys. Rev. Lett. **97**, 216803 (2006).

[95] Y. W. Son, M. L. Cohen and S. G. Louie, Nature **444**, 347 (2006).

[96] J. Spector, H. L. Stormer, K. W. Baldwin, L. N. Pfeiffer, and K. W. West, Appl. Phys. Lett. **56**, 1290 (1990).

[97] W. G. Spitzer, D. A. Kleinman, and D. Walsh, Phys. Rev. **113**, 127 (1959).

[98] K. L. Tsakmakidis, A. D. Boardman, and O. Hess, Nature (London) **450**, 397 (2007).

[99] S. Thongrattanasiri, F. H. L. Koppens, and F. J. Garcia de Abajo, Phys. Rev. Lett. **108**, 047401 (2012).

[100] S. Thongrattanasiri , A. Manjavacas , and F. J. Garca de Abajo, ACS Nano, **6** 1766 (2012).

[101] S. Ulstrup, M. Bianchi, R. Hatch, D. Guan, A. Baraldi, D. Alfè, L. Hornekær, and P. Hofmann, Phys. Rev. B **86**, 161402 (2012).

[102] H. van Houten, B. J. van Wees, J. E. Mooij, C. W. J. Beenakker, J. G. Williamson and C. T. Foxon, Europhys. Lett. **5** 721 (1988).

[103] A. Vakil and N. Engheta, Science **332**, 1291 (2011).

[104] Y. A. Vlasov, M. O'Boyle, H. F. Hamann and S. J. McNab, Nature **438**, 65 (2005).

[105] G. D. Wilk, R. M. Wallace and J. M. Anthony, J. Appl. Phys. **89**, 5243 (2001).

[106] J. R. Williams, T. Low, M. S. Lundstrom and C. M. Marcus, Nat. Nanotechnol. **6**, 222 (2011).

[107] E. Yablonovitch and G. D. Cody, IEEE Trans. Electron Devices **29**, 300 (1982).

[108] A. Yacoby, M. Heiblum, V. Umansky, H. Shtrikman, and D. Mahalu, Phys. Rev. Lett. **73**, 3149 (1994).

[109] H. Yan, X. Li, B. Chandra, G. Tulevski, Y. Wu, M. Freitag, W. Zhu, P. Avouris and F. Xia, Nat. Nanotechnol. **7**, 330 (2012).

[110] A. Yariv, IEEE J. Quantum Electron. **QE-9**, 919 (1973).

[111] K. S. Yee, IEEE Trans. Antennas Propag. **AP-14**, 302 (1966).

[112] A. Young and P. Kim, Nat. Phys. **5**, 222 (2009).

[113] L. Zhao and S. Yelin, arXiv:0804.2225v2 (2008).

[114] F. M. Zhang, Y. He, and X. Chen, Appl. Phys. Lett. **94**, 212105 (2009).